# EFFECTS OF PRODUCTION PARAMETERS ON POROSITY AND HOLE PROPERTIES IN LASER SINTERING RAPID PROTOTYPING PROCESS

A THESIS SUBMITTED TO
THE GRADUATE SCHOOL OF NATURAL AND APPLIED SCIENCES
OF
MIDDLE EAST TECHNICAL UNIVERSITY

BY

ÖZKAN İLKGÜN

IN PARTIAL FULFILLMENT OF THE REQUIREMENTS
FOR
THE DEGREE OF MASTER OF SCIENCE
IN
MECHANICAL ENGINEERING

SEPTEMBER 2005

Approval of the Graduate School of Natural and Applied Sciences

Prof. Dr. Canan ÖZGEN
Director

I certify that this thesis satisfies all the requirements as a thesis for the degree of Master of Science

Prof. Dr. Kemal İDER
Head of the Department

This is to certify that we have read this thesis and that in our opinion it is fully adequate, in scope and quality, as a thesis for the degree of Master of Science

Prof. Dr. Mustafa İlhan GÖKLER
Co-Supervisor

Asst. Prof. Dr. Merve ERDAL
Supervisor

Examining Committee Members:

Prof. Dr. R.Orhan YILDIRIM (METU, ME)

Asst. Prof. Dr. Merve ERDAL (METU, ME)

Prof. Dr. Mustafa İlhan GÖKLER (METU, ME)

Asst. Prof. Dr. İlhan KONUKSEVEN (METU, ME)

Prof. Dr. Can ÇOĞUN (GAZİ UNV., ME)

I hereby declare that all information in this document has been obtained and presented in accordance with academic rules and ethical conduct. I also declare that, as required by these rules and conduct, I have fully cited and referenced all material and results that are not original to this work.

Özkan İLKGÜN

# ABSTRACT

EFFECTS OF PRODUCTION PARAMETERS ON POROSITY AND HOLE PROPERTIES IN LASER SINTERING RAPID PROTOTYPING PROCESS

İLKGÜN, Özkan
M.Sc., Department of Mechanical Engineering
Supervisor: Asst. Prof. Dr. Merve ERDAL
Co-Supervisor: Prof. Dr. Mustafa İlhan GÖKLER

September 2005, 126 Pages

Selective laser sintering (SLS) is a rapid prototyping method in which three-dimensional objects are constructed by sintering thin layers of a variety of powdered materials via laser beam. In SLS, as in most other Rapid Prototyping methods, the produced parts exhibit varying degrees of intrinsic porosity due to the discrete nature of layer-by-layer production. Selective scanning and discrete bonding of individual particles or clusters of particles impart local porosity, which is mostly an undesired trait as the part integrity decreases with increased porosity. However, there are a number of emerging or potential applications as in tissue engineering and composite/functionally graded materials, in which part porosity and its control during production are needed.

In this study, the manufacturing capabilities of selective laser sintering are investigated towards producing *predesigned* porous structures using a polymeric powder. The porous structures are characterized in two main categories: regular porous structures, which involve geometries such as predesigned holes and lattice structures that have orderly porous architecture, and irregular porous structures, which exhibit random pore architecture that is intrinsic in all SLS parts. The limitations of producing regular porous structures are investigated, identified and quantified, based on hole size and dimensional accuracy. An experimental analysis based on design of experiments is employed to investigate the effects of processing parameters on the resulting macroscopic pore properties of irregular porous structures. A mathematical relation is developed to quantify and predict the relations between the SLS process parameters: Laser power, hatching distance, laser scan spacing, and the resulting apparent mass density (as a measure of porosity). The subsequent tests verify accuracy of the developed empirical model.

**Keywords:** Selective Laser Sintering, Rapid Prototyping, Manufacturing, Porous Structures, Design of Experiments.

# ÖZ

## LAZER SİNTERLEME HIZLI PROTOTİPLEME TEKNOLOJİSİNDE ÜRETİM PARAMETLERİNİN, PARÇA GÖZENEK YAPISI VE DELİK ÖZELLİKLERİ ÜZERİNDEKİ ETKİLERİ

İLKGÜN, Özkan

Yüksek Lisans, Makina Mühendisliği Bölümü

Tez Yöneticisi: Y. Doç. Dr. Merve ERDAL

Ortak Tez Yöneticisi: Prof. Dr. Mustafa İlhan GÖKLER

Eylül 2005, 126 Sayfa

Lazer sinteleme, toz yapılarının katman katman birbirlerine lazer ile sinterlenmesiyle, bir çok değişik malzememeden 3 boyutlu parça imalatı yapabilen bir hızlı prototipleme teknolojisidir. Katman katman üretim metodunun kendine özgü doğasından ötürü, diğer bir çok hızlı prototipleme teknolojisinde de olduğu gibi, Lazer Sinterleme teknolojisiyle üretilen parçaların içerisinde gözenek yapıları bulunmaktadır. Bu gözenek yapılarındaki artış, üretilen parçaların dayanımlarında azalmaya neden olduğu için, genel uygulamalarda üretilen parçaların içerisinde gözenek yapılarının mümkün olduğunca az olması istenilmektedir. Fakat, son zamanlarda, doku mühendisliği ve işlevsel kompozit üretimi gibi, ortaya çıkan yeni bazı potansiyel uygulamalarda, parçalar içerisinde gözenek yapılarının bulunması ve bu gözenek yapılarının üretim işlemi sırasında kontrollü bir şekilde oluşturulması gerekliliği ortaya çıkmıştır.

Yapılan bu çalışmada, Lazer Sinterleme teknolojisinin, polimer bir malzemeden, önceden tasarlanmış gözenek yapılarını üretebilme kabiliyetleri araştırılmıştır. Bu çalışmada gözenek yapıları iki ayrı sınıf olarak tanımlanmıştır: üzerlerinde düzenli delik mimarisi bulunan, düzenli gözenek yapıları ve, tüm lazer ile sinterlenmiş parçaların içerisinde bulunan, dağınık gözenek yapıları. Düzenli gözenek yapıları ile ilgili yapılan çalışmada, Lazer Sinterleme teknolojisi ile oluşturulabilecek minimum delik büyüklükleri araştırılmış, belirlenmiş ve bu düzenli delik yapılarının oluşturulmasındaki hassasiyet incelenmiştir. Düzensiz gözenek yapıları ile ilgili yapılan çalışmalarda ise, deney tasarımı metodu kullanılarak gerçekleştirilen deneyler ile, Lazer Sinterleme teknolojisinin üretim parametrelerinin parçalar içerisinde oluşan düzensiz gözenek yapılarındaki etkileri incelenmiştir. Deneyler sonucunda, Lazer Sinterleme üretim parametrelerinden lazer gücü, lazer tarama hızı ve tarama aralığı parametrelerinin üretilen parçalarının yogunluğu üzerinde olan etkilerini hesaplayan ve bu etkileri üretim öncesi tahmin edebilen matematiksel bir denklem bulunmuştur.

**Anahtar Sözcükler:** Selective Laser Sintering, Hızlı Prototipleme, Gözenek Yapıları, Deney Tasarımı.

To My Family,

## ACKNOWLEDGEMENTS

I express sincere appreciation to Asst Prof. Dr. Merve Erdal and Prof. Dr. Mustafa İlhan Gökler for their guidance, advice, criticism, systematic supervision, encouragements, and insight throughout the study.

I wish to thank to Prof. Dr. Cahit Eralp, Prof. Dr. Bilgehan Ögel, Prof. Dr. Leyla Aras, Asst. Prof. Dr. Serhat Akın, Mr. Cengiz Toksöz and Mr. Rahmi Ercan. The support of them is gratefully acknowledged.

I wish to thank to Mr. Halit Şahin specifically for his willingness to help me for all the times I ask for.

I also would like to thank to METU-BİLTİR Research & Application Center for the facilities provided for my work.

Special thanks go to my colleagues, Ender Cengiz, Ömer Köktürk, Evren Anık, Pelin Sarı, Kazım Arda Çelik, İlker Durukan, Mehmet Maşat, for their valuable support and aid; to my senior colleagues Mehmet Tunç, Sertan Gülbahar, Barış Civelek, Barış Karagözler and Ernur Kazancı for their support and guidance.

I offer sincere thanks to my parents, Nermin and İsmail İlkgün and my brother Özgür Barış İlkgün, for their encouragement and faith in me.

**TABLE OF CONTENTS**

## LIST OF TABLES

## LIST OF FIGURES

## LIST OF SYMBOLS

**SYMBOL**

| | |
|---|---|
| CT | : CT Number |
| $d_c$ | : Beam offset for contouring |
| $d_h$ | : Initial beam offset for hatching |
| D | : Physical laser beam diameter |
| $D_e$ | : Effective laser beam diameter |
| $D_{ec}$ | : Effective laser beam diameter during contouring |
| $D_{eh}$ | : Effective laser beam diameter during hatching |
| ED | : Laser Energy Density |
| HD | : Hatching Distance |
| HS | : Hole size of the regular pores |
| LP | : Laser Power |
| LS | : Laser Scan Speed |
| SS | : Sum of Squares |
| WT | : Wall thickness between regular pores |
| $\phi$ | : Porosity |
| Ø | : Diameter of the specimen |

# CHAPTER 1

# INTRODUCTION

## 1.1 Rapid Prototyping

Rapid prototyping (RP) methods denote a family of technologies that enable rapid fabrication of complex three-dimensional physical structures. These technologies are also known by the names Solid Freeform Fabrication and Layer Manufacturing. All RP systems operate on the principle of layer-by-layer production (Figure 1.1). The system accepts as the input, the STL model CAD data of the object to be produced, through a computer interface. An STL file is simply a mesh of triangles wrapped around a CAD model. STL name is derived from rapid prototyping process, **St**ereo**L**ithography, also known as Standard Triangulation Language. This very simple format has become an industry standard for the Rapid Prototyping sector. Virtually all modern CAD Systems now include STL or Rapid Prototyping output as a standard feature.

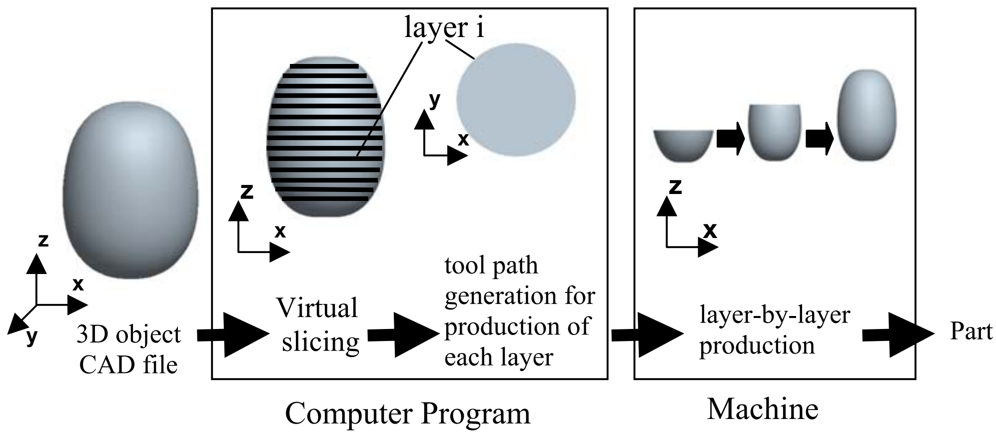


**Figure 1.1: Layer by layer production**

The software inside the RP system virtually slices the STL model into thin even layers. The RP system then reconstructs the object physically by building one layer at a time, bonding each layer to the previous layer. The term “rapid” in rapid prototyping does not necessarily indicate the speed at which an object is manufactured but also, the ease and efficiency with which one can build different and relatively complicated geometries (objects) by only a change of CAD data. RP systems do not require tooling; however some post-processing may be needed. The material with which an object can be manufactured depends on the RP system employed.

RP was originally developed to reduce the prototyping time for product development and manufacturing. Today's systems are heavily used by engineers to better understand and communicate their product designs.

In addition to prototypes, RP techniques can also be used to make tooling (referred to as *rapid tooling*) and even some production-quality parts (*rapid manufacturing*). For small production runs and complicated objects, rapid prototyping can be a viable manufacturing process.

There exist about thirty rapid prototyping techniques, but only few of them are widely used and dominant in the market [1, 2, 3]. These are:

- Selective Laser Sintering (SLS),
- Stereolithography (SLA)
- Fused Deposition Modeling (FDM)
- Laminated Object Manufacturing (LOM)
- Inkjet-based systems and three-dimensional printing (3DP).

Each of these technologies has its varying strengths and weaknesses depending on the manufacturing details, type of material and post processing. The current study focuses on SLS technology.

## 1.2 Selective Laser Sintering (SLS)

In Selective Laser Sintering (SLS) system, a part is built by sintering special powder material through employing a laser beam. In this process, the fabrication

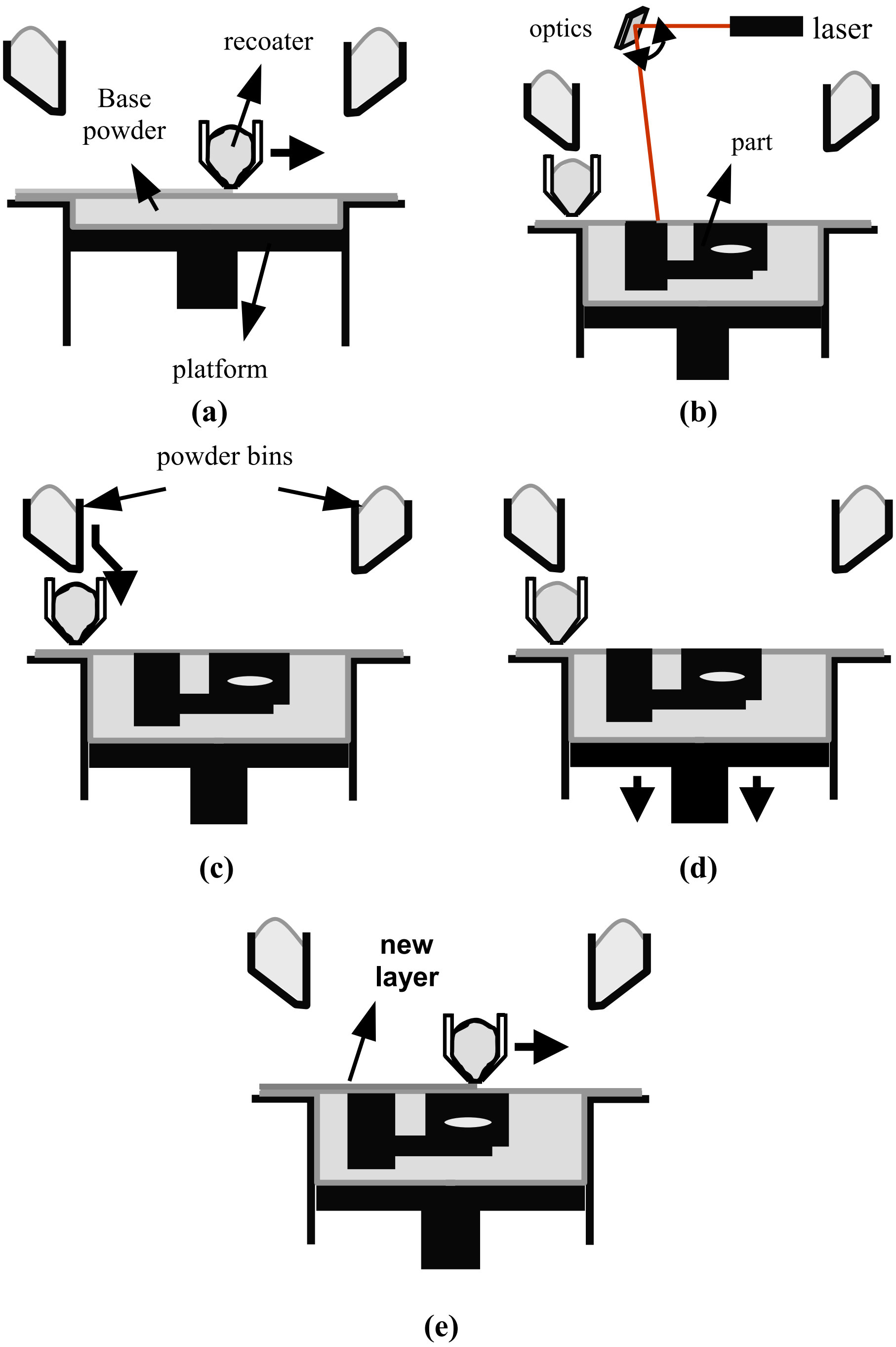


**Figure 1.2: Process steps of SLS**

chamber is maintained at a temperature just below the melting point of the powder and the heat from the laser slightly elevates the temperature, resulting in sintering.

A typical SLS system includes a laser source, optics, powder laying unit(recoater), powder bins and a platform all within a fabrication chamber. Before starting the SLS process, some amount of powder is laid down on the platform as a base (Figure 1.2(a)). Once the process is started, the powder layer at the top of the platform is scanned (sintered) with the laser beam according to laser paths generated in slicing process (Figure 1.2(b)). During sintering the powder particles bond to one another as well as previously sintered particles, forming solid structure. Afterwards, fresh powder is supplied from powder bins to the recoater (Figure 1.2(c)). Next, the platform is moved one layer thickness down, (Figure 1.2(d)), and a new layer of powder is laid by recoater to the whole surface, (Figure 1.2(e)). Except laying down the base powder, the process continues in the same sequence until the last layer [2, 4, 5].

Compared to other RP methods, parts from a larger variety of thermoplastic materials such as polyamide, glass filled polyamide and polystyrene can be built in SLS. SLS is also used in direct fabrication of metal parts using metal powders such as bronze and nickel powder [6]. The technology also enables the production of relatively large objects compared to the other RP methods. Another advantage of the SLS system is the speed of the production. Among all RP methods, the production time in SLS is shortest along with Stereolithography (SLA) [2, 5].

Before starting the SLS process sufficient amount of time is required for the fabrication chamber to reach the working temperature. After part building is completed again some amount of time is required in order to decrease the chamber temperature. Time required for cooling is longer than heating time in order to avoid thermal distortions in part due to rapid cooling [5].

At the end of the part building process, a block of partially hardened powder material is left in the SLS unit in the form of a single body, which has the built part in it. This block of powder material is removed from the SLS system, generally by using apparatus supplied with the machine and carried to a pool or platform for removing the prototype part out of it. Then, the partially hardened unsintered powder around the part is cleaned by sand blasting. Unsintered used powder can be reused later for other operations; this is done by mixing it in proportion with fresh, unused powder.

In most of the RP processes, certain geometries, such as overhangs, require support structures, like a scaffold, underneath during the build [5]. In Fused Deposition Modeling (FDM), for instance, the system has a separate mechanism developed entirely to build support. In SLS, since every layer rests on either sintered (part of the solid structure) or unsintered powder; there is no need for a separate support building mechanism. In geometries such as overhangs, the unsintered powder underneath serves as a natural support [2]. Since support structures are not constructed in SLS process additional parts can be placed in the available space by interrupting the process that has already started. Thus starting a new job in SLS system by interrupting the current job is possible if a suitable unsintered powder volume is available in the current job [6].

For the prototyping applications with SLS usually polyamide or similar plastic materials are used as the powder material. Average particle size of plastic powder materials varies between 50μm and 110μm. Bulk density of the plastic powder materials is usually about 0.5 $g/cm^3$ and these values are usually doubled after sintering. Layer thickness can be varied between 0.10 mm and 0.20 mm. Power of $CO_2$ laser being used for sintering plastic powder is 50W. Depending on the material working temperature inside of the SLS unit is around 120-180 ºC. Plastic powder materials can easily burn at such high temperatures. In order to prevent this situation air is not allowed and Nitrogen gas is used inside of the SLS unit [3].

Apart from prototypes, the plastic laser sintering machines are also used for the direct production of tooling (rapid tooling). Main application of using plastic laser sintering in rapid tooling is to produce patterns for plaster, investment and vacuum casting [7].

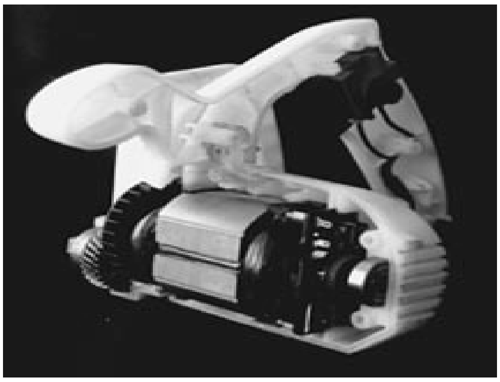

**Figure 1.3: A sample of working prototype made with the SLS technique [6]**

The metal laser sintering machines are mostly used in rapid tooling applications [7, 8, 9]. The laser power of metal laser sintering (MLS) machines is usually around 200W, which is naturally higher than it is for the plastic sintering machines. In MLS, a special metal powder, usually consisting of a mixture of bronze, nickel and steel with some additives, is used as the material. Average grain size of metallic powder materials vary between 0.010μm and 0.015μm. Layer thickness can be changed between 0.05 mm and 0.10 mm [6].

Among all the commercial RP methods, parts built by SLS process have the second best surface finish after the Stereolithography[10]. Because of the sinterization of plastic/metal powder itself and its nature, which is free from anisotropic effects, parts built by SLS have relatively good strength properties [6, 11]. As a result, prototype parts manufactured with SLS technique are generally used for working prototypes, as shown in Figure 1.3.

## 1.3 Porous Structure with RP Technologies

In all RP methods, the produced parts exhibit varying degrees of intrinsic porosity due to the discrete nature of layer-by-layer production. Porosity is mostly an undesired trait as the part integrity decreases with increased porosity. Thus in applications such as rapid tooling, [12, 13] porosity is generally undesired. However, in more recent RP applications such as building scaffolds for tissue engineering [14-18], part porosity is a desired and required trait.

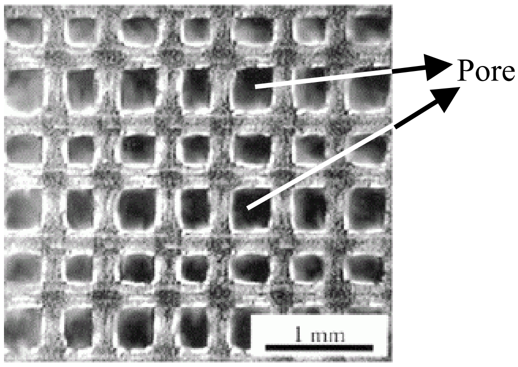


**Figure 1.4 : Regular Porous Structure with FDM to be used as a scaffold for tissue engineering [20]**

Another potential application that requires part porosity involves generation of complex preforms with RP for processing functional composites or functionally graded materials via subsequent resin transfer molding process [19]. In such applications, the discrete nature of RP production can enable the generation of pores within a part, with various degrees of control, depending on the RP method employed.

The intrinsic porosity in RP methods (that needs to be minimized when undesired or that must be produced in a predesigned quantity/pattern when desired) necessitates the study of how an RP system generates porosity and how it can be controlled. In this research, the porosity generation capabilities of SLS method that employs a polymeric powder are studied.

In studies involving the porosity of the parts produced via RP technologies, the porous structures can be characterized in two main categories: **regular porous structures** and **irregular porous structures**.

**Regular porous structures** are porous parts in which pore architecture is established with ordered holes on the part. These ordered holes are specified in the CAD file from which the part is produced. The RP "tool" generates the pore architecture (holes) by following the prespecified "paths" on each layer. In such cases, specific pore architecture is to be produced with predetermined hole size and shape in a desired distribution [14, 15, 20, 21]. Figure 1.4 shows a section of such a regular porous part produced by the RP

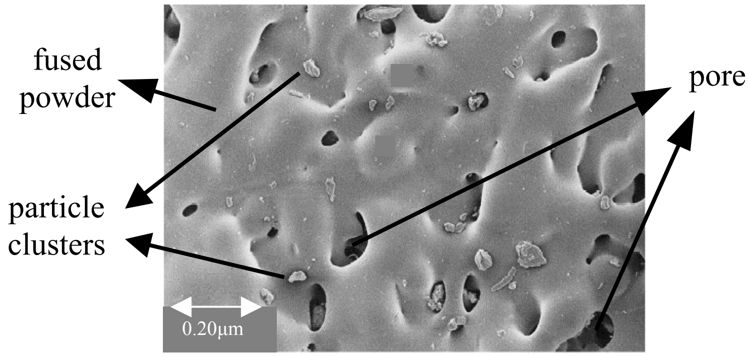


**Figure 1.5: Irregular Porous Structure [12]**

method, FDM.

In **irregular porous structures**, the pore formation is random (unlike in **regular porous structures**) and the pore architecture does not exhibit an orderly geometry. Figure 1.5 presents a section of a part produced by SLS in which the pore formation is random. A number of unbonded clusters of particles can be seen, in addition to the fused powder, exhibiting random pore architecture.

### 1.3.1 Regular Porous Structure Studies in the Literature

Among the many commercialized RP processes available, the fabrication of parts with regular porous structures (ordered holes on the parts) have been studied for fused deposition modeling (FDM), stereolithography (SLA), and three-dimensional printing (3DP) [14, 15, 16, 17, 18]. The feasibility of utilizing an RP technique for fabricating parts with regular porous structures depends mainly on the resolution and the smallest feature that can be built with that particular RP technique. Such a capability is usually constrained by the working principles of the RP process, as well as the process parameters and properties of the building materials.

In RP literature, almost all of the regular porous structure studies are concentrated on producing scaffolds for Tissue Engineering (TE) applications. TE is a relatively new field in biomedical engineering, in which the purpose is to regenerate and grow living tissues or organ substitutes as alternatives to harvested

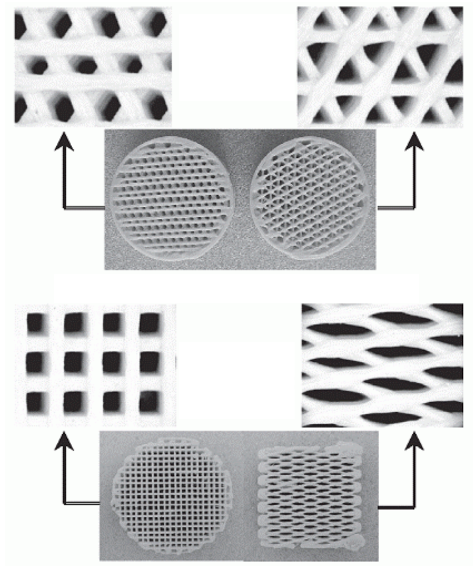

**Figure 1.6: Hard Tissue Scaffolds produced via FDM [20]**

tissues, implants and prostheses [14]. Beginning with the extraction of actual living tissue cells from human patients, the cells are then seeded onto a carrier (scaffold), which accommodates and guides the growth of new cells in three dimensions within the laboratory environment. These scaffolds must be biocompatiple and biodegradable as they are to be disposed naturally once the tissue is implanted in human body [16]. High degrees of porosity and hole interconnectivity are critical requirements of TE scaffolds [16, 18].

Kalita et al, 2003 [20], worked on building hard tissue scaffolds (for bone growth). In their work they were able to produce controlled porosity polymer-ceramic composite scaffolds with different hole shapes, sizes and internal architectures via fused deposition modeling (FDM) (Figure 1.6). The minimum hole size that was reported was 0.160 mm. A variation on hole structure and porosity on the same part was also shown to be possible (Figure 1.7).

Bose et al, 2003 [15], worked to produce alumina ceramic hard tissue scaffold via using FDM as a rapid tooling process. In their work, Bose et al. utilized FDM fabricated mold with regular porous structure to cast 3D alumina ceramic scaffold structures with porosity and hole sizes of 33% to 50% and 0.3 mm to 0.75 mm respectively. The ceramic structures are also reported to have

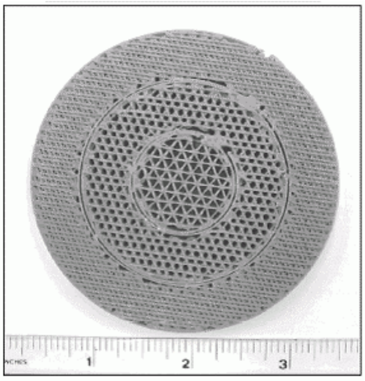


**Figure 1.7: Gradient Porous Structure with FDM [20]**

%100 hole interconnectivity.

Another study was done by Chu et al [21], who evaluated the use of ceramic resins in SLA. The hole sizes obtained in their work were very fine, 0.070 to 0.120 mm, however the porous ceramic parts were very fragile.

### 1.3.2 Irregular Porous Structure Studies in the Literature

Irregular porous structures cannot be described as precisely as regular porous structures, where the porous architecture is defined and ordered. Instead, a macroscopic approach is employed here in which the porous architecture is to be defined by the macroscopic porosity, and its distribution.

In the RP literature, all the porosity studies are performed on selective laser sintering, SLS. Most of the studies were performed in order to understand the effect of the SLS processing parameters on the final property of the product, such as strength, hardness, density, surface roughness, etc. These studies are mostly on the metal laser sintering process and for them porosity is an undesired trait as the part integrity decreases with increased porosity. Thus in all these studies, porosity is tried to be decreased.

Studies on porosity generated in SLS show that there are many parameters affecting the porosity of parts [22]. These parameters (Figure 1.8) are mainly found as laser power, scanning speed (speed at which the laser scans a path), step size (distance between two successive points receiving laser pulses),

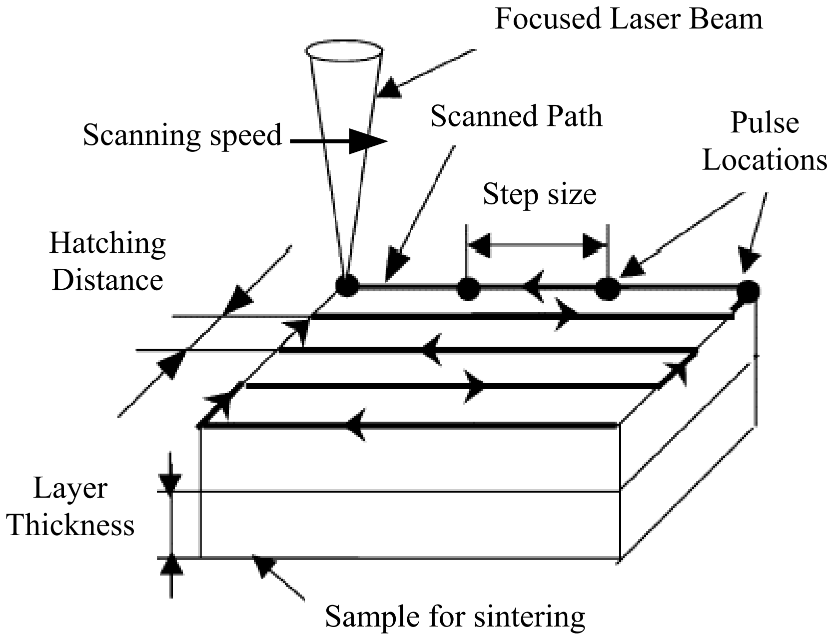

**Figure 1.8: SLS processing parameters effecting porosity**

focused laser beam diameter, layer thickness, hatching distance (distance between successive laser scan lines), and powder characteristics (type of material, particle size, particle size distribution, etc.).

Miller et al [23] have carried out experiments to express the strength of a sintered composite steel powder as a function of laser power and hatching distance and their respective interaction terms. In their work, two mathematical models were developed for the small (0.25 mm) and large beam diameter (1 mm)on the strength of sintered samples.

The study by Song [24] states the influence of laser parameters like laser beam power, beam diameter and experimental parameters like hatching distance (Figure 1.8) on density, strength and surface roughness of a laser-sintered bronze product.

Hardro et al. [25] determined the optimal process parameters of the selective laser sintered elastomeric polymer for dimensional accuracy and strength on parts. Laser power, laser scan spacing and part bed temperature were the factors under consideration while dimensional accuracy and material strength of the sintered samples were the response characteristics. It was concluded that all the factors as well as their interactions, were statistically significant.

Another experimental study was performed by Chatterjee et al [22], in which the hatching distance and layer thickness were selected as two factors that affected density, porosity and hardness of the laser sintered low carbon steel powder.

In addition to metal laser sintering, in the literature there are also some irregular porosity studies on the manufacture of polymer based components using plastic laser sintering. For example, Ku et al [28], explored the variation of the degree of porosity of the laser sintered polystyrene parts by manipulating the laser power. The amount of the porosity variation was characterized by the infiltration characteristics by a different liquid material: The porosity is measured in terms of the mass of the infiltrated material.

Similarly in the study by Ho et al [11], polycarbonate specimens were created under different laser power and the effects of the laser power on the physical density and the tensile properties (fracture behavior) of the components were studied.

### 1.4 Scope of the Thesis

In this study, porous structure building capabilities/incapabilities of SLS process are investigated. The study is not geared towards a specific application such as tissue engineering or a specific goal such as maximizing part strength by minimizing porosity. Rather, an exploratory investigation of the part porosity/ porous architecture and machine process parameters/capabilities is conducted. As the application of porous parts built via rapid prototyping and laser sintering are newly emerging, the porous structure building capabilities of rapid prototyping systems (and in this case, selective laser sintering) must be investigated.

The laser sintering machine, EOSINT P380, which is in METU-BİLTİR CAD/CAM and ROBOTICS center, is employed in this study (Figure 1.9). The

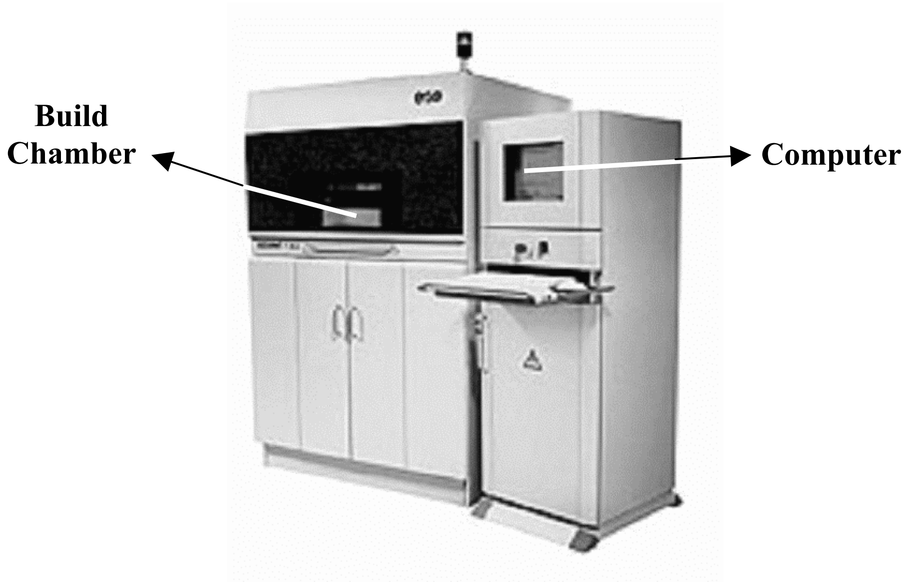


**Figure 1.9: EOSINT P380 Laser Sintering Machine**

manufacturer of this machine is a German company: Electro Optic Systems (EOS).

The polymer used in the study is a fine polyamide powder, PA 2200, available in most commercial available laser sintering systems. The typical application with this material is production of fully functional prototypes. The data sheet of this material can be found in Appendix A.

In Chapter 2, the laser exposure characteristics of the SLS system is examined and explained.

The first part of the research involves studying the relations between the process parameters and the resulting part porosity (irregular porous structure). A major issue is the proper characterization of the porosity. Unlike regular porous structure, where pore architecture (holes) is easily observed visually and hence understood, the pore architecture and porosity in irregular porous structures are random, thus not quantified in a straightforward manner. A macroscopic quantification is sought and presented. The effect of various process parameters on irregular porosity is also sought. For this again a comprehensive experimental study is undertaken, involving part manufacturing and analysis. These efforts are presented in Chapter 3.

In seeking the relations between process parameters and the resulting porosity, design of experiments is employed. Influence of each parameter and interaction of parameters are quantified and a mathematical relation is developed. This work is presented in Chapter 4.

The second part of the research involves investigating the regular porous structure generating capabilities of the SLS system in a controlled manner. This is presented in Chapter 5. In the study, the regular porous structure are named as **hole structures**. In Chapter 5 the limitations of the SLS, based on laser exposure characteristics, in producing small hole features are sought through comprehensive part manufacturing and analysis.

The results are presented and discussed in Chapter 6 and the conclusions and future work are presented in Chapter 7.

The methodology developed in seeking the relations between the process parameters and part porosity in irregular porous structures can be directly applied to other SLS systems where the materials may be different, specifically when a process-property relation is sought. The limitations that are sought for pore feature accuracy and size in regular porous structures are expected to be different quantitatively but similar qualitatively for other materials. Most importantly, the current research aims to serve as a road map for others in developing processing strategies towards the production of porous architectures with controlled porosity and pore architecture.

# CHAPTER 2

# LASER EXPOSURE CHARACTERISTICS OF EOSINT P380 LASER SINTERING MACHINE

As the theory of producing small hole features with SLS and the porosity of the laser sintered parts are directly dependant on the laser exposure parameters and the laser exposure (scanning) strategies of the process, before explaining the details of the studies on the porosity of the laser sintered parts and production of small hole features, first the details of the laser exposure parameters and the laser scanning strategy of the EOSINT P380 machine and will be explained in detail in this chapter.

## 2.1. The Laser Scanning Strategy of EOSINT P380

In the EOSINT P380 system, the scanning strategy of the laser beam for building a layer is mostly fixed, with little room for variation, except for layer geometries that include very thin sections. The laser scan proceeds through hatching or contouring, depending on the slice (layer) geometry obtained from the STL file. The machine software specifies the perimeter(s) (boundaries) of the

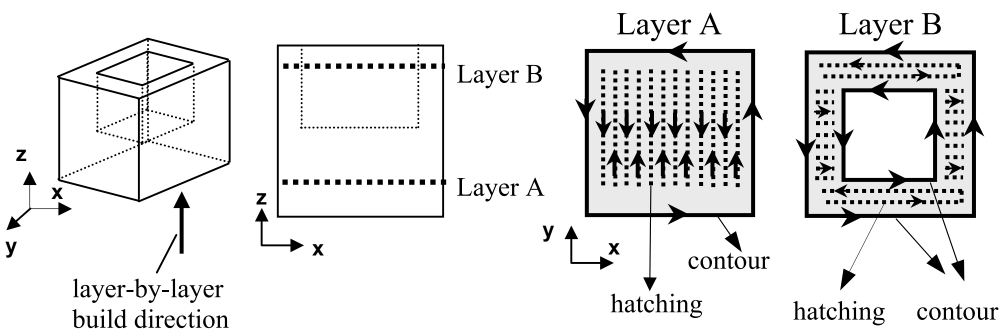


**Figure 2.1: Laser scanning strategy in EOSINT P380**

region that needs to be scanned as contours and the enclosed area within the perimeter(s) as the hatching area. During scanning (curing) of a layer, the laser first draws the contours (boundary), and then proceeds to fill inside, by hatching. In contouring, the laser beam simply follows the contour line in a single pass. In hatching, the laser beam follows a linear path back and forth as it moves along a perpendicular direction. Figure 2.1 presents the scanning strategy for a simple part. In layers A and B, the contours and hatching regions are identified. When an inner detail like hole or a pocket (as shown in Figure 2.1) exists on the part to be produced, the section of the powder layer that corresponds to those inner details is to be unexposed to laser beam. The machine software regards the circumference of those inner details as part of the boundary (contouring) of the region that will be cured. The hatching paths are shown with dashed lines, in Figure 2.1. As seen from the figure between the layers A and B, the directions of the hatching paths are different. The hatching direction variation between the layers depends on the user's selection. This will be explained in detail later.

## 2.2 The Laser Exposure Parameters

The parameters of contour exposure are also the parameters of hatching exposure, but at different values. However hatching exposure has some additional parameters. Below, all the parameters relevant to laser exposure are discussed.

### a) Laser Power

In the process software, the laser power is input as a percentage of the maximum laser source power. The input value depends on the type of the material and the layer thickness, with which the part is built. The corresponding value in W can be determined on the basis of the laser power curve. The laser power curve is a characteristic of the machine, recorded by the service technician during the installation of the machine, which is given in Figure 2.2. As seen from Figure 2.2, the resulting laser power is dependant on the power setting of the laser source, which is inputted in the process software.

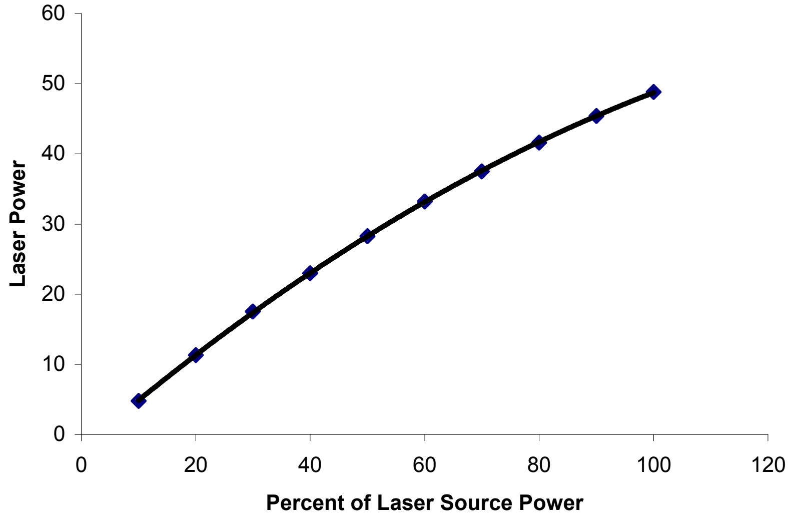


**Figure 2.2: Laser Power Curve**

During building of a layer the laser power for the contouring is generally smaller than that for the hatching distribution. In the standard applications using EOSINT P380, the recommended laser power during the contouring is set to 9.40 W, whereas for the hatching, it is 38.2 W. (Standard parameter settings of EOSINT P380 are listed in Appendix B)

**b) Laser Scanning Speed**

The laser scanning speed is also a process parameter that can be adjusted. In standard applications, the recommended laser scanning speed during contouring is 700 mm/s, whereas for the hatching this standard value is 4500 mm/s.

**c) Effective Diameter of the Laser Beam**

In SLS systems, the produced laser beam is focused down to a certain beam diameter where it contacts the powder surface. For the EOSINT P380 system, this diameter is 0.4 mm. However, the diameter of the region where the particles are sintered (effective sintering range) is larger than the physical beam diameter. This range is denoted as the **effective diameter of the laser beam**, $\mathbf{D_e}$, (Figure 2.3), which is proportional to the laser power and inversely proportional to the scanning speed of the laser. As the laser power and the laser speed settings for the

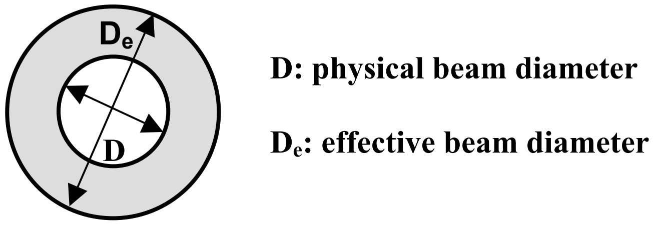


**Figure 2.3: The Effective Diameter of the Laser Beam**

contouring and hatching differ, the $\mathbf{D_e}$ during contouring ($\mathbf{D_{ec}}$) and hatching ($\mathbf{D_{eh}}$) also differs. During the initial installation of the machine, with the 9.40 W laser power and the 700 mm/s laser speed settings $\mathbf{D_{ec}}$ has been experimentally measured as 0.680 mm. The exact value of $\mathbf{D_{eh}}$ was not calculated during installation, as it does not have a special significance during general applications in EOSINT P380. However, the $D_{eh}$ known to be greater than $D_{ec}$, due to the considerable higher laser power in hatching, even though the laser scanning speed is high.

**d) Beam Offset (Displacement)**

During the scanning a layer, the laser beam center does not move all the way to the edge of the layer, but stops before it (Figure 2.4). The distance between the center of the laser beam and the edge of the layer is called the **beam offset**. In

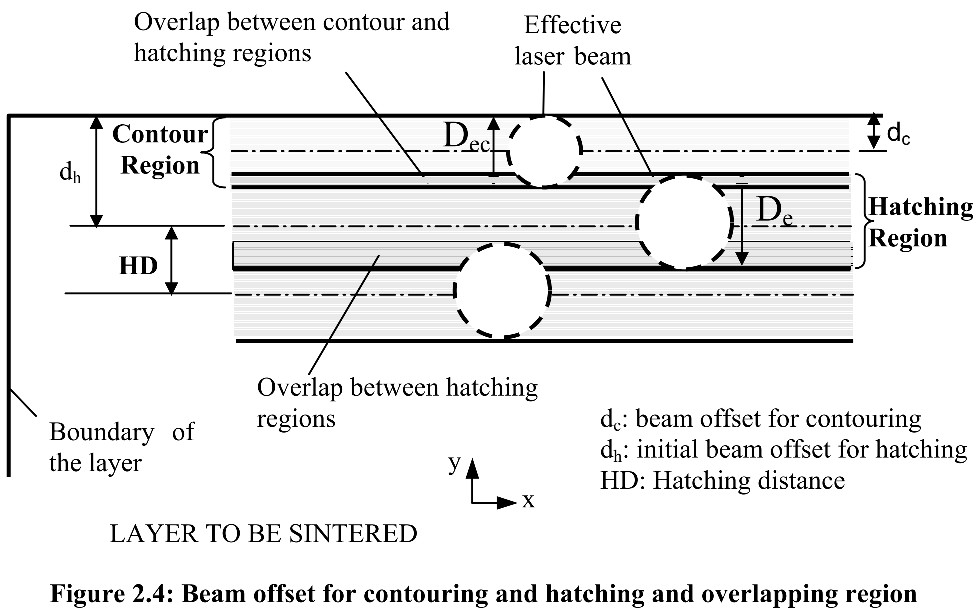


**Figure 2.4: Beam offset for contouring and hatching and overlapping region**

the SLS system, the beam offset can be entered separately for contouring and hatching. In order for the powder at the edge of the boundary to be completely exposed to the laser beam, for the contouring the value of the beam offset, ($\mathbf{d_c}$), should be set to the half of the $\mathbf{D_{ec}}$. If the beam offset for contour is less or greater than half the effective beam diameter, then there is the possibility of sintering powder outside the layer edge or not sintering part of the intended edge region, which would disrupt the dimensional accuracy of the part.

During hatching, the initial beam offset value is again defined with respect to the edge of the boundary (which should be larger than that for contouring), however, in this case caution must be observed in guaranteeing that there are no unsintered particles between the contour path and the hatching region. Thus, the beam offset for hatching ($\mathbf{d_h}$) must be chosen in such a way, so as to form a narrow overlapping regions between the contour path and the hatching region. (Figure 2.4). The overlap should not bee too wide though, to prevent oversintering.

**e) Hatching Distance**

The hatching distance is described in Figure 2.5, where the laser path during hatching is shown. The hatching distance must be smaller than the effective

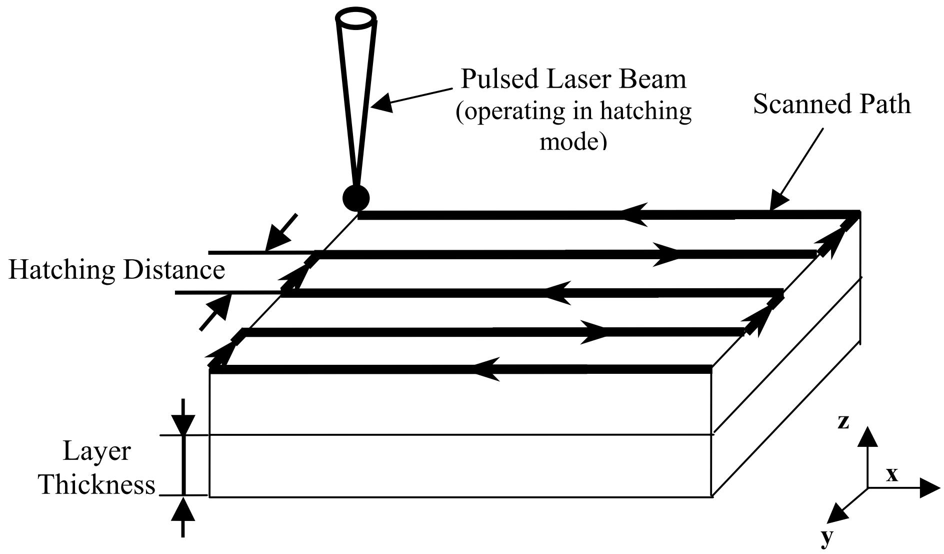


**Figure 2.5: Hatching Distance**

diameter of the laser beam during hatching, $\mathbf{D_{eh}}$, otherwise a connection between the hatching lines cannot be guaranteed. For the standard applications, the recommended hatching distance value is 0.30 mm.

### 2.3 Scanning of Thin Sections

When the layer to be scanned includes geometric features such as very thin sections, the scanning strategy is slightly different than the cases above. Specifically, when a layer section that must be scanned has a dimension less than "2 x $d_c$ (beam offset for contour)", "contouring + hatching" exposure can not generate the desired feature. In fact, even if hatching is not performed (due to the small scan width), contouring exposure alone may not generate the feature. The system software processes the two edges of a thin section as boundaries of the scanning region. Consequently, the contour beam offset is defined with respect to each of the two boundaries. In that case, the laser beam scans the thin section twice (once for each boundary) and the width of the overlap is more than the width of the section, which would result in sintering of a larger region than intended. In such a case, the machine software option "EDGES" must be chosen. This function commands the laser beam to pass through the thin section only once (rather than twice when each edge of the section is regarded as a separate boundary in contouring), decreasing the width of sintered region and approximating the intended width more accurately. If this option is not selected, by default, the machine does not build the corresponding feature for thin sections, but simply leaves the region unsintered. An example of such a section with the corresponding strategy is outlined in Figure 2.6.

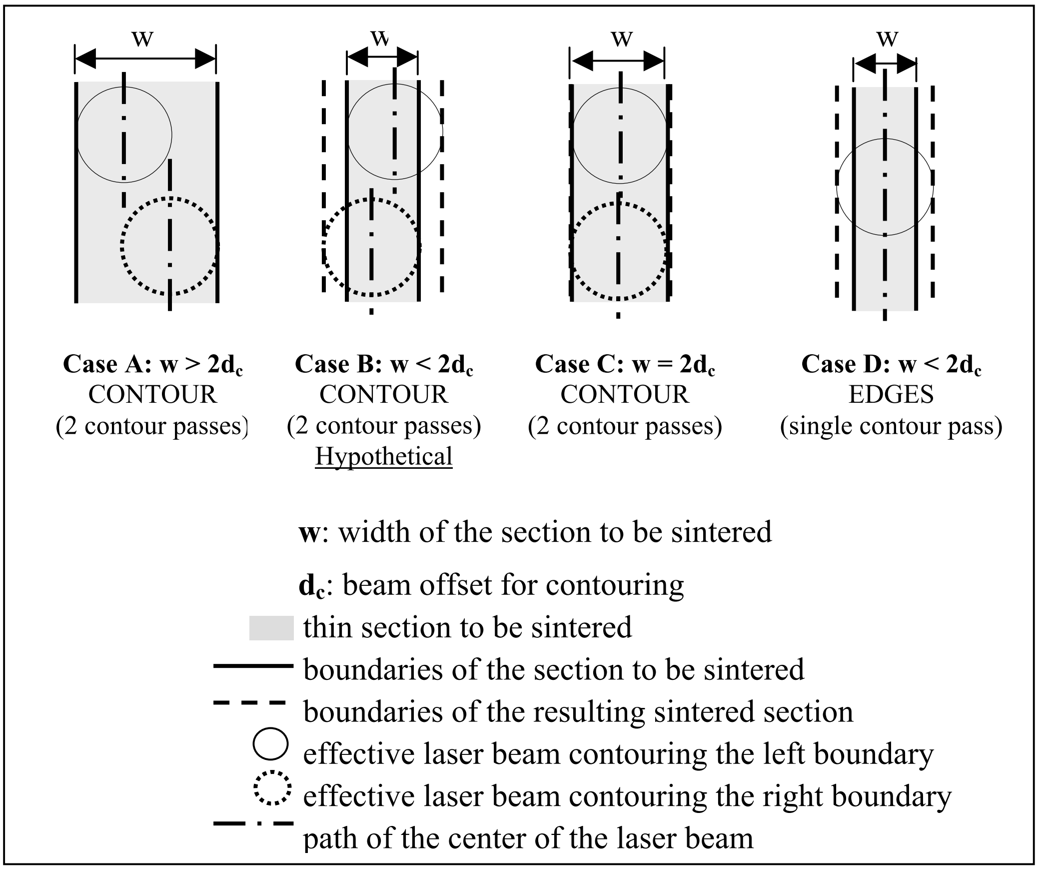


**Figure 2.6: EDGES Function (Exposure of the thin sections)**

# CHAPTER 3

## POROSITY OF THE LASER SINTERED PARTS
## (IRREGULAR POROUS STRUCTURES)

Various process parameters that are effective on the part porosity in SLS were discussed in Chapter 1 (Figure 1.8). In this part of the research, the relations between the effective process parameters and the resulting part porosity are sought. A design of experiment type analysis is performed in order to quantify the effects and interaction of the parameters, the details of which are presented in Chapter 4.

The process parameters, the effects of which will be studied, have been restricted to the laser power, the hatching distance and the laser scanning speed, as they are considered to be relatively more effective than others on the porosity. In the literature, almost all studies regarding the porosity in laser sintered parts were concentrated on a single parameter [11,28], most commonly either laser power or hatching distance. The effects of the parameters concerned in these studies were calculated through the experiments, which were based on trial and error. That is, the response to the variation of a single experiment is as studied, whilst other process parameters are kept constant. In the current study, in addition to the isolated effects of the three chosen parameters on the porosity of the laser sintered parts, their interaction effects are also studied and quantified.

It has been observed that the porosity of the parts produced in SLS systems is directly related with the energy density to which the part is exposed [11]. The energy density can be expressed as:

$$ED = \frac{P}{HD \cdot LS} \tag{3.1}$$

where $P$ is the laser power during hatching exposure, $HD$ is the hatching distance and $LS$ is the laser speed during hatching exposure.

In general, the high energy density of a laser beam results in better fusion of the polymer particles and enables a more compact structure to be built, resulting in a decrease in the porosity. When the energy density becomes excessively high, however, degradation of the polymer will occur. The degradation results in a slight decrease in the porosity, which will be discussed in more detail, later (Section 3.3.1). On the other hand, at low energy density levels, the part is likely to have higher porosity due to insufficient bonding between powder particles.

Initial efforts in this part of the research concentrated on determining the processing window for the parametric experiments. That is a parameter space was sought for the each parameter, whose combinations would yield energy density values between a lower limit (high porosity) and an upper limit (low porosity).

It is helpful to remind that in standard applications in EOSINT P380, the laser power is set as 38.2 W, the hatching distance is 0.30 mm and the laser speed is 4500 mm/s. (Appendix B)

### 3.1 Producing High Porosity Parts in SLS

For achieving high porosity in built parts, the parameter combination, with which the energy density exposed to the part is minimum, is sought. That is when the hatching distance and laser speed are maximum and the laser power is minimum. If the energy given is too low, then there are two possible issues facing the production of the parts.

The first issue concerns poor part strength. At low energy density some powder may not melt, leading to incomplete fusion between layers and hence low part strength [11].

The second issue concerns the **curling** phenomenon. During the production of the parts in SLS, residual stresses are generated on the part because of the temperature difference between the layers of the part itself (temperature gradient

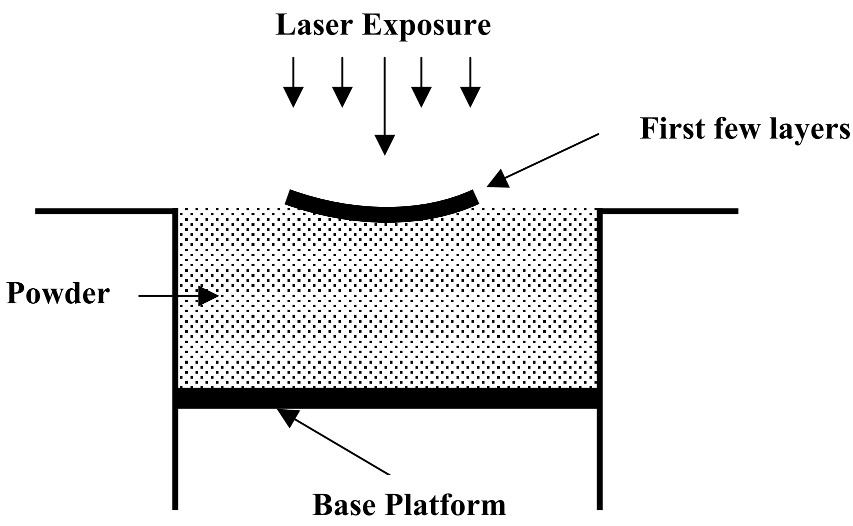


**Figure 3.1: Curling Effect on the beginning layers**

in the z direction) and between the laser exposed sections of the part and surrounding unexposed powder. These stresses can be very high and cause compact warping of the part during production [26]. This warping is called as **"curling"**. While curling is present in all layers, however it is more prominent in beginning layers (Figure 3.1). This also affects the following layers and finally the whole dimensional accuracy. As a result, for reducing the amount of deformation on the parts, one should orient the part geometry such that the cross-section of the initial layers are minimized [27].

The curling is directly related to the energy density. The curling decreases as the energy given to the part increases.

The parts which were analyzed in the current study needed to be designed and built in order to minimize any curling effects. During the trial production runs, in some parameter combination (laser power + hatching distance + laser scan speed) there happened such an intense curling that the part swept away by the recoater during the motion of the recoater between the powder bins.

In the trial studies for high porosity parts, the laser speed and hatching distance were increased and the laser power was decreased as much as possible to determine the upper porosity limit, i.e. the processing conditions for lowest energy density. In the machine specifications of EOSINT P380, because of the capacity of the servomotor of the laser-scanning mirror, it has been noted that the maximum value for the laser speed is 5000 mm/s and in the process software a value greater than 5000 mm/s cannot be entered for the laser speed. Thus before the trial runs, the maximum laser speed was known and in all trials for producing high porous part, the laser speed was set as 5000 mm/s.

The first parameter combination tried for the high porosity limit was 22.9 W laser power, 0.50 mm hatching distance and 5000 mm/s laser speed, which resulted in extreme curling. Increasing the laser power to 25.5 W, while keeping the other parameters same, still resulted in extreme curling. When the hatching distance was decreased to 0.45 mm, in addition to the above increase in laser power, a considerable amount of curling was still present. Finally, when the parameters were set as 28.15 W laser power, 0.45 mm hatching distance and 5000 mm/s laser speed, the curling of the part was observed to be at an acceptable level. This process combination has been chosen as the limit on the processing window for the highest porosity.

### 3.2 Producing Low Porosity Parts in SLS

In determining the process parameter combination for the low porosity limit in the processing window, the degradation of the material under high energy levels was sought. When the parts were sintered under very high energy levels, smoke was observed during laser exposure, which is a sign of degradation.

As a first try, a parameter combination of 41.4 W laser power, 3000 mm/s laser speed and 0.25 mm hatching distance were set. In this configuration intensive smoke was observed during the laser scan.

Further studies involving characterization of porous parts through Computed Tomography (CT) (Section 4.3.1) has shown that when the material degraded due to excessive energy, the part porosity actually increased compared to an undegraded part with lower energy density exposure. Thus for the lower limit on part porosity in the processing window, a parameter combination with as

**Table 3.1: Variation of Parameters in Determining Low Porosity Limit**

| | Laser power (W) | Hatching Distance (mm) | Laser Speed (mm/s) |
|---|---|---|---|
| 1st observation | 39.45 | 0.25 | 2900,3100,3300,3500,3700,3900,4100,4500 |
| 2nd observation | 39.45 | 0.3 | 2900,3100,3300,3500,3700,3900,4100,4500 |
| 3rd observation | 38.22 | 0.3 | 2900,3100,33003500,3700,3900,4000,4100 4200,4300,4400,4500 |

high a resultant exposure density exposure as possible without any degradation should be sought. As smoke generation is the major sign of degradation, smoke observation experiments were carried out for this purpose. In these experiments the parameters, laser power, laser speed and the hatching distance were modified step by step to find out the highest energy density with no smoke generation. The parameter variations are presented in Table 3.1. Figure 3.2 presents the results of this study. Each data point in Figure 3.2 represents a different parameter combination of each observation. The observations were done by varying the laser scan speed at a given laser power and hatching distance. For each observation, the parts that exhibit heavy smoke, light smoke or no smoke are marked with different markers on Figure 3.2. For each parameter combination the energy density is calculated with Equation 3.1.

Of all parameter combinations tried, that did not exhibit any smoke, the combination of 38.22 W laser power, 0.3 mm hatching distance and 4000 mm/s laser speed exhibited the highest energy density (Figure 3.2). Thus the low porosity part limit is determined as such.

Figure 3.3 presents the processing window, comprised of upper and lower limits of the three processing parameters, laser power, hatching distance and laser speed. The relations between processing parameters and the resulting porosity will be sought within this window.

In developing such relations, the major issue is to measure the porosity of the parts, as the reliability of the results of these mathematical relations' results

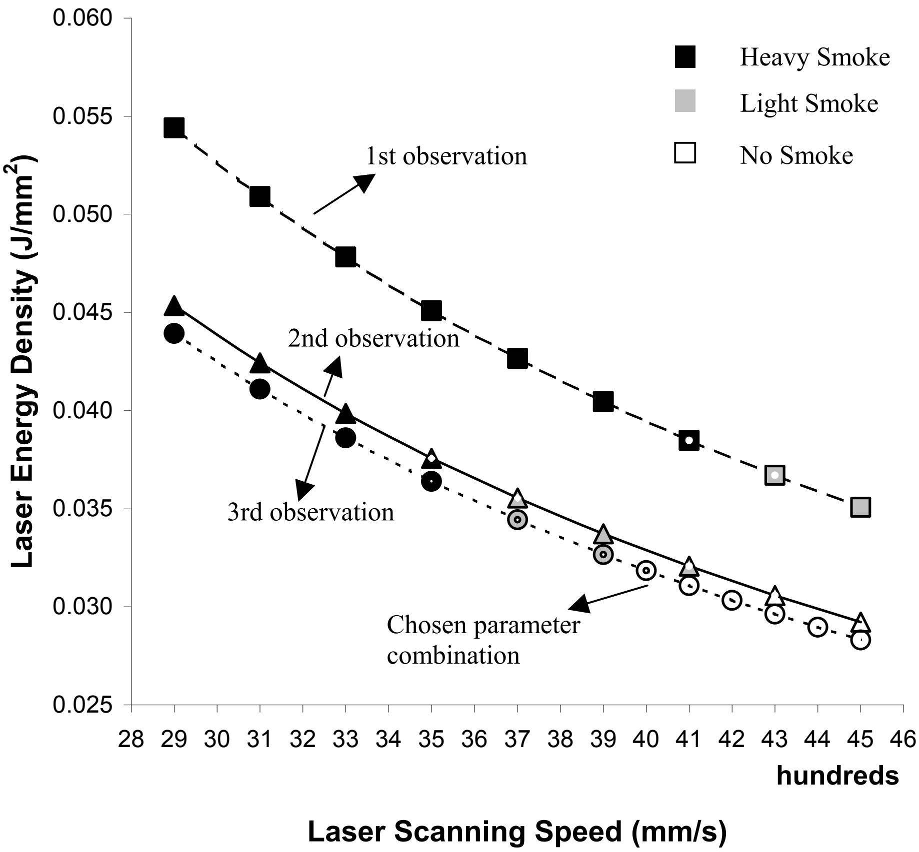


**Figure 3.2: The results of the smoke observation experiment**

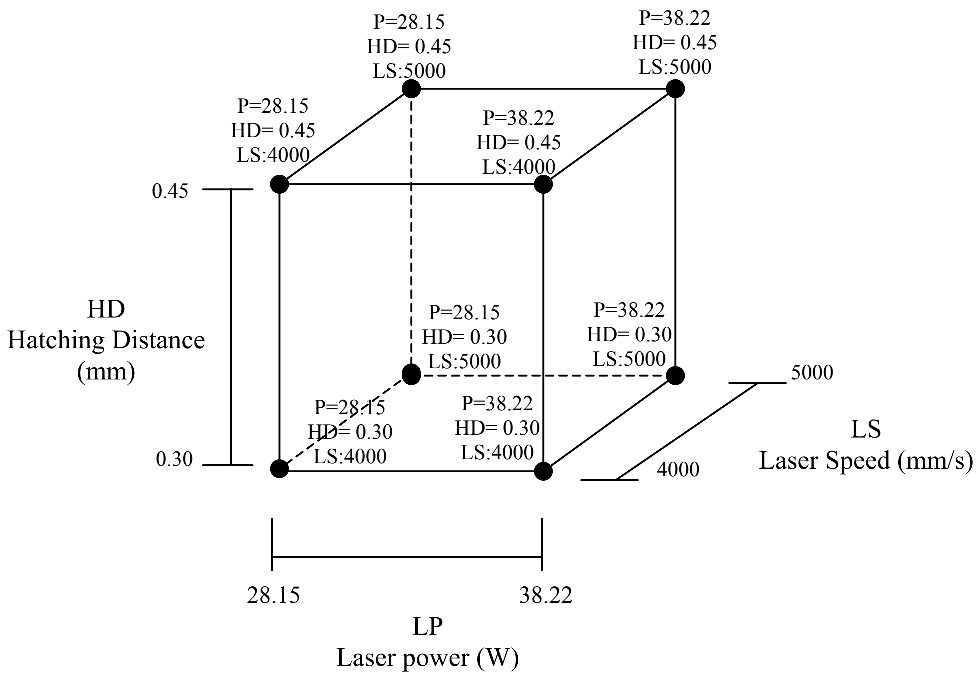


**Figure 3.3: Processing window for the design of experiments**

depends on the accuracy with which porosity can be measured. The next section presents these efforts.

## 3.3 Characterization of the Porosity of Laser Sintered Parts

### 3.3.1 Computed Tomography (CT) for Macroscopic Porosity

As Computed Tomography (CT) is a non-destructive measurement method to analyze the porosity variations inside and to measure macro porosity of the parts, at first the goal was to use CT scan analyses for characterization of the porous structures in the study. For that the CT scanner in the Petroleum and Natural Gas Engineering Department was used.

CT is a technique for digitally cutting a specimen using X-rays to reveal its interior details. A CT image is typically called a *slice*, and a slice corresponds to a certain thickness of the object being scanned. Therefore, a CT slice image is composed of *voxels* (volume elements) [29].

When a CT scanner is operated, X rays penetrate a thin volumetric slice of an object at different angles as the X-ray source rotates around the object or the object rotates around itself. A series of detectors then records the transmitted X-ray intensity. Thus for each voxel different X-ray attenuations are made available for the mathematical reconstruction of the images. Then with the special algorithm, the image is digitally reconstructed. During this reconstruction, the attenuation coefficients of each voxel are normalized with respect to the attenuation coefficient of water and converted into corresponding numerical values, CT numbers, for each voxel. Thus the CT number of water is 0 and CT values of the parts, which are denser than water, are positive and vice versa.

The CT number values obtained after the scan is directly related with the density of the particles. As the density of the part increases (i.e. porosity decreases) the CT number obtained after the scan increases [29].

The CT number analysis of the parts is done with special software of the scanner. For the analysis, in the software, a measurement circle is drawn and this circle is traveled on to the different locations to measure the CT number. During this travel the software dynamically shows you the mean and the standard deviation (STD) of the CT number in the location that are enclosed by the measurement circle. The diameter of the measurement circle can be modified depending on the section that is wanted to analyze.

Assessment of the porosity of the part scanned is possible once the CT numbers are measured. The following equation is used for that.

$$CT_{sample} = (1-\phi)CT_{material} + \phi CT_{air} \tag{3.3}$$

where $CT_{sample}$ is the $CT$ number of the sample to be scanned, $CT_{material}$ is the $CT$ number for the fully homogenous material (without any pore) , which the sample is made of, and $CT_{air}$ is the $CT$ number for the air inside of the pores and $\phi$ is the porosity.

After some modifications in Equation (3.3):

$$\phi = \frac{(CT_{sample} - CT_{material})}{(CT_{air} - CT_{material})} \tag{3.4}$$

The issue with the Equation (3.4) is that, for the calculation of the porosity with CT analyses, it is needed to know the $CT$ number for the fully homogenous part, $CT_{material}$, with no pores. Thus in the study, before performing CT analyses, it is tried to achieve a fully homogenous part with PA 2200. The first method considered for this was the hot pressing (Figure 3.4). For that the press in the

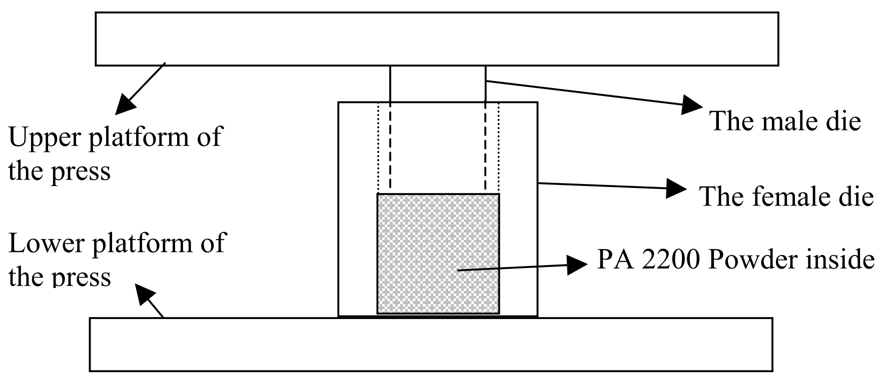


**Figure 3.4: Hot Pressing of the PA 2200**

**Figure 3.5: Hot Press used to produce fully homogenous part**

plastics laboratory of the Chemistry Department of METU was used (Figure 3.5). In this press, there are electrical resistances inside the upper and lower platform and when the power is switched on, first the platforms are heated through these resistances, and then as the dies got contact with the platforms, the heat energy is transformed to the dies.

To compensate for the losses of heat energy, as the hot pressing takes place in open environment, although it was known that the melting temperature of PA 2200 is around 184 Celsius, the temperature of the press was arranged to be its maximum value, 300 Celsius.

The die set for the hot pressing was made of steel. It is composed of simple cylinder (the male die) and annular (the female die). The dimensions of the male and female dies were designed on the basis of the stroke capacity of the hot press and the desired dimensions of the aimed fully homogenous part. The stroke capacity of the press used in this study was 150 mm. Thus the height of the female die plus the height of the male die were designed to be 130 mm (50 mm + 80 mm), which is less than the stroke capacity (Figure 3.6).

After the hot pressing, it was seen the powder that are closer to the die surfaces are melted but the powder, which are close to the die center, did not melt. This shows that, the temperature control over the die and hot press was

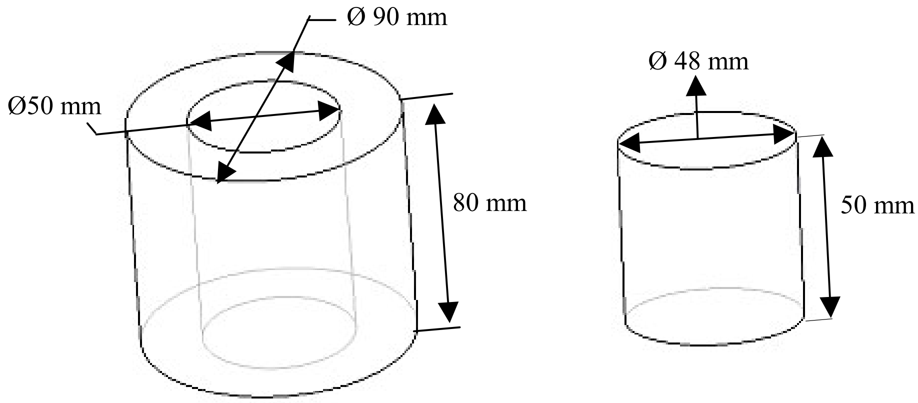


(a) The Female Die b) The Male Die

**Figure 3.6: The die set for the hot pressing**

insufficient to yield an appropriate processing configuration to obtain homogenously melted powder

Since the intended fully homogenous parts could not be achieved with the hot pressing machine in METU Plastics Laboratory, a search has been conducted to find a hot pressing machine or a compression molding system in companies and in other facilities of METU. However for the amount of powder to be molded an available machine in a willing company could not be found

Next the idea of casting the powder in an oven (a closed environment) was considered to obtain a fully solid part. For that an electrical oven is used in the plastics laboratory of the Chemistry Department (Figure 3.6).

The temperature of the oven was adjusted to 300 Celsius. When the temperature in the oven reaches 300 Celsius, three 100 ml bottles with 20 ml PA 2200 powder inside in each were put into the oven. Around one hour is waited for all powders to melt. After 1 hour the bottles are taken out from the oven and first the melted plastic solution is mixed with a wooden spoon and secondly another 20 ml powder is putted, in each bottle, on the previous melted powder. These steps were repeated until 100 ml bottles are filled. When the bottles are filled, the oven is switched of and left for cooling one night while the bottles are still inside. This was done to prevent the sudden cooling of the plastic solution.


**Figure 3.7: The electrical oven used for casting**

Next day, the cooled bottles filled with plastic were taken out of the oven and first the bottle surrounding the plastic part was broken and secondly the plastic parts were machined into cylinder shape with 15 mm diameter and 15 mm height. During the machining of the first and second part there were no pores observed on the part but in the last part, a small pore has been observed on the bottom side of the part.

The sample parts produced with SLS for the CT analysis were designated depending on their shape, production method and type as shown in Table 3.2. The first letter in the designations stands for the shape of the sample part, A for annular shape, F for full cylinder. The second letter stands for the production method, S for SLS, C for casting. Finally the third letter resembles the type of the part: S stands for the standard part of EOSINT P380, L for the low porosity part and H for the high porosity part. The parameter combinations, with which these parts were produced, is listed in Table 3.2. As there were three casting parts, in the designations of these parts, the numbers 1, 2 and 3 were used.

As it is mentioned before, the casting parts (FC1, FC2, FC1 were machined into a cylindrical shape with 15 mm diameter and 15 mm height. Similarly the standard part (FSS) was also machined into the same shape with same dimensions before the CT scan.

**Table 3.2: Sample Parts Produced for the First CT Analysis**

| Part Designation | Geometry | Production Method and Specifications |
|---|---|---|
| FSS | 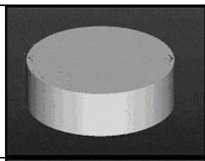 | SLS (Standard configuration)<br>LP: 38.2 W<br>HD: 0.30 mm<br>LS: 4500 mm/s |
| FC1<br>FC2<br>FC3 | 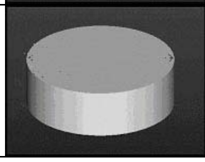 | Casting |
| ASL | 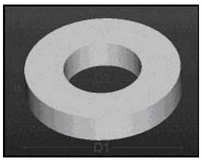 | SLS (Low porosity configuration)<br>LP: 28.15 W<br>HD: 0.25 mm<br>LS: 3000 mm/s |
| ASH | 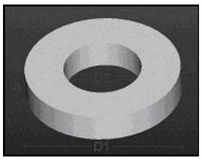 | SLS (High porosity configuration)<br>LP: 28.15 W<br>HD: 0.45 mm<br>LS: 5000 mm/s |

The high and low porous parts (ASL, ASH, respectively) were designed in an annular shape. The inner and outer diameter is 20 mm and 60 mm, respectively and the height was 15 mm (Figure 3.8). The reason that ASL and ASH parts were designed in annular shape was that by placing the molded parts or the standard part on the wall of the inner hole, two different types of part could be scanned in a

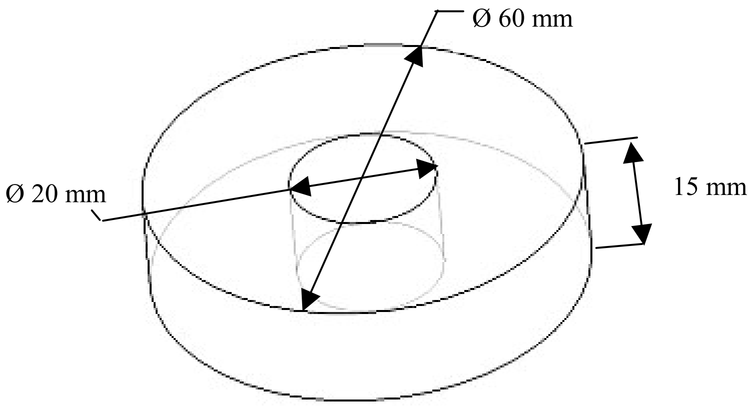


**Figure 3.8: The dimensions of annular ASL and ASH parts**

**Table 3.3: The Results of the First CT Scan**

| | Mean CT | STD of CT |
|---|---|---|
| **FC1** | 29.8 | 22.5 |
| **FC2** | 19.5 | 6.7 |
| **FC3** | -1.2 | 31.2 |
| **ASH** | -333.7 | 8.5 |
| **ASL** | -83.2 | 5.9 |
| **FSS** | -62.7 | 4.8 |

single scan, as shown in Figure 3.9. In the shot shown in Figure 3.9, ASL part and the FM3 part (placed at the center) was analyzed together.

The mean CT numbers and the standard deviations of the CT numbers for all parts scanned in the first CT scan have been shown in Table 3.3. From these results, as the CT analysis gave different CT values for all the parts scanned, the main conclusion obtained was that, CT was able to detect the differences between different types of parts.

When the results of the casting parts (FC1, FM2, FM3) were compared in Table 3.3, it is seen that for all these parts there are different mean CT values and the STD of CT is very large when compared with the mean CT for each, which shows that these parts are not homogenous. Moreover as seen from Figure 3.9, during the analysis, in one of these reference parts, a very large inner pore was observed in the interior of the part. These have leaded us to conclude that, these casting parts cannot be used as reference fully homogenous part for the macro porosity analysis with CT.

In contrast to molded parts, the STD of the CT values for the ASH, ASL and FSS parts turned out to be very small when compared to their mean CT values, which means that the homogeneity of parts produced in SLS are superior.

As previously expected, the mean CT of the high porous part (ASH) happened to be the smallest (-333.7) when compared with low porous (ASL) and standard part (FSS), which means that the low porous and the standard part are

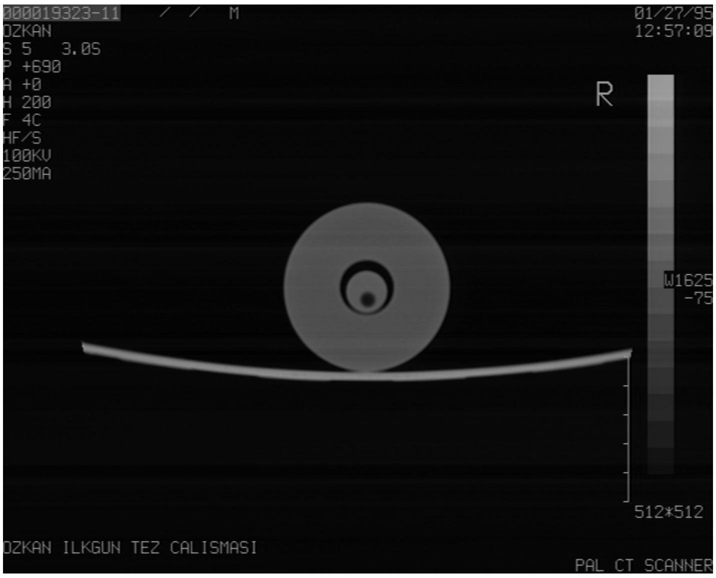


**Figure 3.9: The CT shot taken while ASL and FC3 were analyzed together**

denser than the high porous part. The interesting result was that, the mean CT for the low porous part, ASL, (-83.2) was smaller than the standard part, FSS, (-62.7).

Before the study, it was expected that, as the low porous part (ASL) was produced with a higher energy density than it was for the standard part (FSS), the low porous part should be denser than the standard part and the CT value of the low porous part would be greater. However the result turned out to be the opposite. A similar result was found in [11], where the cause was attributed to the degradation of the material during the production of the low porous part. As it is mentioned in Section 3.2, excessive amount of smoke was observed during the laser exposure on the low porous part. It is believed that the degradation was most severe on the layer surface where the powder particles were in direct contact with the laser beam. The smoke or gases generated from the surface would escape easily. However the laser beam might penetrate through the gaps between the powder particles and reach a deeper section within the layer, therefore, degradation of polymer below the surface is also possible. If the gaps were sealed off quickly due to efficient melting of the polymer, the gases generated at a later stage of the degradation process would be trapped and these trapped gases expand the voids, result in increase in the porosity and reduction in density.

In the light of this, it is understood that for achieving lowest porosity, a parameter combination with as high a resultant exposure density exposure as possible without any degradation should be sought (Section 3.2).

### 3.3.2 CT for Detecting Variations within Part Porosity

Since fully homogeneous parts with PA 2000 could not be produced in the study, CT could not be used for measuring the macro porosity of the sintered parts. However, as mentioned below, CT analyses were used as a characterization method for detecting variations in part porosity within the part.

To see the porosity variation within the scanned sections of the parts, different measurements were taken at different locations in the scanned sections. During the analysis of the ASH and ASL, in the process software of the CT, the measurement circles were placed at four different locations as seen in Figure 3.10.

In Table 3.4, the results of the four measurement locations on ASH and ASL parts are given. The CT results of these parts shown in Table 3.3 were, in fact, the average of these four measurement locations. From Table 3.4 it is seen that, for each part (ASH and ASL), the measured values of the CT number do not vary between different measurement locations. Thus it is detected that the porosity does not vary between different locations of the scanned sections.

To see the porosity variation between the sections of the part, two different measurements were taken at different sections of the ASH, ASL and FSS parts. As seen from the results of each part, (Table 3.5) there is almost no variation in

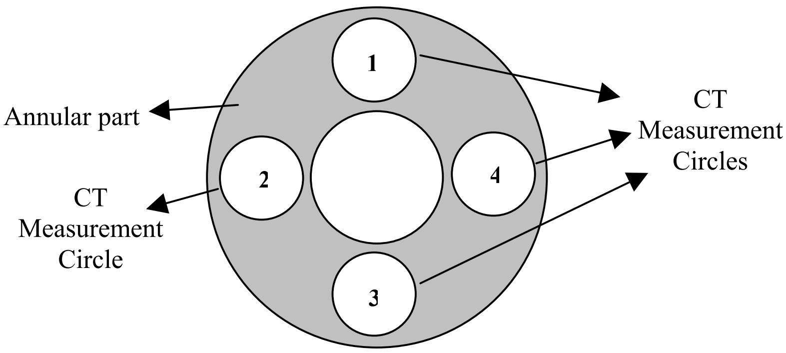


**Figure 3.10: The measurement locations on the ASH and ASL parts during the CT analysis**

**Table 3.4: The CT Measurements on the ASH and ASL Parts**

| | ASH | | ASL | |
|---|---|---|---|---|
| | Mean CT | STD | Mean CT | STD |
| Location 1* | -332.8 | 8.6 | -83.2 | 4.5 |
| Location 2* | -332.4 | 7.5 | -84.1 | 6,9 |
| Location 3* | -335.6 | 9.2 | -83.8 | 5.8 |
| Location 4* | -333.8 | 8.8 | -81.6 | 4.3 |

*** For locations see Figure 3.9**

**Table 3.5: The Variation of CT Values between the Sections of the Parts**

| | First Section | | Second Section | |
|---|---|---|---|---|
| | Mean CT | STD | Mean CT | STD |
| ASH | -333.65 * | 8.5* | -331.4 * | 7.8 * |
| ASL | -83.8 * | 5.9 * | -83.95 * | 6.0 * |
| FSS | -62.7 | 4.8 | -61.6 | 4.2 |

*** Average of the four measurement locations**

**Table 3.6: Sample Parts Produced for the Second CT Analysis**

| Part Designation | Geometry | Production Method and Specifications |
|---|---|---|
| ASL | 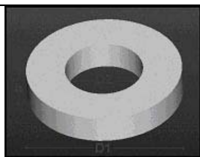 | SLS (Low porosity configuration)<br>LP: 28.15 W<br>HD: 0.25 mm<br>LS: 3000 mm/s |
| FSL | 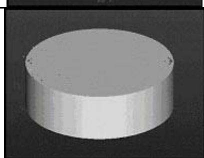 | SLS (Low porosity configuration)<br>LP: 28.15 W<br>HD: 0.25 mm<br>LS: 3000 mm/s |
| FSH | 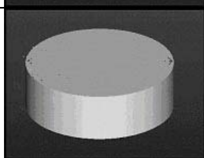 | SLS (High porosity configuration)<br>LP: 28.15 W<br>HD: 0.45 mm<br>LS: 5000 mm/s |
| ASS | 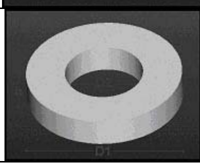 | SLS (Standart configuration)<br>LP: 38.2 W<br>HD: 0.30 mm<br>LS: 4500 mm/s |

CT values between the sections, which means that, the porosity do not vary between sections of the laser sintered parts, also.

In the CT study, a second CT analysis was performed to check the repeatability of the SLS process and to see whether the part geometry has an effect on the part porosity. The designed parts for the second CT analysis are shown in Table 3.6.

To see the repeatability of the SLS process, a new low porosity part (ASL) was produced with the same shape and with the same parameter configuration as in the first scan. The comparison of the result of the first and the second scans of ASL part are shown in Table 3.7. It is seen that, the CT values of the ASL part do not differ between the first and second scan, thus the repeatability of the SLS process was proven.

For the second scan, three new parts were produced to see whether the part geometry has an effect on the resultant part porosity. The first one was the full cylinder high porosity part (FSH), the second was the full cylinder low porosity part (FSL) and finally the third one is annular standard part (ASS).

In Table 3.8, Table 3.9 and Table 3.10, the comparisons of the CT values of the different shaped low porosity, high porosity and standard part, respectively, are given. When these tables are examined it is seen that, part geometry has no effect on the porosity, as the CT values of the same type but different geometry parts do not differ from each other.

**Table 3.7: The CT Values of the Same ASL Parts in the First and Second CT Scan**

| | The First Scan | | The Second Scan | |
|---|---|---|---|---|
| | **Mean CT** | **STD** | **Mean CT** | **STD** |
| **Location 1*** | -83.2 | 4.5 | -84.6 | 5.4 |
| **Location 2*** | -84.1 | 6.9 | -82.8 | 5.8 |
| **Location 3*** | -83.8 | 5.8 | -83.7 | 6.3 |
| **Location 4*** | -81.6 | 6.4 | -82.1 | 6 |

*** For locations see Figure 3.9**

**Table 3.8: The CT Values of the ASH and FSH Parts**

| ASH (First Scan) | | | | FSH (Second Scan) | | | |
|---|---|---|---|---|---|---|---|
| First Section | | Second Section | | First Section | | Second Section | |
| Mean CT | STD | Mean CT | STD | Mean CT | STD | Mean CT | STD |
| -333.6 * | 8.5 * | -331.4 * | 7,8 * | -331 | 9.8 | -329.4 | 9.2 |

*** Average of the four measurement locations**

**Table 3.9: The CT values of the ASL and FSL parts**

| ASL (First Scan) | | | | FSL (Second Scan) | | | |
|---|---|---|---|---|---|---|---|
| First Section | | Second Section | | First Section | | Second Section | |
| Mean CT | STD | Mean CT | STD | Mean CT | STD | Mean CT | STD |
| -83.8 * | 5.9 * | -84.0 * | 6.0 * | -83.6 | 6.5 | -81.4 | 7.2 |

*** Average of the four measurement locations**

**Table 3.10: The CT values of the FSS and ASS parts**

| FSS (First Scan) | | | | ASS (Second Scan) | | | |
|---|---|---|---|---|---|---|---|
| First Section | | Second Section | | First Section | | Second Section | |
| Mean CT | STD | Mean CT | STD | Mean CT | STD | Mean CT | STD |
| -62.7 | 4.8 | -61.6 | 4.2 | -62.3 * | 5.6 * | -62.2 * | 5.5 * |

*** Average of the four measurement locations**

### 3.3.3 Characterization with Apparent Mass Density Measurements

After it was understood that the characterization of porosity of laser sintered parts could not be done with CT analysis, then it was concluded to use apparent mass density measurements for the characterization.

For that first the sample cylindrical parts are produced in SLS, with the parameter combinations of the process window (Figure 3.3) and than the apparent mass densities of these parts are measured with mass volume ratio.

The dimensions of the test parts were measured with the Coordinate Measuring Machine, in the METU/BİLTİR CAD/CAM and Robotics Center, and the volume of the test parts were calculated in accordance with these measured dimensions. Before the measurements with CMM, the parts were machined with lathe machine, to bring the dimensions of the test parts into exact values and to enhance the surface quality of the parts for better measurements in CMM.

After the calculation of the volume for each test part, then the mass of these machined parts were measured with a high sensitivity (0.0001 g) scale, in the Chemistry Department of METU.

For every parameter combinations, two replicates were produced, to decrease the experimental error.

In Table 3.11 the measured mass apparent density values for each parameter combination are shown. As seen from the table, density values differ depending on the parameter combination. In Table 3.12, the CT values for each parameter

**Table 3.11: The Density Measurements for Each Parameter Combination**

| **Parameter combination that the part was produced with** | **Weight (g)** | | **Volume cm3** | | **Apparent Mass Density (g/cm3)** | |
|---|---|---|---|---|---|---|
| | Replicate 1 | Replicate 2 | Replicate 1 | Replicate 2 | Replicate 1 | Replicate 2 |
| P=28.15 W HD= 0.30 mm LS=4000 mm/s | 3.935 | 3.915 | 4.119 | 4.118 | 0.9553 | 0.9508 |
| P=38.22 W HD= 0.30 mm LS:=4000 mm/s | 3.988 | 4.001 | 4.133 | 4.119 | 0.9651 | 0.9713 |
| P=28.15 W HD= 0.30 mm LS=5000 mm/s | 3.601 | 3.630 | 4.117 | 4.110 | 0.8746 | 0.8832 |
| P=38.22 W HD= 0.30 mm LS=5000 mm/s | 3.913 | 3.945 | 4.114 | 4.123 | 0.9512 | 0.9568 |
| P=28.15 W HD= 0.45 mm LS=4000 mm/s | 3.145 | 3.196 | 4.114 | 4.137 | 0.7644 | 0.7726 |
| P=38.22 W HD= 0.45 mm LS=4000 mm/s | 3.866 | 3.862 | 4.144 | 4.133 | 0.9330 | 0.9345 |
| P=28.15 W HD= 0.45 mm LS=5000 mm/s | 2.878 | 2.901 | 4.136 | 4.118 | 0.6960 | 0.7044 |
| P=28.15 W HD= 0.45 mm LS=5000 mm/s | 3.183 | 3.187 | 4.126 | 4.114 | 0.7713 | 0.7747 |

*** P is the laser power, HD is the hatching distance and LS is the laser speed**

combination are shown. When the apparent mass density vs. CT graph is drawn, it is seen that there is almost a linear relationship with CT and apparent mass density and as the apparent mass density increases the CT value decreases (Figure 3.11), as expected.

**Table 3.12: The CT Measurements for Each Parameter Combination**

| Parameter combination that the part was produced with | CT |
|---|---|
| P=28.15 W<br>HD= 0.30 mm<br>LS=4000 mm/s | -89 |
| P=38.22 W<br>HD= 0.30 mm<br>LS=4000 mm/s | -55 |
| P=28.15 W<br>HD= 0.30 mm<br>LS=5000 mm/s | -130 |
| P=38.22 W<br>HD= 0.30 mm<br>LS=5000 mm/s | -78 |
| P=28.15 W<br>HD= 0.45 mm<br>LS=4000 mm/s | -258 |
| P=38.22 W<br>HD= 0.45 mm<br>LS=4000 mm/s | -87 |
| P=28.15 W<br>HD= 0.45 mm<br>LS=5000 mm/s | -335 |
| P=28.15 W<br>HD= 0.45 mm<br>LS=5000 mm/s | -270 |

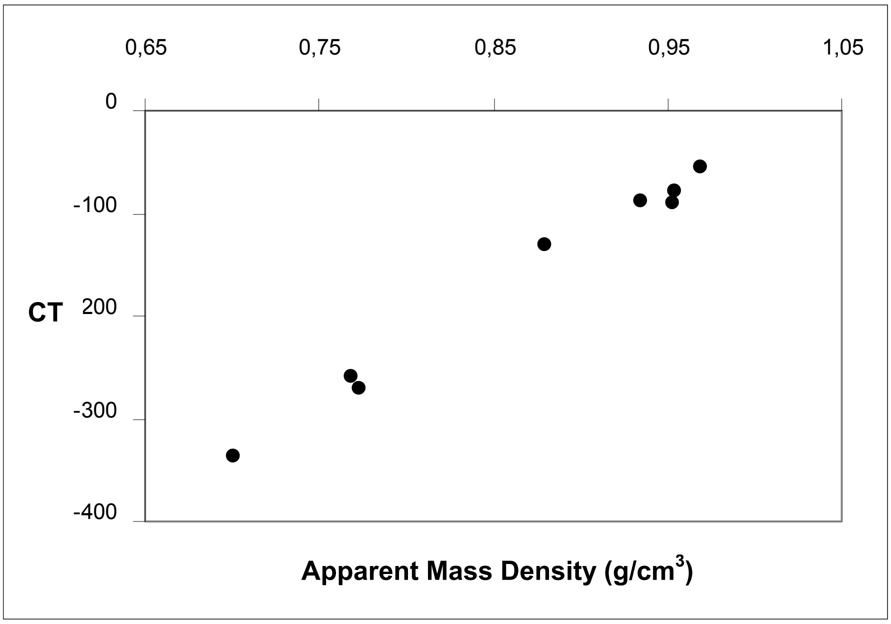


**Figure 3.11: The CT vs. Density graph of the parts produced with the parameter combinations in the process window.**

# CHAPTER 4

# DESIGN OF EXPERIMENTS

In Chapter 3, the main process parameters that were deemed to be most effective on apparent mass density (and hence its porosity) were the laser power, laser scanning speed and hatching distance. In this chapter, a mathematical relation will be developed between these parameters and the resulting part apparent mass density of the parts. The relation will be based on a series of parametric experiments. The experiments are designed with the $2^3$ factorial design method, the details of which are explained in the following.

## 4.1 The Advantage of Factorial Design of an Experiment

The strategy of experimentation that is used extensively in practice is the **one factor at a time approach**. This method consist of selecting a start point, or **baseline** set of levels, for each factor considered, then successively varying each factor over its range with the other factors held constant at their baseline level. The major disadvantage of the one factor at a time strategy is that, it fails to consider any possible **interaction** between the factors. An **interaction** is the failure of the one factor to produce the same effect on the response at different levels of another factor [30]. The interactions between the factors will be further explained in Section 4.2.

In general, factorial designs are the most efficient experimental method for the types of experiments when there is an interaction between the factors [30]. By a factorial design it is meant that in each run of the designed experiment, all possible combinations of the levels (values) of the factors (parameters) are investigated. That is, the factors are varied together, instead of one at a time. For example, if there are “a” levels of factor A and “b” levels of factor B, each run of the experiment contains all “ab” treatment combinations. This way, at several levels of the factors the main effects of each factor and interaction between factors are estimated which yields conclusions that are valid over a range of experimental conditions.

### 4.2 The Main Effects and Interaction Effects

The **effect** a factor (laser power, laser scan speed or hatching distance in this study) is defined to be the change in response (apparent mass density, in our study) produced by a change in the level of the factor. This is called **main effect** because it refers to the primary factors of interest in the experiment. For example, in Figure 4.1, a simple two-factor factorial design experiment is shown, with the response values shown at the corners. In the experiment each factor is designed with two levels. These levels are called “low” and “high”. The main effect of factor A in this two level design can be thought of as the difference between the average response at the low level of A and the average response at the high level of A, such as

$$A = \frac{40+50}{2} - \frac{20+30}{2} = 20 \tag{4.1}$$

That is increasing factor A from the low level to the high level causes an

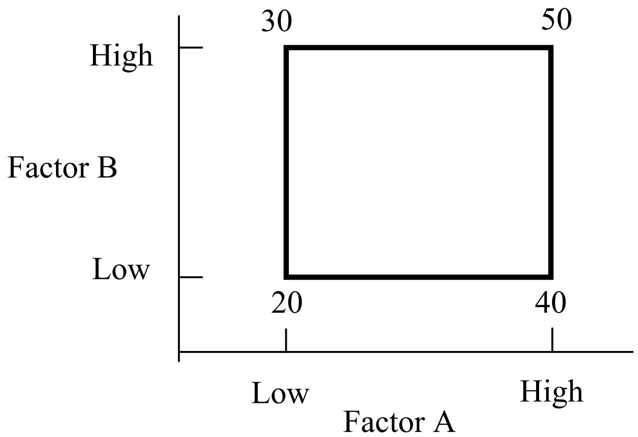


**Figure 4.1: A two factor factorial experiment, with the response shown at the corners**

**average response increase** of 20 units. Similarly the main effect of B is,

$$B = \frac{30+50}{2} - \frac{20+40}{2} = 10 \tag{4.2}$$

From Figure 4.1, it is seen that, the effect of the increase in the level of Factor B from low to high level on the response does not depend on the level of Factor A. At the high level of Factor A ($A^+$), the increase in the level of Factor B from low to high level causes an increase of 10 (50-40) units in the response, similarly, at the low level of Factor A ($A^-$), it causes an increase of 10 (30-20) units in the response. The same is also valid for factor A, when the effect of the increase in the level of Factor A from low to high on response is examined. In this case, there is no **interaction** between the factors in the designed experiment.

In some cases, the difference between one factor is not same at all levels of the other factors. For example, in the two-factor factorial experiment, shown in Figure 4.2, at the high level of factor B ($B^+$), the increase in the level of Factor A from low to high level (A effect) is

$$A = 12 - 40 = -28 \tag{4.3}$$

and at the low level of factor B ($B^-$), the A effect is

$$A = 50 - 20 = 30 \tag{4.4}$$

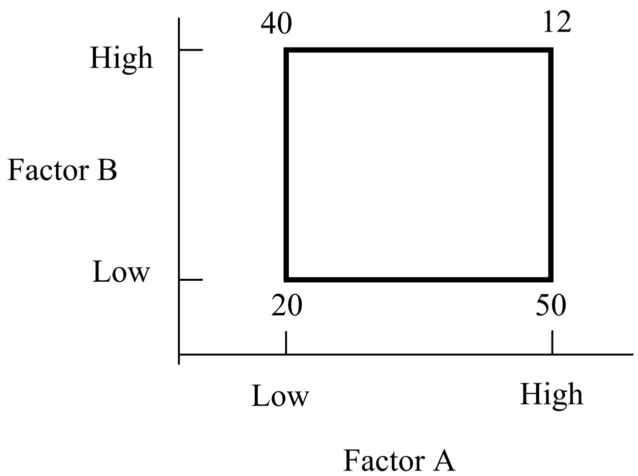


**Figure 4.2: A two factor factorial experiment with interaction**

Because the effect of A depends on the level chosen for factor B, it is seen that there is an interaction between factors A and B. The magnitude of interaction, AB, is the average difference in these two A effects.

$$AB = (-28 - 30)/2 = -29 \tag{4.5}$$

The main effects of the experiment shown in Figure 4.2 can be calculated as

$$A = \frac{50+12}{2} - \frac{40+20}{2} = 1.5 \tag{4.6}$$

$$B = \frac{40+12}{2} - \frac{20+50}{2} = -9 \tag{4.7}$$

The result of this experiment indicates that, the effect of the interaction, AB, on the response is larger than the main effects, A and B. Thus, in designing the experiment and studying the effect of the factors on response, neglecting the interaction between the factors (one factor at a time approach) would result in a serious error.

## 4.3 The $2^3$ Factorial Design

In this study, as an initial approach, $2^k$ factorial design was used to design the experiments. The data obtained from these experiments are to be used in determining a mathematical model to express the relations between the response (apparent mass density) and the three factors (parameters), the laser power, laser speed and hatching distance. The $2^k$ factorial design approach is the simplest among all factorial experimental design methods. Thus, the mathematical models obtained with it are also simple when compared to other more complicated factorial designs ($3^k$ design, for example). However, a complicated design of experiments does not always result in better accuracy of the final established model, thus it was intended to proceed with the simplest design, $2^k$ factorial design approach, and check the validity of the established model with incoming experimental data.

In $2^k$ factorial design, there are only two levels (high and low) for the "k" factors interested. This provides the smallest number of runs with which "k" factors can be studied in a complete factorial design. Because there are only two levels for each factor, in the $2^k$ factorial design it is assumed that the response is approximately linear over the range of the factors chosen.

In the designed experiments of this study, by varying the three factors (the laser power, the laser speed and the hatching distance, k=3) at two levels, the apparent mass density variations of $2^3$=8 sample laser sintered parts (runs) were analyzed.

In the $2^3$ factorial design the levels of the factors can be arbitrarily called, "low" and "high". The treatment combinations in the design can be shown geometrically as a cube as in Figure 4.3.

As seen from Figure 4.3, the high level of any factor in the treatment combination is denoted by the corresponding lowercase letter and the low level of a factor in the treatment combination is denoted by the absence of the corresponding letter. Thus "a" represents the resulting property value at the treatment combination with A at high level and B and C at low level, "ab" represents A and B at the high level and C at the low level. By convention, (1) is used to denote all factors at the low level. At each configuration, experiments may

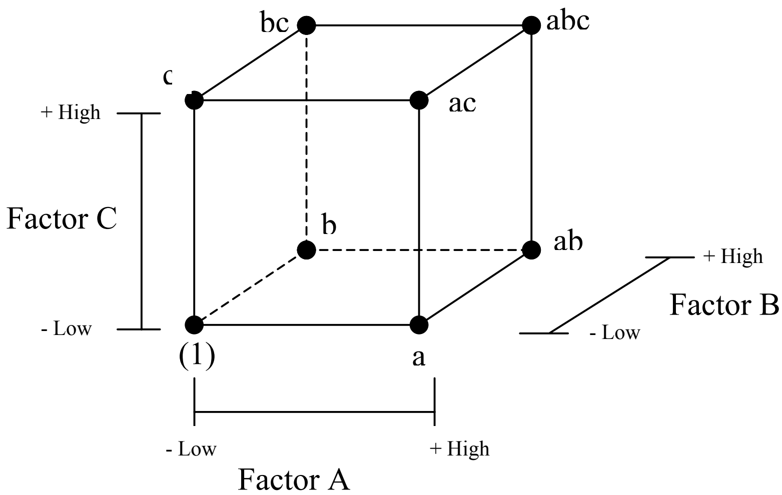


**Figure 4.3- The Factor-Level Space in $2^3$ factorial design**

be repeated, i.e., “n” replicates of the same configuration (for later statistical analysis). Thus, each symbol (e.g. a, b, ab, etc.) denotes to the sum of the “n” responses in that configuration.

In a two level factorial design, the average effect of a factor is defined as the change in response produced by a change in the level of that factor averaged over the levels of the other factors. For instance, the effect of A when B and C are at low level is [a-(1)]/n, where “n” is the number of replicates. Similarly the effect of A when B is at high level and C is at the low level is [ab-b]/n. The effect of A when C is at the high level and B is at the low level is [ac-c]/n. Finally the effect of A when both B and C are at high level is [abc-bc]/n. Thus the average main effect of A is just the average of these four, or

$$A = \frac{1}{4n}\left[a - (1) + ab - b + ac - c + abc - bc\right] \tag{4.8}$$

Using similar logic for estimating the average effects of other factors is:

$$B = \frac{1}{4n}\left[b + ab + bc + abc - (1) - a - c - ac\right] \tag{4.9}$$

$$C = \frac{1}{4n}\left[c + ac + bc + abc - (1) - a - b - ab\right] \tag{4.10}$$

The two factor interaction effects may be computed easily. A measure of the AB interaction is the difference between the average A effects at the two levels of B. By convention, one-half of this difference is called the AB interaction. Symbolically,

| **B** | **Average A Effect** |
|---|---|
| High (+) | $\frac{[(abc - bc) + (ab - b)]}{2n}$ |
| Low (-) | $\frac{[(ac - c) + (a - (1)]}{2n}$ |
| Difference | $\frac{[abc - bc + ab - b - ac + c - a + (1)]}{2n}$ |

Because the AB interaction is the half of this difference

$$AB = \frac{[abc - bc + ab - b - ac + c - a + (1)]}{4n} \tag{4.11}$$

Using similar logic, one can find that:

$$AC = \frac{[(1) - a + b - ab - c + ac - bc + abc]}{4n} \tag{4.12}$$

$$BC = \frac{[(1) + a - b - ab - c - ac + bc + abc]}{4n} \tag{4.13}$$

The ABC interaction is defined as the average differences between the AB interaction for the two different levels of C. Thus

$$\begin{aligned} ABC &= \frac{1}{4n}[(abc - bc) - (ac - c) - (ab - b) + (a - (1))] \\ &= \frac{[abc - bc - ac + c - ab + b + a - (1)]}{4n} \end{aligned} \tag{4.14}$$

In Equations (4.8) through (4.14), the quantities in the brackets in numerators are called **contrasts** in the treatment combinations [30]. A table of the plus and minus signs, such as Table 4.1, can be used to determine the proper sign for each effect, which is then linearly combined with others in a certain treatment combination to calculate the  contrast for a specific factor. The column headings in Table 4.1 are the main effects (A, B and C), and the interactions (AB, AC, BC and ABC). The signs for the main effects are determined by associating a plus with the high level and a minus with the low level of the factor in the corresponding configuration. The row designators are the treatment combinations. Once the signs for the main effects have been established, the signs for the remaining interaction effect columns can be obtained by multiplying the relevant main effect signs for the particular treatment combination in consideration. For instance, to estimate ABC interaction, the contrast is –(1)+a+b-ab-c-ac-bc+abc, which agrees with equation (4.14).

**Table 4.1: Algebraic Signs of the Factor Effect for Calculating Contrasts in the $2^3$ Design**

| | **Factorial Effect** | | | | | | |
|---|---|---|---|---|---|---|---|
| **Treatment Combination** | A | B | AB | C | AC | BC | ABC |
| (1) | - | - | + | - | + | + | - |
| A | + | - | - | - | - | + | + |
| B | - | + | - | - | + | - | + |
| Ab | + | + | + | - | - | - | - |
| C | - | - | + | + | - | - | + |
| Ac | + | - | - | + | + | - | - |
| Bc | - | + | - | + | - | + | - |
| abc | + | + | + | + | + | + | + |

## 4.4 The Designed Density Variation Experiment

The purpose of the experiment is to seek the effect of the laser power, laser speed and hatching distance on the apparent mass density (as a measure of porosity) of the parts produced by Laser Sintering Process will be presented. Large the porosity of the part, the smaller its density will be. The factors are coded as A for the laser power, B for the laser speed and C for the hatching distance. All factors have two levels and the resulting measured property (response) is the apparent mass density.

The high and low values (levels) of three parameters (factors) are tabulated in Table 4.2, which were determined in Chapter 3. During the production of the test parts of the experiment, only these parameters of the EOSINT P380 were modified. All other parameters were kept in their standard values, which are listed

**Table 4.2: Factor Levels (Parameter Values) in the Designed Experiment**

| | Low (-1) | High (+1) |
|---|---|---|
| A (Laser Power, W) | 28,15 | 38,22 |
| B (Laser scan Speed, mm/s) | 4000 | 5000 |
| C (Hatching Distance, mm) | 0,3 | 0,45 |

in Appendix B. In the experiment, to decrease the experimental error in measurements, for every treatment combination (process configuration) two replicates (two test parts with the same process configuration) were produced and analyzed.

The results of the designed experiments are shown in Table 4.3. In the Table, the measured density values of each replicate test part at every process configuration, as well as the replicate sums and averages are presented. The density of the produced test parts produced was calculated by mass volume ratio. The mass of the parts were measured with a high sensitivity (0.0001 g) scale. The dimensions of the test parts were measured with the Coordinate Measuring Machine (CMM), in the METU/BİLTİR CAD/CAM and Robotics Center, and the volume of the test parts were calculated in accordance with these measured dimensions.

The test parts were originally modeled in full cylindrical shape with 20 mm diameter and 30 mm height and the parts were produced in these dimensions with SLS. Afterwards all the parts were machined into dimensions: diameter around 16 mm and height around 20 mm. With the machining the surface quality of the parts

**Table 4.3: The Results of $2^3$ Factorial Design Density Variation Experiment**

| | | **Parameter* Levels** | | | **Measured Apparent Mass Density ($g/cm^3$)** | | | |
|---|---|---|---|---|---|---|---|---|
| Process Configuration | Test Run | A | B | C | Replicate 1 | Replicate 2 | Density Sum ($g/cm^3$) | Density Average ($g/cm^3$) |
| -1 | 1 | -1 | -1 | -1 | 0.955 | 0.950 | 1.905 | 0.953 |
| a | 2 | 1 | -1 | -1 | 0.965 | 0.971 | 1.936 | 0.968 |
| b | 3 | -1 | 1 | -1 | 0.875 | 0.883 | 1.758 | 0.879 |
| ab | 4 | 1 | 1 | -1 | 0.951 | 0.957 | 1.908 | 0.954 |
| c | 5 | -1 | -1 | 1 | 0.764 | 0.773 | 1.537 | 0.769 |
| ac | 6 | 1 | -1 | 1 | 0.933 | 0.934 | 1.867 | 0.934 |
| bc | 7 | -1 | 1 | 1 | 0.696 | 0.704 | 1.400 | 0.700 |
| abc | 8 | 1 | 1 | 1 | 0.771 | 0.775 | 1.546 | 0.773 |

*** Process Parameters: A: Laser Power, B: Laser Scanning Speed, C: Hatching Distance**

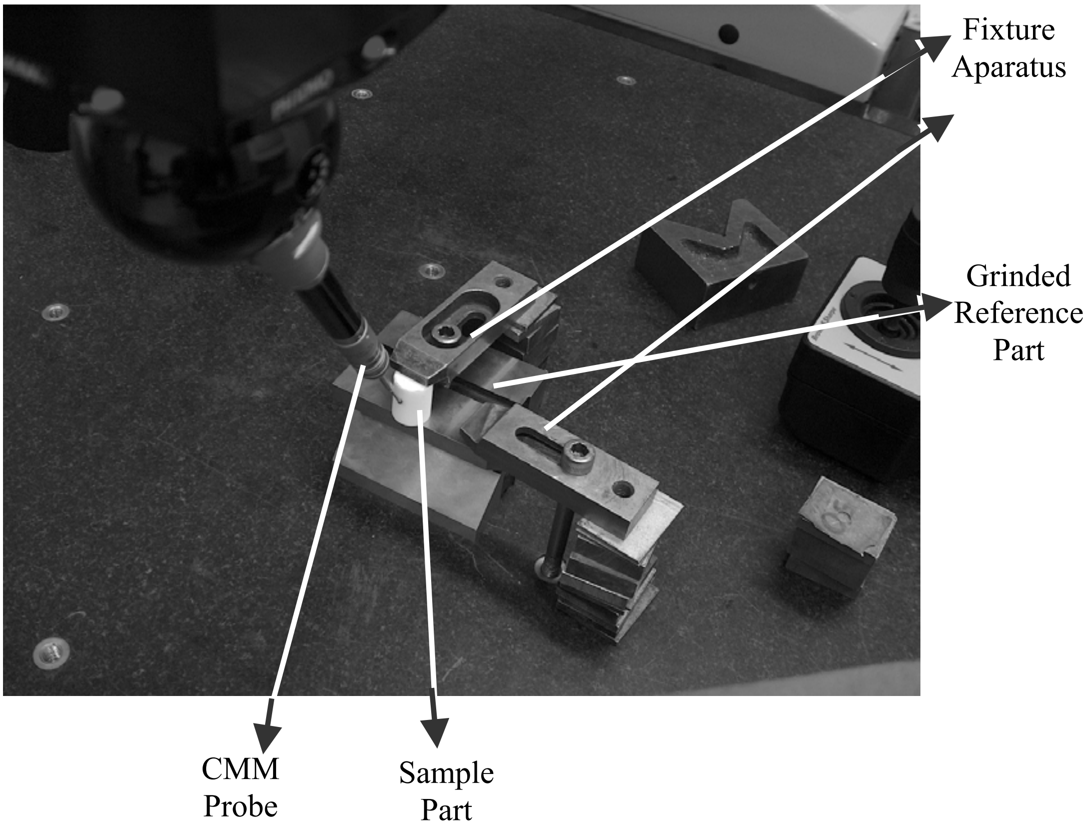


**Figure 4.4. CMM Measurements of the test parts**

were enhanced, also, which results in better measurements with CMM. Before the CMM measurements, the parts were fixed onto a grinded reference part as shown in Figure 4.4.

For all the sample parts, the diameters were measured at three different locations and the average of these is taken. In each diameter location, the probe of the CMM touched the part at different circumferential positins without changing the probe position in Z-axis. Then in the process software of CMM, a circle which passes through these points are constructed and the diameter value is found for that location.

For the height measurements, the average distances between several touched points at the top surface of the test parts and the points on the top surface of the grinded reference part were measured.

For each replicate of the test parts, the measured dimensions (diameter and

**Table 4.4: Dimensions, Volume and Mass of the Test Parts in the $2^3$ Factorial Design Experiment**

| | Parameter* Levels | | | Diameter (mm) | | Height (mm) | | Volume (cm3) | | Mass (g) | |
|---|---|---|---|---|---|---|---|---|---|---|---|
| **Test Run** | A | B | C | R1 | R2 | R1 | R2 | R1 | R2 | R1 | R2 |
| 1 | -1 | -1 | -1 | 16.03 | 16.04 | 20.41 | 20.38 | 4.119 | 4.118 | 3.935 | 3.915 |
| **2** | 1 | -1 | -1 | 16.08 | 16.05 | 20.35 | 20.36 | 4.133 | 4.119 | 3.988 | 4.001 |
| **3** | -1 | 1 | -1 | 16.05 | 16.02 | 20.35 | 20.39 | 4.117 | 4.110 | 3.601 | 3.630 |
| **4** | 1 | 1 | -1 | 16.04 | 16.07 | 20.36 | 20.33 | 4.114 | 4.123 | 3.913 | 3.945 |
| **5** | -1 | -1 | 1 | 16.04 | 16.06 | 20.36 | 20.42 | 4.114 | 4.137 | 3.145 | 3.196 |
| **6** | 1 | -1 | 1 | 16.09 | 16.08 | 20.38 | 20.35 | 4.144 | 4.133 | 3.866 | 3.862 |
| **7** | -1 | 1 | 1 | 16.09 | 16.04 | 20.34 | 20.38 | 4.136 | 4.118 | 2.878 | 2.901 |
| **8** | 1 | 1 | 1 | 16.06 | 16.04 | 20.37 | 20.36 | 4.126 | 4.114 | 3.183 | 3.187 |

*** Process Parameters: A: Laser Power, B: Laser Scanning Speed, C: Hatching Distance**
*** R stands for the replicate**

height), the resulting volume and measured mass are presented in Table 4.4. The density values of in Table 4.3 are calculated with these mass and volume values.

The same results of Table 4.3 are also presented in Figure 4.5, in the parameter factor space. The presented values are the sums of replicate density values.

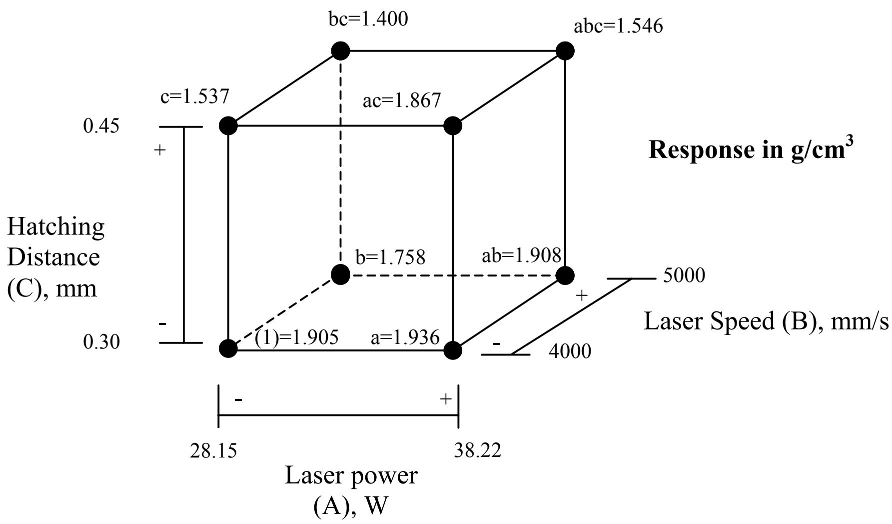


**Figure 4.5: The results of $2^3$ design for the density variation experiment: Replicate test parts density sums at each process configuration**

Using equations (4.8) through (4.14), the main and interaction effects of the process parameters can be calculated as:

$$
\begin{aligned}
A &= \frac{1}{4n}\left[a-(1)+ab-b+ac-c+abc-bc\right] \\
&= \frac{1}{8}\left[1.936-1.905+1.908-1.758+1.867-1.537+1.546-1.400\right] \\
&= \frac{1}{8}\left[0.656\right]=0.082
\end{aligned}
\tag{4.15}
$$

$$
\begin{aligned}
B &= \frac{1}{4n}\left[b+ab+bc+abc-(1)-a-c-ac\right] \\
&= \frac{1}{8}\left[1.758+1.908+1.400+1.546-1.905-1.936-1.537-1.867\right] \\
&= \frac{1}{8}\left[-0.634\right]=-0.079
\end{aligned}
\tag{4.16}
$$

$$
\begin{aligned}
C &= \frac{1}{4n}\left[c+ac+bc+abc-(1)-a-b-ab\right] \\
&= \frac{1}{8}\left[1.537+1.867+1.400+1.546-1.905-1.936-1.758-1.908\right] \\
&= \frac{1}{8}\left[-1.157\right]=-0.145
\end{aligned}
\tag{4.17}
$$

$$
\begin{aligned}
AB &= \frac{1}{4n}\left[ab-a-b+(1)+abc-bc-ac+c\right] \\
&= \frac{1}{8}\left[1.908-1.936-1.758+1.905+1.546-1.400-1.867+1.537\right] \\
&= \frac{1}{8}\left[-0.065\right]=-0.008
\end{aligned}
\tag{4.18}
$$

$$
\begin{aligned}
AC &= \frac{1}{4n}\left[(1)-a+b-ab-c+ac-bc+abc\right] \\
&= \frac{1}{8}\left[1.905-1.936+1.758-1.908-1.537+1.867-1.400+1.546\right] \\
&= \frac{1}{8}\left[0.296\right]=0.0369
\end{aligned}
\tag{4.19}
$$

$$BC = \frac{1}{4n}\left[(1) + a - b - ab - c - ac + bc + abc\right]$$
$$= \frac{1}{8}\left[1.905 + 1.936 - 1.758 - 1.908 - 1.537 - 1.867 + 1.400 + 1.546\right] \quad (4.20)$$
$$= \frac{1}{8}\left[-0.281\right] = -0.035$$

$$ABC = \frac{1}{4n}\left[abc - bc - ac + c - ab + b + a - (1)\right]$$
$$= \frac{1}{8}\left[1.546 - 1.400 - 1.867 + 1.537 - 1.908 + 1.758 + 1.936 - 1.905\right] \quad (4.21)$$
$$= \frac{1}{8}\left[-0.304\right] = -0.038$$

The calculated main effects and interaction effects are tabulated in Table 4.5. When the absolute values of the effects are compared it is seen that, the largest effect is for main effect of the hatching distance, C, -0.145 g/cm$^3$. After the hatching distance, the greatest effects are the main effect of the laser power (0.082 g/cm$^3$) and laser scan speed (-0.079 g/cm$^3$). In addition the effects of laser power-hatching distance, AC, (0.037 g/cm$^3$), laser speed-hatching distance (BC) and the laser power-laser speed- hatching distance (ABC) interactions are also substantial. Whereas laser power-laser speed, AB, interaction, (-0.008 g/cm$^3$) does not appear to have as large an effect on the density.

As it was expected, from the main effect of laser power (A) it is seen that, the increase from low (28.15 W) to high level (38.22) causes an increase of 0.082 g/cm$^3$ in the density. It should be again pointed out that this is the main effect of laser power. The effect of the laser power is also seen in its interactions with laser scan speed and the hatching distance. For instance, the increase of the laser scan speed from low (4000 mm/s) to high level (5000 mm/s) results in -0.079 g/cm$^3$ (main effect of the laser scan speed) decrease in the density. However from the laser power and laser speed interaction, AB, it is seen that, the negative effect of laser scan speed in density is almost compensated by the positive effect of laser speed and the resulting effect of AB turns out to be -0.008 g/cm$^3$, which is a very small negative effect in the resulting density. In the laser power and the hatching

**Table 4.5: Effect of Main Process Parameters and Their Interactions on Apparent Mass Density**

| | **(g/cm3)** |
|---|---|
| A | 0.082 |
| B | -0.079 |
| C | -0.145 |
| AB | -0.008 |
| AC | 0.037 |
| BC | -0.035 |
| ABC | -0.038 |

*** Process Parameters: A: Laser Power, B: Laser Scan Speed, C: Hatching Distance**

distance interaction, AC, the effect of the laser power is greater when compared to AB interaction. The increase of the hatching distance from low (0.30 mm) to high level (0.45 mm) results in -0.145 g/cm$^3$ (main effect of the hatching distance) decrease in the density. However from the laser power and hatching distance interaction, AC, it is seen that, the negative effect of hatching distance in density is totally compensated by the positive effect of laser speed and the resulting effect of AC turns out to be a positive effect in resulting density, 0.037 g/cm$^3$, which is significant.

As the laser scan speed (B) and hatching distance (C) have a negative effect on the density, naturally their interaction effect, (BC) does also have a negative effect, -0.037 g/cm$^3$ in the density. Although the laser power's positive effect in resulting density is seen in its interactions with the laser speed and hatching distance, AB and AC, the positive effect of laser power is not seen in the triple interaction of parameters, ABC, the effect of which is -0.038 g/cm$^3$, a negative effect in the resulting density.

After the quantitative analysis of the effects, it is seen that, except the interaction between laser power and laser scan speed (AB), all other effects: the main effects of laser scan speed (A), laser speed (B) and hatching distance (C) and the interaction effects of laser power-hatching distance (AC), laser scan speed- hatching distance (BC) and laser power-laser scan speed-hatching distance

(ABC) seem to be important and should be considered during the establishing the mathematical model. To calculate the importance of each effect statistically, as it will be shown in the next section, a statistical analysis of the experimental data was undertaken. In fact, the main intention of the statistical analysis was to calculate the experimental error of the measurements.

### 4.5 The Statistical Analysis of the Density Variation Experiment

The statistical analysis of the experiments is performed to calculate the variation in the all measured values of the response of the experiment, which occurs because of different levels of the process parameters. After the statistical analysis, the effect of each process parameter on the response variation is compared and relative effectiveness of the process parameters on the mass density, as well as the magnitude of the experimental error are, are established.

In the current study, the process parameters are the laser power (A), the laser scan speed (B) and the hatching distance (C) and the response is the apparent mass density of the laser sintered parts. However, as the interactions between these input parameters also result in variations in the mass density, the interactions are also considered as influential parameters of the experiment. Thus in the statistical analysis, the variations in mass density due to different levels of the main effects and interaction effects will be calculated and each variation will be compared.

From the results of the $2^3$ Factorial Design experiment, in Table 4.2, the total mean of the all measured apparent mass densities of test part is

$$\overline{\rho} = \frac{(0.955 + 0.950 + 0.965 + 9.971 + ........ + 0.775)}{16} = 0.866 g / cm^3 \qquad (4.22)$$

That is if there were no experimental errors and the process parameters and their interactions had no effect on mass density, this would be the hypothetical constant density of all 16 parts (2 replicates each for 8 process configurations)

To calculate the total variation of the measured densities, the total corrected **sum of squares** formula is used [30].

$$SS_T = \sum_{i=1}^{N} \rho_i^2 - \frac{\overline{\rho}^2}{N} \tag{4.23}$$

where "$N$" is number of total measurements (observations) . In this experiment "$N$" equals to 16, thus the resultant measure of total variation in density variation experiment is

$$SS_T = \sum_{i=1}^{16} \rho_i^2 - \frac{\overline{\rho}^2}{16} = 0.1525 g / cm^3 \tag{4.24}$$

This total variation denotes the variation in density (deviation from total mean) due to different levels of the main and interaction effects and as well as due to experimental error during the measurements [30]. The total variation can be broken down to:

$$SS_T = SS_A + SS_B + SS_C + SS_{AB} + SS_{AC} + SS_{BC} + SS_{ABC} + SS_E \tag{4.25}$$

Where $SS_E$ denotes the variation from the mean due to the experimental error and the others denote the variations due to the effect of each factor and factor interactions.

The sum of squares for all the main effects and interaction effects in equation (4.25) can be found from, [30]

$$SS_i = \frac{[Contrast_i]^2}{8n} \tag{4.26}$$

where the **contrast** (Section 4.3) of the main effects and the interaction effects were calculated in Section 4.4 and "$n$" stands for number of replicates. Then,

$$SS_A = \frac{(0.656)^2}{16} = 0.0269 \cdot g / cm^3 \tag{4.27}$$

$$SS_B = \frac{(-0.634)^2}{16} = 0.0252 \cdot g / cm^3 \tag{4.28}$$

$$SS_C = \frac{(-1.157)^2}{16} = 0.0837 \cdot g / cm^3 \tag{4.29}$$

$$SS_{AB} = \frac{(-0.065)^2}{16} = 0.0003 \cdot g/cm^3 \tag{4.30}$$

$$SS_{AC} = \frac{(0.296)^2}{16} = 0.0055 \cdot g/cm^3 \tag{4.31}$$

$$SS_{BC} = \frac{(-0.281)^2}{16} = 0.0050 \cdot g/cm^3 \tag{4.32}$$

$$SS_{ABC} = \frac{(-0.305)^2}{16} = 0.0058 \cdot g/cm^3 \tag{4.33}$$

The experimental error sum of squares can be found by substituting equations (4.27-4.33) into equation (4.25)

$$\begin{aligned} SS_E &= SS_T - SS_A - SS_B - SS_C - SS_{AB} - SS_{AC} - SS_{BC} - SS_{ABC} \\ &= 0.1525 - 0.0269 - 0.0252 - 0.0837 \\ &\quad - 0.0003 - 0.0055 - 0.0050 - 0.0058 \\ &= 0.0002 \end{aligned} \tag{4.34}$$

The above results and the calculated effects are presented in Table 4.6. As seen from the results, the variation due the experimental error accounts for 0.1% of total variation, which shows that the experimental error in the experiment is very small (the mass density values do not vary significantly because of experimental error). As expected, sum of squares is another indicator for the effect of factors (process parameters) and their interactions on part mass density. In addition the sum of squares also quantifies the effect of experimental error on the measured response.

From the statistical analysis, it is seen that the main effects are highly significant. Although not as high as the main effects, the interactions AC, BC and ABC also have substantial effect on the density. Thus all the main effects and AC, BC, and ABC interactions are to be considered in the regression analysis of the experiment Among all parameters, only the AB interaction seems to have little effect on the resulting apparent mass density. However, in the regression analysis, the AB interaction will be considered also, as the experiment has been already employed and the inclusion of AB interaction does not lead to any complexity in the calculations. However if the result of the mathematical model established by

**Table 4.6: The Sum of Squares and Calculated Effects of the Parameters of the Density Experiment**

| Parameter | Calculated Effect ($g/cm^3$) | Sum of Squares, SS (Variation in Density, $g/cm^3$) | Percent Contribution to Total Variation $(SS_i / SS_T)$ |
|---|---|---|---|
| A | 0.082 | 0.0269 | 17.64 |
| B | -0.079 | 0.0252 | 16.52 |
| C | -0.145 | 0.0837 | 54.88 |
| AB | -0.008 | 0.0003 | 0.27 |
| AC | 0.037 | 0.0055 | 3.6 |
| BC | -0.035 | 0.0050 | 3.27 |
| ABC | -0.038 | 0.0058 | 3.81 |
| Experimental Error | | 0.0002 | 0.1 |
| Total | | 0.1525 | |

the regression analysis of the designed $2^3$ experiment does not give accurate results, a more advanced design of experiment approach must be employed (such as $3^k$). In that case, the AB interaction could be neglected for reducing the increased number of the runs.

## 4.6 Development of a Mathematical Model for Relating Process Parameters to Part Mass Density

If there is a single **response** *y* that depends on *k* **independent** variables**,** for example, $x_1$, $x_2$...... $x_n$, then the relationship between these variables can be characterized by a mathematical model called a **regression model.** The regression model is a fit to a set of experimental data. After building the model relating the response to independent variables, the experimenter can predict the response for different combinations of the independent variables and ultimately the process optimization and the process control can be achieved. In this study, the aim is to develop a prediction tool for determining parts density (as a measure of their porosity) from the three process parameter settings, laser power, laser scan speed and hatching distance.

### 4.6.1 Linear Regression Model

A linear model describing the relationship between the response of a process to two independent variables of the process is

$$y = \beta_0 + \beta_1 x_1 + \beta_2 x_2 + \varepsilon \tag{4.35}$$

where y represents the response, $x_1$ and $x_2$ represent the two independent variables and $\varepsilon$ is the error, defined as the difference between the experimentally measured response and the predicted response value by the mathematical model. The term linear is used because equation (4.35) is linear function of the unknown parameters $\beta_0$, $\beta_1$ and $\beta_2$. The model describes a plane in the three dimensional ($x_1$, $x_2$, $y$) space. The parameters, $\beta_1$ and $\beta_2$ are called the *partial variable coefficients*, because $\beta_1$ measures the expected change in $y$ per unit change in $x_1$ when $x_2$ is held constant, and $\beta_2$ measures the expected change in $y$ per unit change in $x_2$ when $x_1$ is held constant [30].

The above discussion can be extended to $k$ independent variables as:

$$y = \beta_0 + \beta_1 x_1 + \beta_2 x_2 + \dots\dots\dots + \beta_k x_k + \varepsilon \tag{4.36}$$

which is called a ***multiple linear regression model with k variable coefficients***. The parameter $\beta_j$ represents the expected change in response $y$ per unit change in $x_j$ when all the remaining independent variables $x_i$ $(i \neq j)$ are held constant.

Models that are more complex in appearance than the Equation (4.36) may often be analyzed by multiple linear regression techniques. For example, if an interaction term is added to the first order model in two variables, as

$$y = \beta_0 + \beta_1 x_1 + \beta_2 x_2 + \beta_{12} x_1 x_2 + \varepsilon \tag{4.37}$$

The model can still be linear by defining $x_3 = x_1 x_2$ and $\beta_3 = \beta_{12}$ as

$$y = \beta_0 + \beta_1 x_1 + \beta_2 x_2 + \beta_3 x_3 + \varepsilon \tag{4.38}$$

### 4.6.2 Regression Model of the Density Experiment

As all the main effects, A, B, C and the interaction effects AB, AC, BC and ABC are included in the regression model, then the linear model that describing the relationship would be

$$\begin{aligned}\rho = \beta_0 + \beta_1 x_1 + \beta_2 x_2 + \beta_3 x_3 + \beta_{12} x_1 x_2 \\ + \beta_{13} x_1 x_3 + \beta_{23} x_2 x_3 + \beta_{123} x_1 x_2 x_3 + \varepsilon\end{aligned} \tag{4.39}$$

where $\rho$ represents the apparent mass density (the response), $x_1$ represents the laser power (A), $x_2$ represents the laser speed (B), $x_3$ represents the hatching distance (C), $x_1 x_2$ represents the AB interaction, $x_1 x_3$ represents the AC interaction, $x_2 x_3$ represents the BC interaction and $x_1 x_2 x_3$ represents the ABC interaction. $\beta_0$, $\beta_1$, $\beta_2$, $\beta_3$, $\beta_{12}$, $\beta_{13}$, $\beta_{23}$, $\beta_{123}$ are the regression coefficients.

When the interaction effects are substituted such as, $x_4 = x_1 x_2$, $\beta_4 = \beta_{12}$, $x_5 = x_1 x_3$, $\beta_5 = \beta_{13}$, $x_6 = x_2 x_3$, $\beta_6 = \beta_{23}$ , $x_7 = x_1 x_2 x_3$ and $\beta_7 = \beta_{123}$ the Equation (4.39) can be written as

$$\rho = \beta_0 + \beta_1 x_1 + \beta_2 x_2 + \beta_3 x_3 + \beta_4 x_4 + \beta_5 x_5 + \beta_6 x_7 + \beta_7 x_7 + \varepsilon \tag{4.40}$$

The experimental data on the density study, which was shown in Table 4.2, is again presented in Table 4.7 below, but this time, instead of the -1,+1 level symbols, the exact values of each parameter are shown in Table 4.7.

The model equation, Equation (4.40), in terms of the measurements in Table 4.7 can be written as

$$\begin{aligned}\rho_i &= \beta_0 + \beta_1 x_{i1} + \beta_2 x_{i2} + \dots\dots\dots + \beta_k x_{ik} + \varepsilon_i \\ &= \beta_0 + \sum_{j=1}^{k} \beta_j x_{ij} + \varepsilon_i\end{aligned} \tag{4.41}$$

where $\rho_i$ is the measured density at the ith measurement, $x_{ij}$ is the ith value of the variable $x_j$, and $\varepsilon_i$ is the ith measurement error. For calculating the regression coefficients, $\beta$'s, in Equation 4.41, least squares method is employed, minimizing the error $\varepsilon_i$ . The details of the method are presented in Appendix C.

**Table 4.7: The Results of $2^3$ Factorial Design Density Variation Experiment**

| Process Config. | Test Run | Parameter* Levels | | | Measured Apparent Mass Density ($g/cm^3$) | | | |
|---|---|---|---|---|---|---|---|---|
| | | Laser Power (A, W) | Laser Scan Speed (B, mm/s) | Hatching Distance (C, mm) | Replicate 1 | Replicate 2 | Density Sum ($g/cm^3$) | Density Avg. ($g/cm^3$) |
| -1 | 1 | 28.15 | 4000 | 0.3 | 0.955 | 0.950 | 1.905 | 0.953 |
| A | 2 | 38.22 | 4000 | 0.3 | 0.965 | 0.971 | 1.936 | 0.968 |
| b | 3 | 28.15 | 5000 | 0.3 | 0.875 | 0.883 | 1.758 | 0.879 |
| ab | 4 | 38.22 | 5000 | 0.3 | 0.951 | 0.957 | 1.908 | 0.954 |
| c | 5 | 28.15 | 4000 | 0.45 | 0.764 | 0.773 | 1.537 | 0.769 |
| ac | 6 | 38.22 | 4000 | 0.45 | 0.933 | 0.934 | 1.867 | 0.934 |
| bc | 7 | 28.15 | 5000 | 0.45 | 0.696 | 0.704 | 1.400 | 0.700 |
| abc | 8 | 38.22 | 5000 | 0.45 | 0.771 | 0.775 | 1.546 | 0.773 |

*** Process Parameters: A: Laser Power, B: Laser Scanning Speed, C: Hatching Distance**

After applying the least square method to the experimental data obtained from the $2^3$ factorial design experiments, shown in Table 4.8, the mathematical regression model between the part apparent mass density and three process parameters, the laser power, laser scan speed and the laser speed is found as,

$$\begin{aligned}\rho = 5.377 - 0.144x_1 - 8.522\times10^{-4}x_3 - 12.479x_3 + 3.012\times10^{-5}x_1x_2 \\ + 0.428x_1x_3 + 2.248\times10^{-3}x_2x_3 - 8.591\times10^{-5}x_1x_2x_3\end{aligned} \tag{4.42}$$

where $x_1$ stands for the laser power, $x_2$ for the laser scan speed, $x_3$ for the hatching distance. The details of the calculations are presented in Appendix C.

In section 6.1, the validity of this established model will be checked.

# CHAPTER 5

# HOLE STRUCTURES
# (REGULAR POROUS STRUCTURES)

## 5.1 Producing Hole Structures with EOSINT P380

The feasibility of utilizing an RP technique for fabricating parts with small holes on them depends mainly on the size of the smallest feature and the accuracy with which that smallest feature can be built with that particular RP technique. Such a capability is usually constrained by the working principles of the RP process, as well as the process parameters and properties of the building materials. Within this concept, this study concentrates on determining the smallest hole size and the corresponding accuracy, for obtaining ordered regular hole features on laser sinter parts with PA 2200 powder. A number of test parts that have small hole features on them are designed and built for the analysis.

The test parts for the small hole structures are designed by considering two factors:

a) Laser exposure strategy of the SLS system

b) Shrinkage of the parts after sintering.

The details of the design steps based on these two factors are given in the following.

### 5.1.1. Laser exposure strategy of the SLS system

A typical ordered regular porous architecture, similar to the test parts that are built in this part of the research, is shown in Figure 5.1. In building such parts, the type of the scan performed (contouring only, contouring and hatching

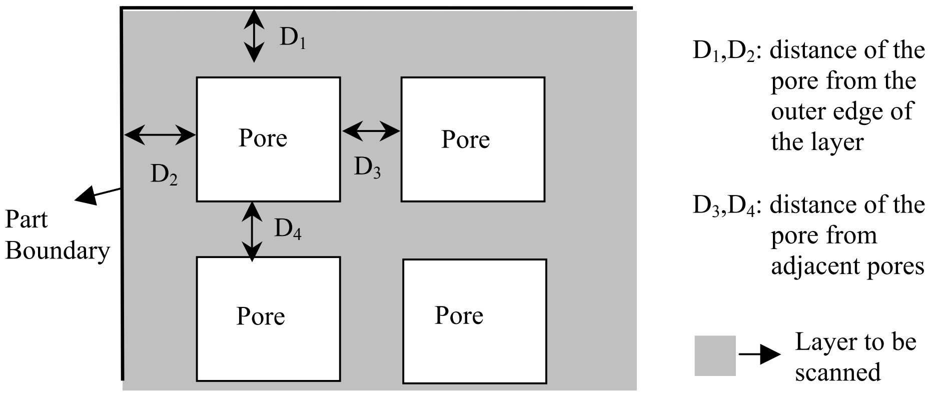


**Figure 5.1: A typical pore architecture**

together, or “EDGES”) depends on the distances between the pores and the closest boundaries surrounding it ($D_1$, $D_2$ , $D_3$, $D_4$ in Figure 5.1).

As the accuracy, with which pore features can be built, are directly dependant on the type of scan of their surrounding medium, in the test parts these dimensions ($D_1$, $D_2$ , $D_3$, $D_4$ at Figure 2.7) are varied.

In building the test parts the default values of the machine parameters, as specified by the manufacturer, are used. In this case, the power level and the laser scanning speed were set to 10.8 W and 700 mm/s respectively, during contouring, resulting in an effective diameter of 0.680 mm ($D_{ec}$). The beam offset for contouring is selected as 0.340 mm (half the effective diameter) and the beam offset for hatching is set to 0.530 mm (in order to guarantee that no unsintered region exists between the contour and hatching paths).

When a sliced model is imported into the process software of EOSINT P380, PSW$^{TM}$, the type of scan (contouring only, contouring and hatching together, or “EDGES”) that will be performed on the sections of the sliced data can be seen, prior to build. For example in Figure 5.2, a sample section of a layer, as imported into the system software PSW$^{TM}$, is shown. In this part, there are ordered tubular hole features with square sections. Depending on the wall thickness, contour, edges and hatching modes are specified at various portions of the section.

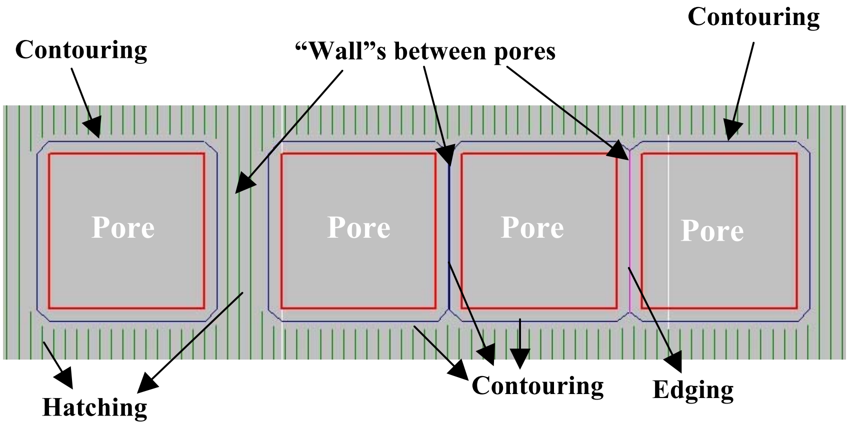


**Figure 5.2: Laser scan types on a layer section of a hole structure**

As such, before building test parts, all laser scan types are verified within the system software. This way the wall thickness (between the holes) ranges, which would correspond to different scan types, were determined, prior to actual building. This was a valuable tool in determining the geometric specifications of the pore features in the regular pore test parts. For the specified contour beam offset (0.34 mm), only a single contour scan was observed ("EDGES function") at the exactly mid point between two adjacent pores (Figure 5.3), where the wall thickness was less than 0.68 mm.

For the case: 0.68 mm ≤ wall thickness < 1.2 mm, two contouring laser paths were observed in the wall sections, without any hatching. In Figure 5.4(a),

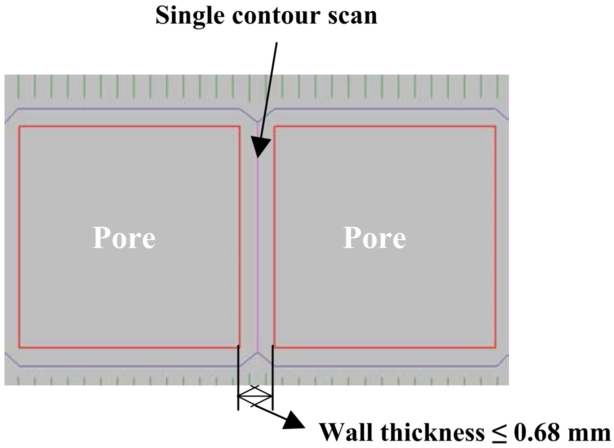


**Figure 5.3: Close up of "EDGES" in the boundaries between adjacent pores for thin wall sections, wall thickness ≤ 0.68 mm (contour beam offset =0.34 mm)**

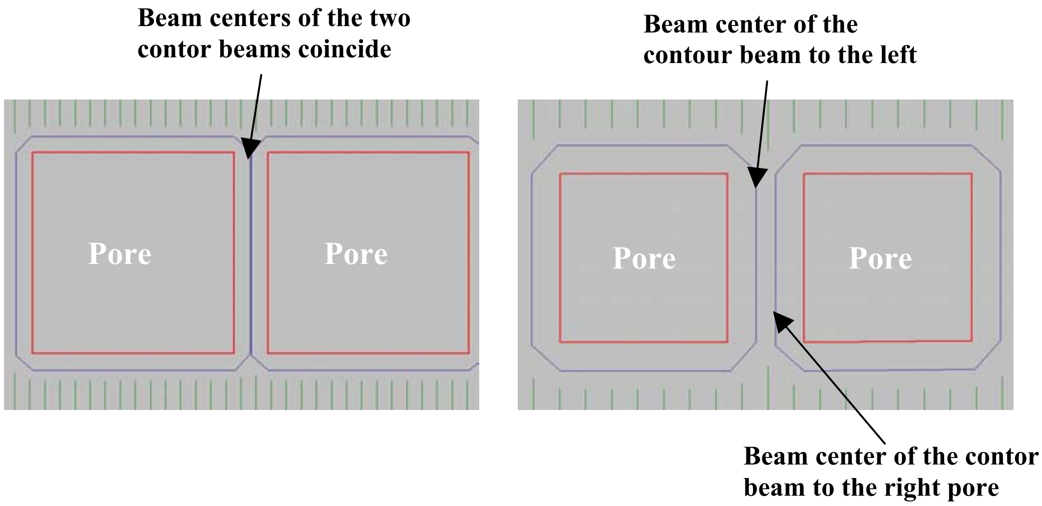


(a) Wall thickness= 0.68 mm (b) Wall thickness= 0.9 mm

**Figure 5.4: Laser scanning of wall sections where 0.68 mm ≤ wall thickness < 1.2 mm**

the wall thickness between the pores was modeled as 0.68 mm, which exactly equals to “2 x beam offset ($d_c$)”.In Figure 5.4(b), the wall thickness was modeled as 0.9 mm. In the Figure 5.4(a), the two contour paths in the wall sections completely overlap, the beam centers coinciding at the center. In Figure 5.4(b), the wall thickness is 0.9 mm, larger than “2 x beam offset ($d_c$)”, therefore the two contour beam centers do not coincide. In addition, the wall thickness is not large enough for hatching.

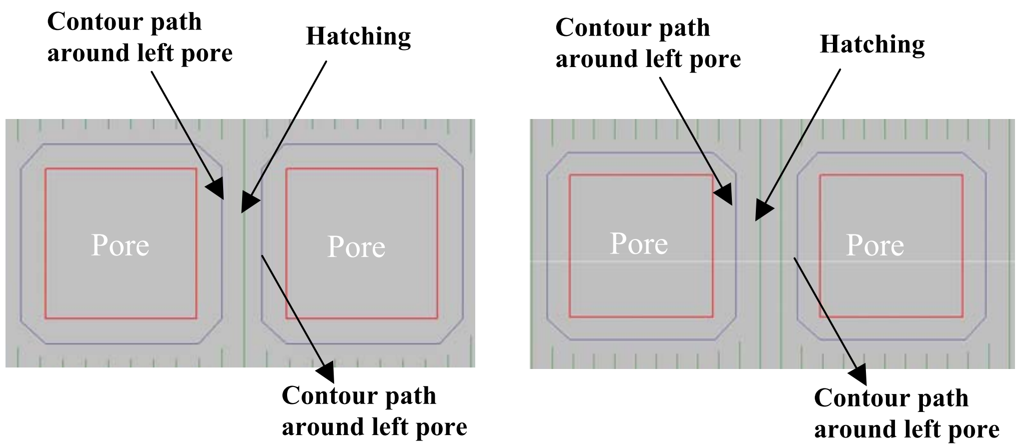


(a) Wall thickness= 1.2 mm (b) Wall thickness> 1.2 mm

**Figure 5.5: Laser scanning of wall sections where where wall thickness ≥ 1.2 mm**

**Table 5.1: The ranges of the scan types in EOSINT P380**

| Type of Scan | Wall Thickness Range |
|---|---|
| Edging (EDGES function) | WT< 0.68 mm |
| Contouring Only | 0.68 mm ≤ WT <1.2 mm |
| Contouring and Hatching | WT≥1.2 mm |

***WT stands for wall thickness**

For the wall thickness values starting from 1.2 mm, in addition to the two contour paths, hatching was also observed in the wall sections between the pores (Figure 5.5). When the wall thickness is equal to 1.2 mm, only a single hatching laser path is observed in the wall section (Figure 5.5(a)). When the wall thickness increases, the number of the hatching laser paths also increases, as seen in Figure 5.5(b).

Based on the above analysis, test parts were built with varying wall thicknesses, related to the type of scans. The ranges for the scan types are specified in Table 5.1

### 5.1.2. Part shrinkage

The shrinkage factor is a process parameter that can be input to the system like the previous parameters. Its function is to compensate for the shrinkage that occurs in the polymer when it is cooling after sintering, so that the design dimensions can be obtained after production.

For all parts in the standard applications with PA powder, after the part model is oriented to its production orientation, the model is scaled with a 1.032 shrinkage factor in the X and Y axes directions; that is the shrinkage factor on the layer plane is isotropic. The design dimensions on the layer plane are multiplied by 1.032 during the actual production. Along the Z axis direction (layer by layer direction), the shrinkage factor can be adjusted from 1.013 to 1.018, depending on the maximum dimension of the part in that direction. These shrinkage factor values are the default values as specified by the manufacturer. The slice data of the scaled model is imported into the process software. The software generates the tool laser paths with respect to the dimensions of the scaled model, not the original unscaled model (corresponding to design dimensions).

The shrinkage factor directly affects the dimensional accuracy of the sintered parts. During the design of the regular pore the shrinkage factor is also a varied parameter, along with pore size and wall thickness.

## 5.2 Test Parts for Small Hole Structures

In order to study the accuracy with which small hole structures can be built in SLS, as well as the limiting size of hole features, various test parts have been designed and built with different hole architecture and process parameters.

### 5.2.1 Test Part 1

In test part 1, the aim was to study the accuracy in building holes of the same size, with varying wall thicknesses and varying shrinkage factors. In this part, there are four major groups of holes, each of which is subdivided into three minor pore groups, totally twelve different groups of holes. All holes in this part

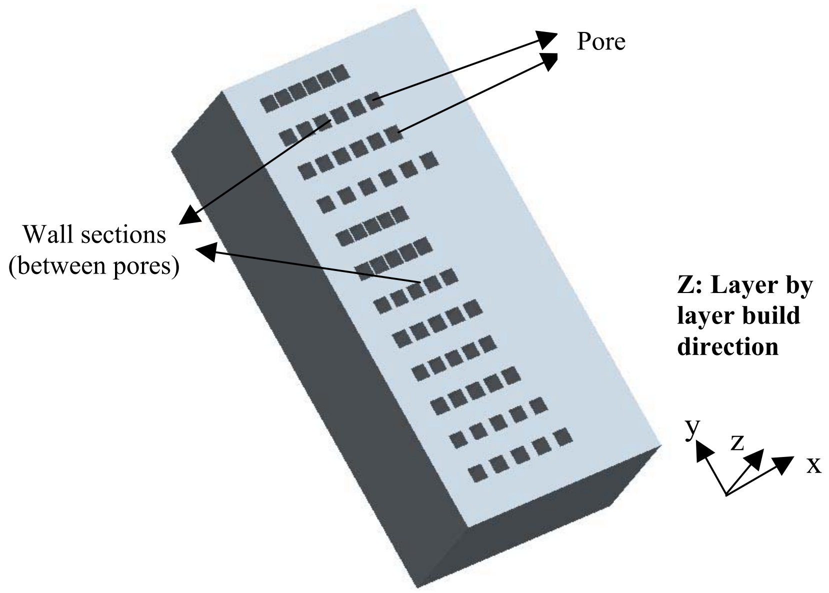


**Figure 5.6: The model of Test Part 1**

are square cross-section with a design side length of 2 mm. Each group of holes is composed of 5 or 6 holes with same wall thicknesses (Figure 5.6). The characteristics of this part are shown in Table 5.2.

The shrinkage factor in Z direction is considered to have little effect on the accuracy of the holes (the pore cross sections lie on the XY plane). Thus during the analysis, the Z direction shrinkage factor was not considered.

The measurements of the hole features on Test Part 1 were performed by Global Status$^{TM}$ CMM machine in METU BİLTİR CAD/CAM and Robotics Center. The hole size and wall thickness measurements are done, first by touching the inner walls of the holes and then calculating the distances between these touched points (P1, P2…P8, in Figure 5.7). For each hole group, three hole sizes and four wall thicknesses measurements are done, as shown in Figure 5.7. The results and discussions of Test Part 1 are given in Section 6.2.1.

**Table 5.2: Test Part 1 Characteristics**

| Designation of major group of holes | Minor Group Designations | Shrinkage Factor on layer plane | Scaled HS* (mm) | Scaled WT* (mm) | Type of the scan on the wall sections |
|---|---|---|---|---|---|
| Group 1<br>Nominal WT: 0.2 mm | 1.A | 1 | 2 | 0.2 | EDGES |
| | 1.B | 0.968 | 1.937 | 0.1937 | EDGES |
| | 1.C | 1,032 | 2.064 | 0.2064 | EDGES |
| Group 2<br>Nominal WT: 0.66 mm | 2.A | 1 | 2 | 0.66 | EDGES |
| | 2.B | 0.968 | 1.937 | 0.639 | EDGES |
| | 2.C | 1,032 | 2.064 | 0.6811 | Contouring Only |
| Group 3<br>Nominal WT: 0.68 mm | 3.A | 1 | 2 | 0.68 | Contouring Only |
| | 3.B | 0.968 | 1.937 | 0.658 | EDGES |
| | 3.C | 1,032 | 2.064 | 0.701 | Contouring Only |
| Group 4<br>Nominal WT: 1.2 mm | 4.A | 1 | 2 | 1.2 | Contouring + Hatching |
| | 4.B | 0.968 | 1.937 | 1.162 | Contouring Only |
| | 4.C | 1.032 | 2.064 | 12.384 | Contouring + Hatching |

**HS: Hole Size, WT: Wall thickness**
**Nominal hole size (side length of hole) in all holes= 2 mm**
**Contour beam offset= 0.34 mm**
*** Including the effect of shrinkage factor**

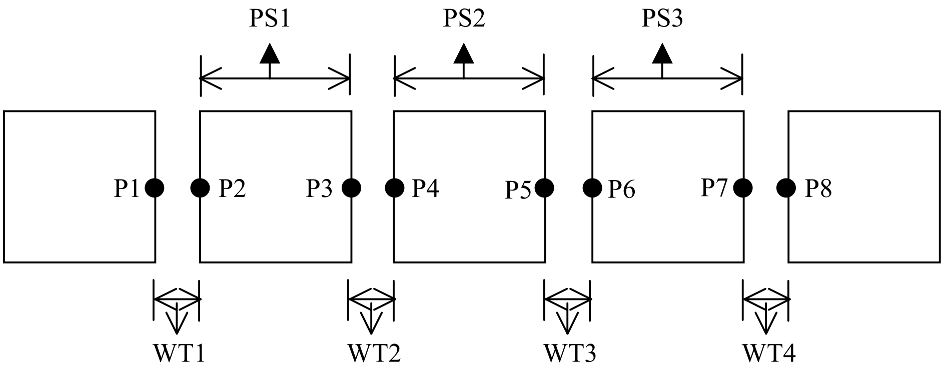


**Figure 5.7: The CMM measurement of the hole sizes and wall thicknesses on Test Parts 1 and 2**

### 5.2.2 Test Part 2

As it will be discussed in Section 6.2, in Test Part 1, both shrinkage factor and type of the scan have been shown to have considerable effect on the dimensional accuracy. However, it should be pointed out that, on the Test Part 1, except the 1st major hole group, in all other major hole groups, the scan types of the wall sections of the minor hole groups were different. As a result, the effect of shrinkage factor could not be isolated, separate from the effect of scan type. Test Part 2 (Figure 5.8) was designed to isolate the effect of the shrinkage factor on the accuracy of the hole features.

In the Test Part 2, there are 2 major groups of hole, each of which is

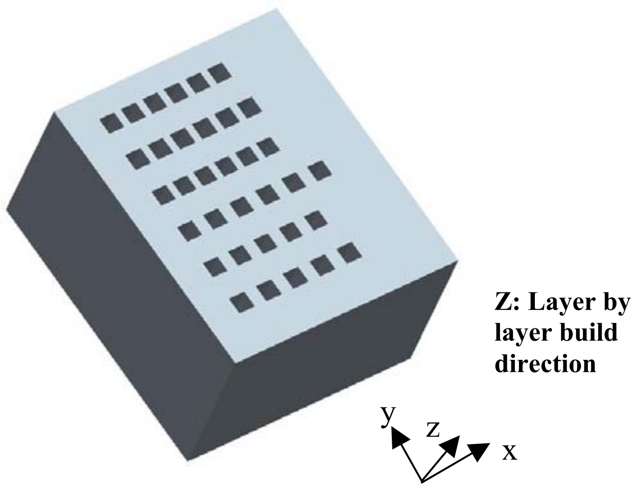


**Figure 5.8: The model of Test Part 2**

subdivided into 3 minor groups, totaling 6 different groups of holes. The design (nominal) wall thickness for the first group was 0.9 mm and for the second group, 1.4 mm. The scan types for all the wall sections are same. The characteristics of Test Part 2 can be seen in Table 5.3. The CMM measurement of Test Part 2 is performed in the same manner as it is in Test Part 1, and again for each hole group, three hole sizes and four wall thicknesses measurements are done. The results and discussions of Test Part 2 are given in Section 5.1.2.

### 5.2.3 Test Part 3

In Test Part 3, the goal was to study the accuracy in building holes with varying sizes, as well as with varying wall thicknesses in between holes. For Test Part 3, the shrinkage factor was kept at the recommended 1.032 value.

In Test Part 3, there are 7 groups of holes and each group has 9 holes, with different hole sizes and wall thicknesses in between (Figure 5.9). Each hole is again tubular with a square cross- section. In the upper row, there are two groups of holes. Each group has the hole cross-sectional dimensions of 3 mm x 3 mm. In the upper left group, the wall thickness between the holes is 0.68 mm. In upper right group, the wall thickness is 1.4 mm. In the middle row, there are 2 groups of

**Table 5.3: Test Part 2 Characteristics**

| Designation of Major group of holes | Minor Hole Group Designation | Shrinkage Factor | Scaled HS* (mm) | Scaled WT* (mm) | Type of the scan on the wall sections |
|---|---|---|---|---|---|
| Group 1 WT: 0.9 mm | 1.A | 1 | 2 | 0.900 | Contouring Only |
| | 1.B | 0.968 | 1.937 | 0.871 | Contouring Only |
| | 1.C | 1.032 | 2.064 | 0.929 | Contouring Only |
| Group 2 WT: 1.4 mm | 2.A | 1 | 2 | 1.4 | Contouring + Hatching |
| | 2.B | 0.968 | 1.937 | 1.357 | Contouring + Hatching |
| | 2.C | 1.032 | 2.064 | 1.445 | Contouring + Hatching |

**HS: Hole Size, WT: Wall thickness**
**Nominal hole size (side length of hole) in all holes= 2 mm**
**Contour beam offset= 0.34 mm**
*** Including the effect of shrinkage factor**

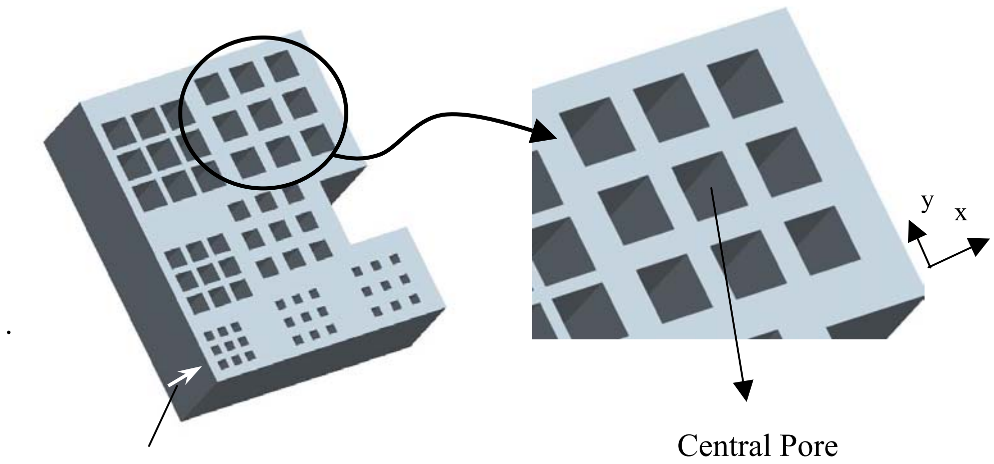


**Figure 5.9: The model of Test Part 3**

holes with each hole having the cross – sectional dimensions of 2 mm x 2 mm. The middle left group has a wall thickness of 0.68 mm and the middle right group has a wall thickness of 1.1 mm. In the lower row, all holes are tubular with the cross-sectional dimensions of 1 mm x 1 mm. The lower left, the lower middle and the lower right groups have the wall thicknesses of 0.68, 1.1 and 1.4 mm, respectively.

In the CMM measurements of the Test Part 3, the hole size of the central holes in X and Y direction (Figure 5.9) and the thicknesses of all the walls surrounding these central holes (upper, lower, left and right walls) are measured. For that, first the probe of the CMM was touched on the inner walls of the central holes and neighbor holes and then the distances between these touched points (P1, P2…P8, in Figure 5.10) were calculated. The results and discussions of Test Part 2 are given in Section 6.2.3.

### 5.2.4 Lattice Structures

The final regular hole test parts that were produced in this study are lattice structures (See Figure 2.17). These parts differ from the previous test parts by their different hole architecture (lattice rather than tubular architecture). Three

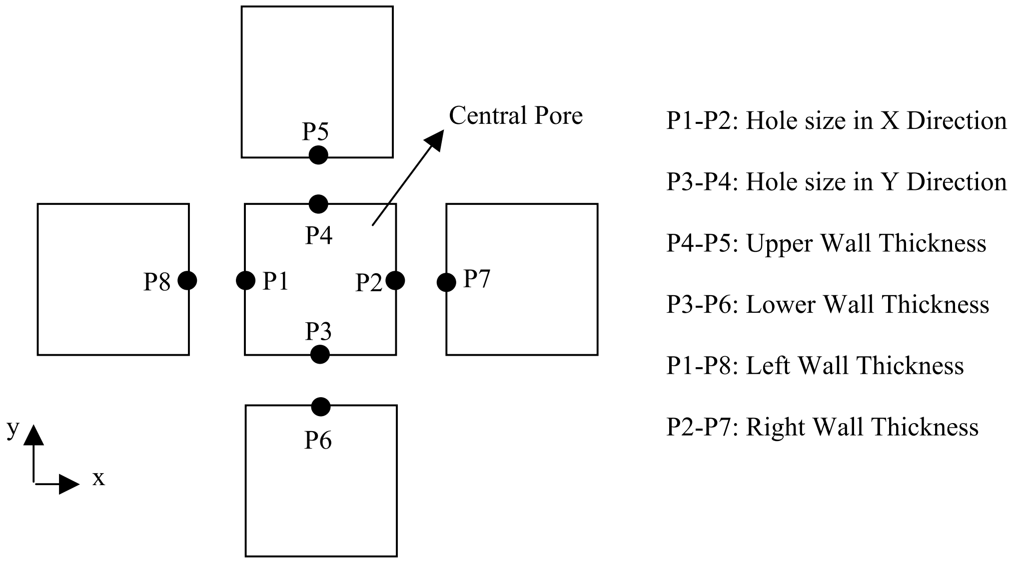


**Figure 5.10: The CMM measurement points for hole sizes and wall thicknesses on Test Part 3**

cubic lattice structures were modeled with cubic hole cross-sectional dimensions of 2 mm x 2 mm x 2 mm (PS, in Figure 5.11) but with different wall thicknesses (WT). The first lattice structure was modeled with 0.65 mm wall thickness, the second lattices structure was modeled with 1.1 mm and the third was with 1.4 mm. On each surface of the modeled lattice structures, the wall section to the layer edge was modeled with 2 mm thickness (Figure 5.11). As the hole features are three dimensional, in contrast to other test parts, the lattice structures were scaled in three directions, with the recommended 1.032 value in the X and Y axis and 1.013 value in the Z axis.

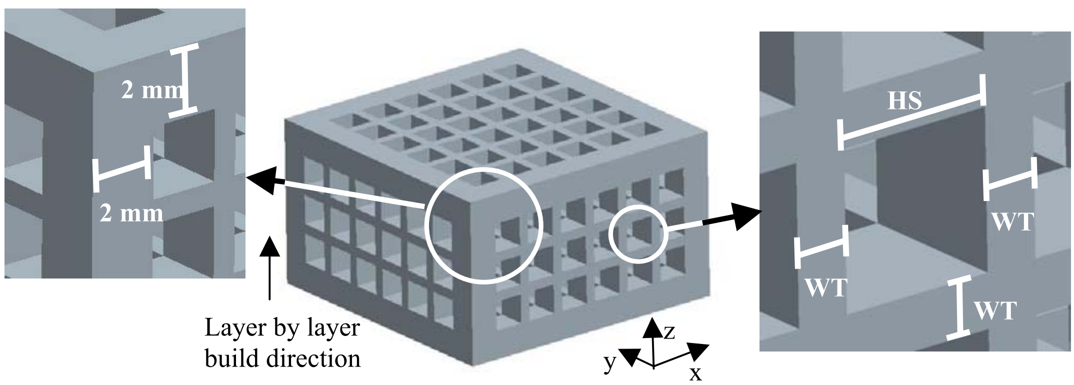


**Figure 5.11: Lattice Structures, HS and WT stands for the hole size and wall thickness, respectively.**

With lattice structures, during CMM measurements, in addition to the deviations in the hole size and wall thickness, the side lengths on the XY plane (w, in Figure 5.12(a)), were measured also. With this it is intended to examine the effect of the deviations in the hole size and wall size between the holes on the accuracy of the whole part. As the holes are distributed in 3D, for each lattice structure, three measurements are done on three different rows of holes, which lie on different planes, on XY, XZ and YZ plane (Figure 5.12(a)). In each measurement, the probe of the CMM was touched on the inner walls of holes of the measured row (P2,P3…P13) and on the surface of the part (P1 and P14), as shown in Figure 5.12(b).

As the wall thickness between the holes differs between the lattice structures, the designed side length (w, in Figure 5.12(a)) is different for each

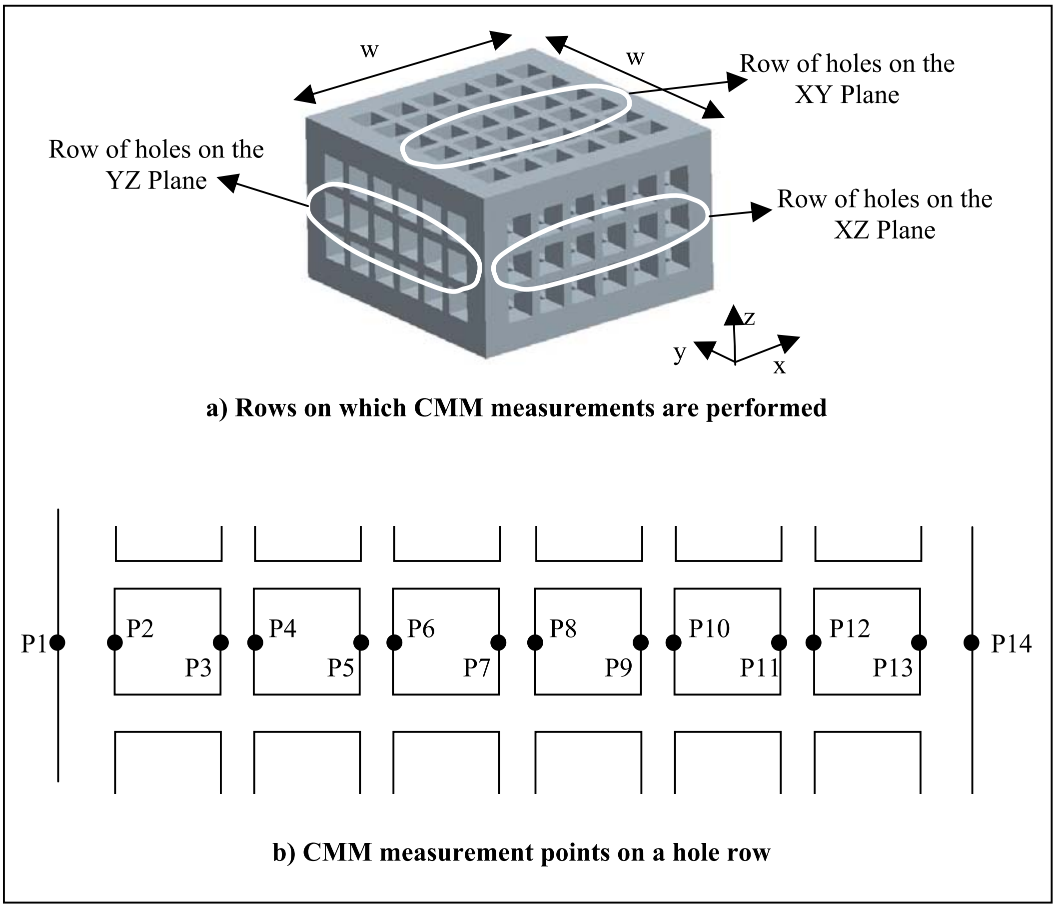


**Figure 5.12: The CMM measurement of the hole features on lattice structure**

lattice. For the lattice with 0.65 mm wall thickness between the holes, the side length is 19.25 mm, for the lattice with 1.1 mm wall thickness it is 21.5 mm and 23 mm for the lattice with 1.4 mm wall thickness. The results and discussions of lattice structures are given in Section 6.2.4.

# CHAPTER 6

# RESULTS AND DISCUSSIONS

## 6.1 Porosity of the Laser Sintered Parts (Irregular Porous Structures)

### 6.1.1 The Validity of the Established Model

As mentioned in Chapter 4, based on the experimental data obtained from a $2^3$ factorial design experiment, a mathematical relation between the irregular porous part apparent mass density and the three process parameters, the laser power, the laser scan speed and the laser speed was found as ,

$$\begin{aligned}\delta = 5.377 - 0.144x_1 - 8.522\times10^{-4}x_3 - 12.479x_3 + 3.012\times10^{-5}x_1x_2 \\ + 0.428x_1x_3 + 2.248\times10^{-3}x_2x_3 - 8.591\times10^{-5}x_1x_2x_3\end{aligned} \quad (6.1)$$

where $x_1$ is laser power in W, $x_2$ is laser scan speed in mm/s and $x_3$ is hatching distance in mm.

The results of the designed experiment are shown once again here, in Table 6.1. In the first test to check the validity of the obtained mathematical model, the density values measured in the experiment is compared with the predicted density values obtained from the model. For this, the parameter values of each run in the experiment were inputted into Equation (6.1) to calculate the predicted density with that parameter combination. For example, in the first run, the parameters were adjusted as: 28.15 W laser power, 4000 mm/s laser speed and 0.3 mm hatching distance. Substituting these values into Equation (6.1),

**Table 6.1: The Results of $2^3$ Factorial Design Density Variation Experiment**

| | | Parameter* Levels | | | Measured Apparent Mass Density (g/cm$^3$) | | | |
|---|---|---|---|---|---|---|---|---|
| Process Config. | Test Run | Laser Power (A, W) | Laser Scan Speed (B, mm/s) | Hatching Distance (C, mm) | Replicate 1 | Replicate 2 | Density Sum (g/cm$^3$) | Density Avg. (g/cm$^3$) |
| -1 | 1 | 28.15 | 4000 | 0.3 | 0.955 | 0.950 | 1.905 | 0.953 |
| A | 2 | 38.22 | 4000 | 0.3 | 0.965 | 0.971 | 1.936 | 0.968 |
| B | 3 | 28.15 | 5000 | 0.3 | 0.875 | 0.883 | 1.758 | 0.879 |
| Ab | 4 | 38.22 | 5000 | 0.3 | 0.951 | 0.957 | 1.908 | 0.954 |
| C | 5 | 28.15 | 4000 | 0.45 | 0.764 | 0.773 | 1.537 | 0.769 |
| Ac | 6 | 38.22 | 4000 | 0.45 | 0.933 | 0.934 | 1.867 | 0.934 |
| Bc | 7 | 28.15 | 5000 | 0.45 | 0.696 | 0.704 | 1.400 | 0.700 |
| Abc | 8 | 38.22 | 5000 | 0.45 | 0.771 | 0.775 | 1.546 | 0.773 |

*** Process Parameters: A: Laser Power, B: Laser Scanning Speed, C: Hatching Distance**

$$\begin{aligned}\delta &= 5.377 - 0.144\cdot 28.15 - 8.522\times10^{-4}\cdot 4000 - 12.479\cdot 0.3\\ &\quad + 3.012\times10^{-5}\cdot 28.15\cdot 4000 + 0.428\cdot 28.15\cdot 0.3\\ &\quad + 2.248\times10^{-3}\cdot 4000\cdot 0.3 - 8.591\times10^{-5}\cdot 28.15\cdot 4000\cdot 0.3\\ &= 0.942\cdot g/cm^3\end{aligned} \tag{6.2}$$

The same is performed for the other seven test points of the $2^3$ factorial design experiment and the predicted density values are calculated. The comparisons of the measured and predicted density values are shown Table 5.10.

As seen from the results in Table 6.2, the difference between the observed and the predicted density values are quite small. However the linear regression model itself was derived from the eight test points of the designed experiment. Thus small error can be expected for these points. For a valid assessment of the accuracy of the developed model, new process configurations, other than those in the experiment, must be tried and test parts at these new configurations must be built and their measured densities must be compared with the predicted values of the model. The new process configurations are specified based on “laser energy density”.

**Table 6.2: Predicted Vs. Measured Values at the $2^3$ Factorial Design of Experiment Test Points**

| Run | Laser Power (W) | Laser Speed (mm/s) | Hatching Distance (mm) | Measured Density* (g/cm3) | Predicted Density (g/cm3) | Error | % Error (Error/Measured) |
|---|---|---|---|---|---|---|---|
| **1** | 28.15 | 4000 | 0.3 | 0.953 | 0.942 | 0.011 | 1.2 |
| **2** | 38.22 | 4000 | 0.3 | 0.968 | 0.96 | 0.008 | 0.8 |
| **3** | 28.15 | 5000 | 0.3 | 0.879 | 0.887 | 0.008 | 0.9 |
| **4** | 38.22 | 5000 | 0.3 | 0.954 | 0.949 | 0.005 | 0.5 |
| **5** | 28.15 | 4000 | 0.45 | 0.769 | 0.776 | 0.008 | 1.0 |
| **6** | 38.22 | 4000 | 0.45 | 0.934 | 0.921 | 0.013 | 1.4 |
| **7** | 28.15 | 5000 | 0.45 | 0.704 | 0.695 | 0.009 | 1.3 |
| **8** | 38.22 | 5000 | 0.45 | 0.773 | 0.754 | 0.019 | 2.5 |

*** Average of replicate test parts**

### 6.1.2 The Effect of Laser Energy Density on Mass Density

In Figure 6.1, for the test points of the $2^3$ factorial design experiment, the measured and predicted apparent mass density versus the laser energy density graph is given. From the graph it is also seen that as the laser energy density increases the density of the laser sintered part also increases, as expected (Section 3.1). However, between the 0.012 J/mm$^2$ and 0.021 J/mm$^2$ values of the laser energy density values, the increase in the energy density results in steep increase in the resultant density, but between the 0.021 J/mm$^2$ and 0.032 J/mm$^2$ values of the laser energy density values, the resultant density do not vary so much and reaches an asymptote around 0.95 g/cm$^3$.

As was discussed before, the measured and predicted values are very close to each other. After analyzing the graph in Figure 6.1, to check the validity of the established mathematical model, additional test parts were built at new process configurations. Each part process configuration is referred as check point.

The parameter combination of the first check point was set as the average of the high and low values of the parameter values set of test points of $2^3$ factorial design experiment: 33.20 W laser power, 4500 mm/s laser speed and 0.38 mm

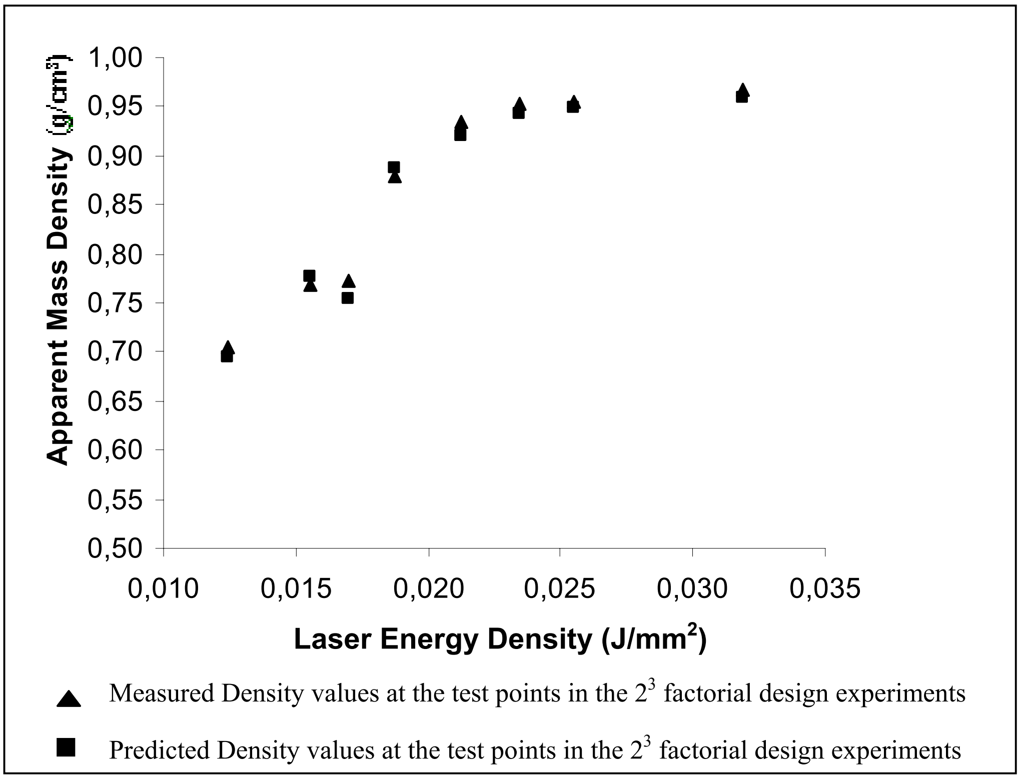


**Figure 6.1: Apparent Mass Density vs. Laser Energy Density**

hatching distance. This point is called the “central point”.

The parameter combinations of the second and third check points are specified such that, the resulting laser energy densities of the parametric configurations of these points lay between the first (0.025 J/mm$^2$) and second (0.032 J/mm$^2$) highest laser energy densities of the parametric configurations of the test points of the designed experiment. The check point 2 (Table 6.3) was designed with 35.23 W laser power, 4500 mm/s laser speed and 0.3 mm hatching distance and the resulting laser energy density of the check point 2 is

$$ED_{checkpo\,\mathrm{int}\,2} = \frac{35.23}{4500 \cdot 0.3} = 0.26 \cdot J / mm^2 \tag{6.3}$$

Similarly, with the parameter settings of check point 3 (Table 6.3), the resulting laser energy density is 0.030 J/mm$^2$.

In contrast to check points 2 and 3, the parameter combination of check point 4 was specified such that the resulting laser energy density of this point lay between the first (0.012 J/mm$^2$) and second (0.016 J/mm$^2$) lowest non laser energy densities of the parametric configurations of the test points of the designed experiment. So the purpose was to fill “empty” spots in the energy density spectrum. The check point 4 (Table 6.3) was designed with 29.64 W laser power, 4500 mm/s laser speed and 0.45 mm hatching distance and the resulting laser energy density of the check point 4 is 0.015 J/mm$^2$.

In Figure 6.2, for the test and check points, the measured and predicted apparent mass densities at varying non-dimensional energy densities for all test parts including the additional check parts. When the measured and the predicted density values of the check points are compared (Table 6.4), it is seen that, the

**Table 6.3: Additional Check Points for Verification of Equation (6.1)**

| Check Point | Laser Power (W) | Laser Speed (mm/s) | Hatching Distance (mm) | Measured Apparent Mass Density (g/cm$^3$) Replicate 1 | Replicate 2 | Density Sum (g/cm$^3$) | Density Avg. (g/cm$^3$) |
|---|---|---|---|---|---|---|---|
| 1 | 33.20 | 4500 | 0.38 | 0.854 | 0.86 | 1.713 | 0.857 |
| 2 | 35.23 | 4500 | 0.3 | 0.944 | 0.963 | 1.907 | 0.954 |
| 3 | 36.54 | 4000 | 0.3 | 0.98 | 0.968 | 1.947 | 0.974 |
| 4 | 29.64 | 4500 | 0.45 | 0.792 | 0.788 | 1.58 | 0.79 |

**Table 6.4: The Predicted vs. Measured Values at Check Points**

| Check Point | Laser Power (W) | Laser Speed (mm/s) | Hatching Distance (mm) | Measured Density* (g/cm$^3$) | Predicted Density (g/cm$^3$) | Error | %Error |
|---|---|---|---|---|---|---|---|
| 1 | 33.2 | 4500 | 0.38 | 0.857 | 0.855 | 0.002 | 0.233 |
| 2 | 35.23 | 4500 | 0.3 | 0.954 | 0.942 | 0.012 | 1.258 |
| 3 | 36.54 | 4000 | 0.3 | 0.974 | 0.957 | 0.017 | 1.45 |
| 4 | 29.64 | 4500 | 0.45 | 0.771 | 0.75 | 0.021 | 2.724 |

*** Average of replicate test parts**

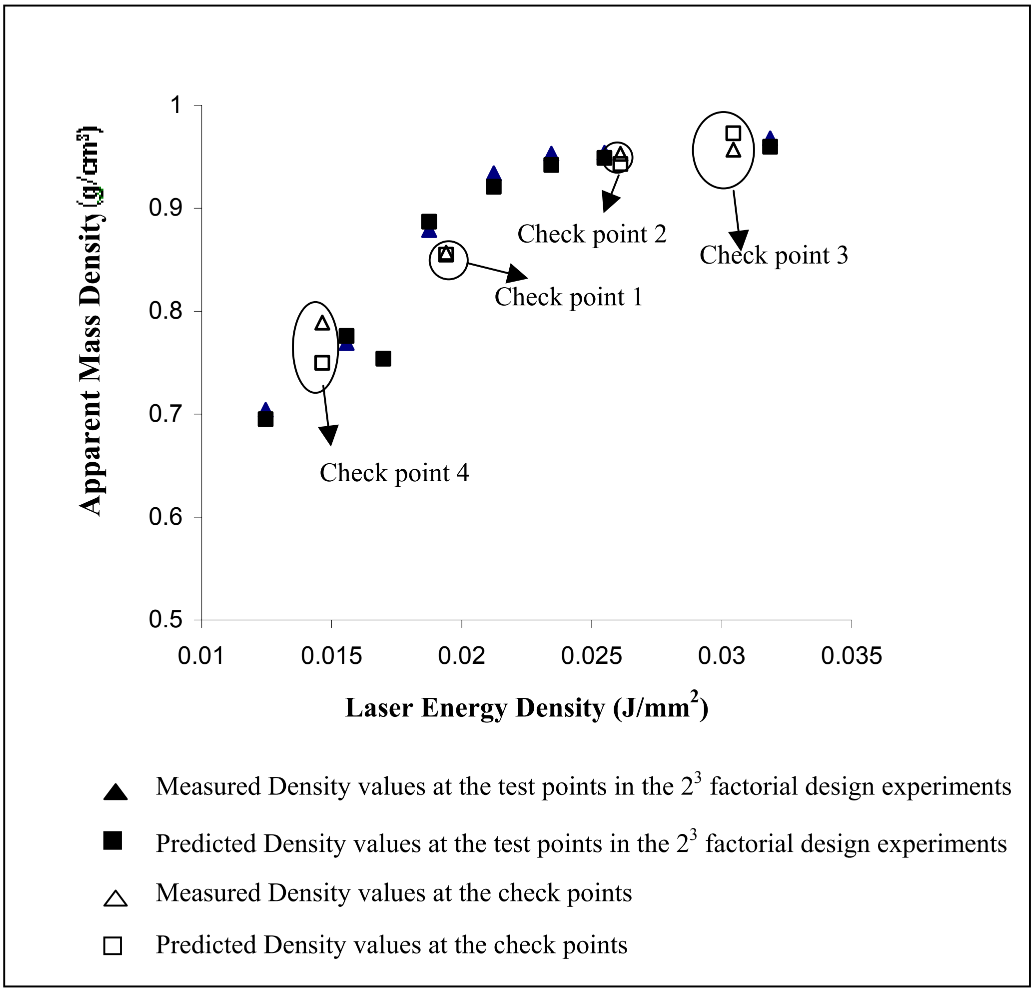


**Figure 6.2: Apparent Mass Density vs. Laser Energy Density**

difference (error) is small. The developed empirical model works enough for the check points, as well as for the $2^3$ factorial design experiment run points.

In the study of Ho et al [11], the resultant mass density of the laser sintered parts were related to the resultant laser energy density with which the parts were produced with, similar to Figure 6.2. In that study, the laser energy density was varied only with respect to laser power. However the underlying promise was that it was the laser energy density value that was the effective factor, rather than the parameters that make up the laser energy density. As follow up to this, in this study, it has been investigated what happens when the parts are sintered with the same laser energy density but with different parameter combinations. In Table 6.5, two groups of test parts are presented for all, each group of which has the

**Table 6.5: Different Parameter Configurations for the Same Energy Density and the Resulting Test Part Mass Densities**

| | Energy Density Test Parts | Laser Power (W) | Laser Speed (mm/s) | Hatching Distance (mm) | Measured Mass Density (g/cm3) | Predicted Mass Density (g/cm3) |
|---|---|---|---|---|---|---|
| **Group 1 ED=0.020 J/mm$^2$** | 1 | 28,15 | 4500 | 0,3 | 0,938 | 0,915 |
| | 2 | 35,23 | 4200 | 0,4 | 0,897 | 0,883 |
| | 3 | 39,45 | 5000 | 0,38 | 0,846 | 0,852 |
| **Group 2 ED=0.027 J/mm$^2$** | 4 | 32,97 | 4000 | 0,3 | 0,967 | 0,951 |
| | 5 | 34,78 | 4200 | 0,3 | 0,932 | 0,949 |
| | 6 | 37,39 | 4500 | 0,3 | 0,968 | 0,951 |

same laser energy density. Within a group, three parts with different parameter configurations (that yields the same energy density value) are built.

The measured and the predicted apparent mass density results of these parts are also shown in table 6.5.

Within the second group, although the measured and predicted mass density values of the part 4 (0.967 g/cm$^3$ and 0.951 g/cm$^3$, respectively) and part 6 (0.968 g/cm$^3$ and 0.951 g/cm$^3$, respectively) are about the same, the mass density of part 5 (0.932 g/cm$^3$ and 0.949 g/cm$^3$, respectively) differs slightly from those of part 4 and 6.

The resulting density values also differ within the first group. Moreover when compared with the second group, it is seen that the variation of density within the first group is much more than it is, for the second group. It should be noted that the variation between the parameter values in the first group is greater than it is in the second group.

The energy density cannot be used as the sole influential factor for porosity of the laser sintered parts; same energy density does not always result in the same apparent mass density. The specific values of the parameters that combine to make up the energy density are effective. That is for a given energy density value, different combinations of parameters that make it up yield different porosities.

### 6.1.3 The Part Porosity

So far, the porosity of the parts has been expressed by apparent mass density. The approximate porosity in these parts are can be calculated by using the true density of the polymer powder, PA. The true density of PA varies, depending on how it is processed. However this variation is not too large and a reasonable approximation for porosity can be made, based on this study.

The porosity percentage calculations of the parts are preformed by comparing the density of all the test parts with the true density of the polyamide, with the following formula

$$\phi_i = \left(1 - \frac{\rho_i}{\rho_{PA}}\right) \cdot 100 \tag{6.5}$$

where $\phi_i$ is the % porosity of the part, $\rho_i$ is the apparent density of the part and $\rho_{PA}$ is the true density of the polyamide. The average true density of the polyamide is specified as 1.15 g/cm$^3$ [31]. In Table 6.6, the calculated porosity values of the produced test parts are listed, along with the corresponding process configurations and the resulting laser energy densities. In Figure 6.3, the laser

**Table 6.6: The Calculated Porosity of Produced Irregular Porous Test Parts**

| | | Laser Power (W) | Laser Speed (mm/s) | Hatching Distance (mm) | Laser Energy Density (J/mm$^2$) | Measured Density (g/cm$^3$) | Calculated Porosity $\rho_{PA}$=1.15g/cm/3 |
|---|---|---|---|---|---|---|---|
| $2^3$ Factorial Design Test points | 1 | 28.15 | 4000 | 0.3 | 0,023 | 0.953 | 17.130 |
| | 2 | 38.22 | 4000 | 0.3 | 0,032 | 0.968 | 15.826 |
| | 3 | 28.15 | 5000 | 0.3 | 0,019 | 0.879 | 23.565 |
| | 4 | 38.22 | 5000 | 0.3 | 0,025 | 0.954 | 17.043 |
| | 5 | 28.15 | 4000 | 0.45 | 0,016 | 0.769 | 33.130 |
| | 6 | 38.22 | 4000 | 0.45 | 0,021 | 0.934 | 18.782 |
| | 7 | 28.15 | 5000 | 0.45 | 0,012 | 0.704 | 38.782 |
| | 8 | 38.22 | 5000 | 0.45 | 0,017 | 0.773 | 32.782 |
| Additional Test Parts for Validification (Check Points) | 1 | 33.2 | 4500 | 0.38 | 0,019 | 0.857 | 25.478 |
| | 2 | 35.23 | 4500 | 0.3 | 0,026 | 0.954 | 17.043 |
| | 3 | 36.54 | 4000 | 0.3 | 0,030 | 0.974 | 15.304 |
| | 4 | 29.64 | 4500 | 0.45 | 0,015 | 0.771 | 32.956 |

energy density versus the porosity graph of all part is shown. As expected, as the laser energy density increases the resultant porosity on the part decreases. Similar to the effect on the mass density, between the 0.012 J/mm$^2$ and 0.021 J/mm$^2$ values of the laser energy density values, the increase in the energy density results in steep decrease in the resultant porosity, but between the 0.021 J/mm$^2$ and 0.032 J/mm$^2$ values of the non-dimensional energy density, the resulting porosity does not vary so much and reaches an asymptote around 16%. Approximately this is also the about the lowest porosity that is achieved for this powder. It should be noted that the part porosity gain as high as almost 40%, which is quiet high.

Sections of the three test parts with low porosity (Test point 2) and high porosity (Test Point 7) and mid porosity (Check Point 1, central point) have been visualized through a Scanning Electron Microscope (SEM) machine in the METU Metallurgical Engineering Department was used. The results are presented in

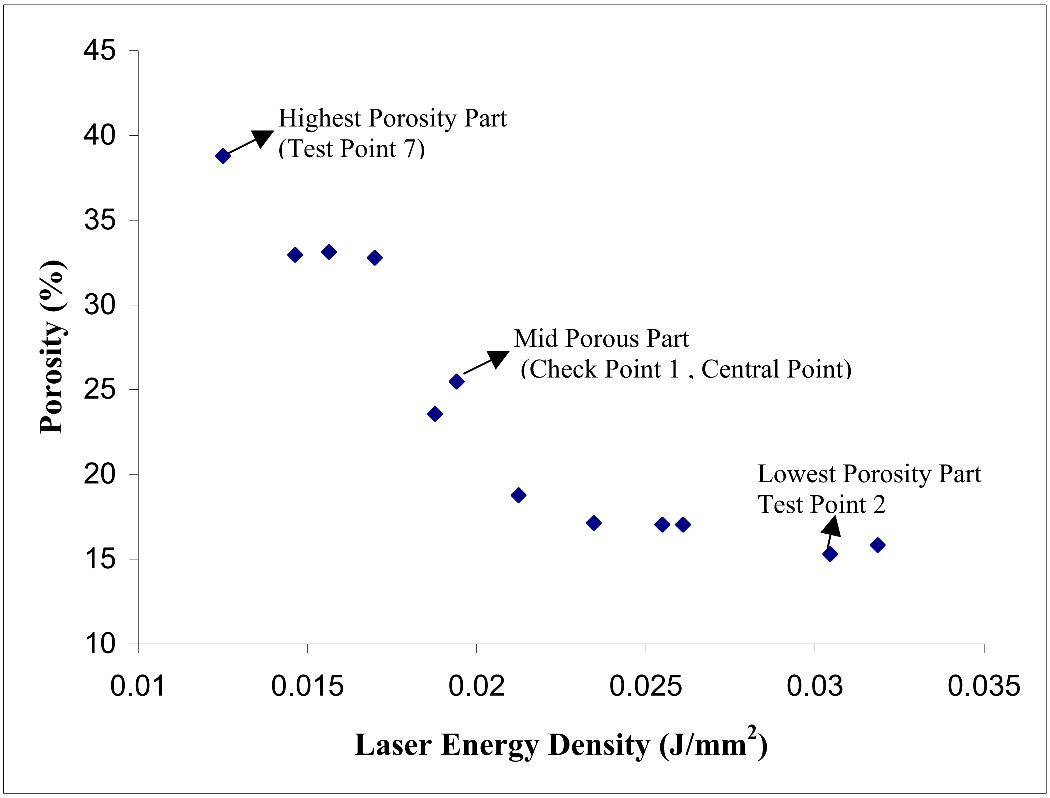


**Figure 6.3: The non-dimensional energy density versus the porosity for irregular porous test parts**

Figures 6.4, 6.5 and 6.6. The shown sections are on the XY plane of the parts during the production. Lots of different sized pores were observed in all parts. Between the visualized parts a gross change in the sizes of the irregular pores were not observed. However a significant change in the number of pores (frequency of pores) on each section has been observed. Specifically, a decreasing pore population can be observed from Figure 6.4 (high porosity part) towards Figure 6.6 (low porosity part).

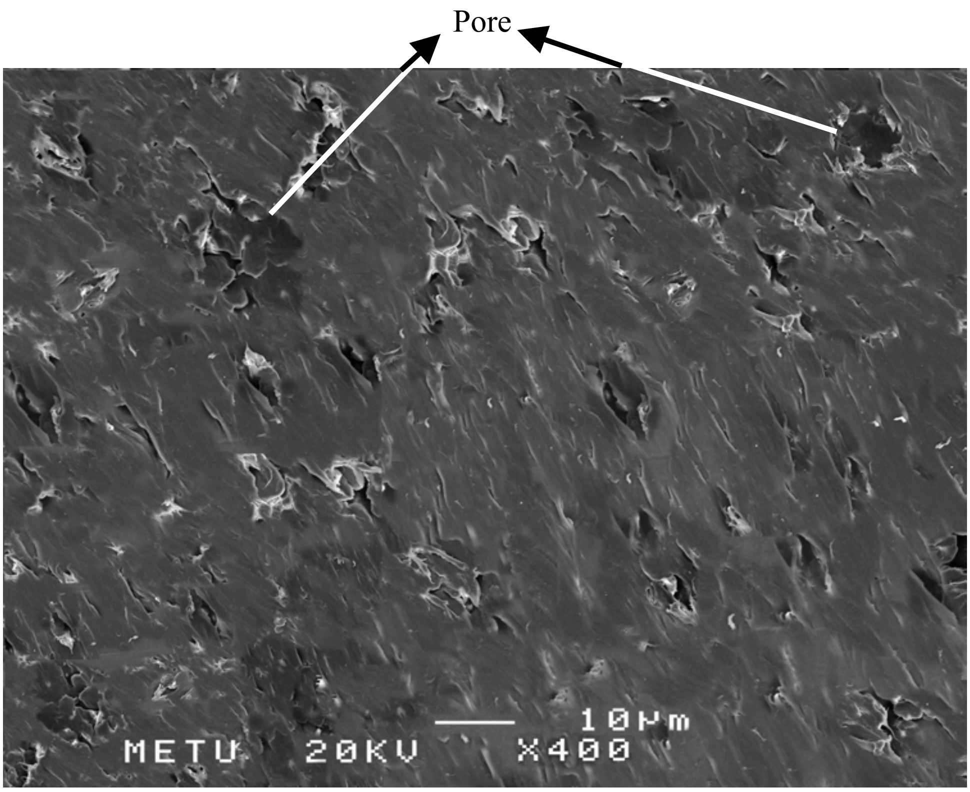


**Figure 6.4: A section of the high porosity part (Test Point 7)**

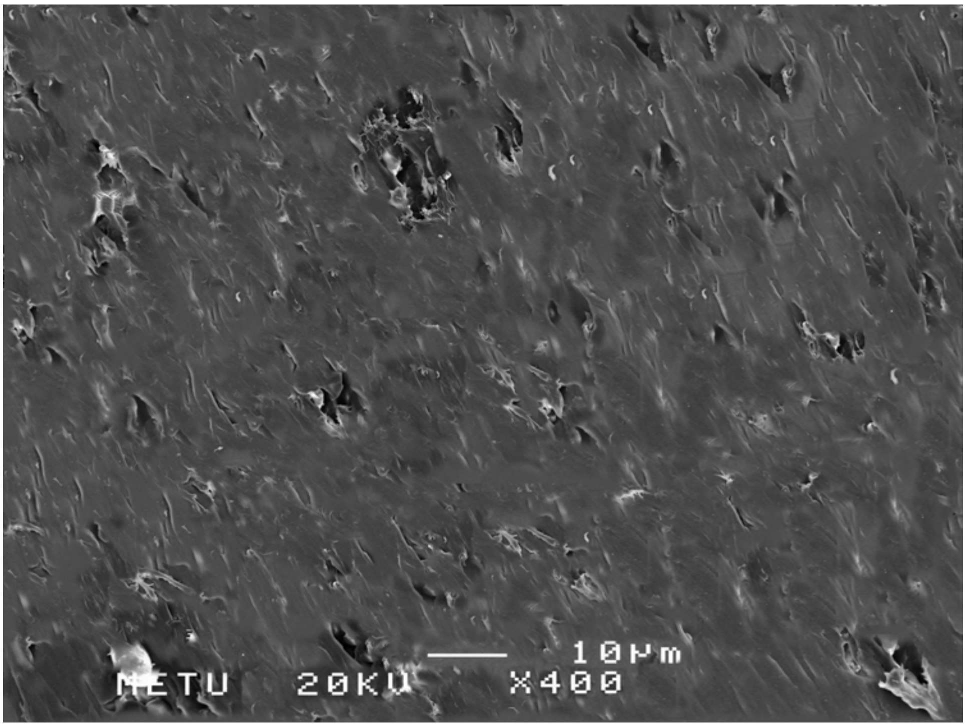


**Figure 6. 5: A section of the mid porosity part, (Check Point 1)**

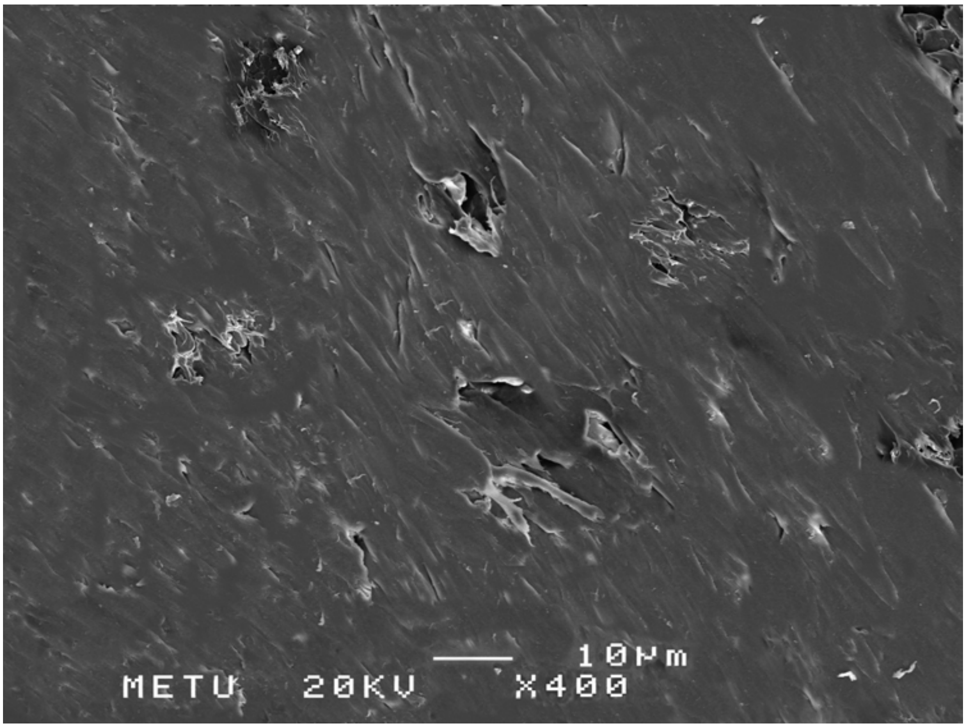


**Figure 6.6: A section of the low porosity part (Test Point 7)**

## 6.2 Hole Structures (Regular Porous Structures)

In order to study the accuracy with which the hole structures could be built in SLS, as well as the limiting size of such features, three different types of hole structures had been manufactured as explained in Chapter 2. In this section, the resulting dimensions of the designed parts are presented and discussed.

### 6.2.1 Test Part 1

After the fabrication of Test Part 1, sand-blasting alone was observed to be insufficient to remove the unsintered loose powder inside holes. The unsintered powder needed to be poked to loosen and be released from the parts, followed by further sand-blasting.

Rather than the original model square geometry, all holes on Test Part 1 were seen to be rounded at the corners. This is expected since the laser beam path cannot contour sharp corners properly due to its finite width during laser exposure and the intended sharp corner relaxes into a smooth curvature in the absence of confinement.

The hole size and wall thickness measurements are done, first by touching the inner walls of the holes and then calculating the distances between these touched points (P1, P2…P8, in Figure 5.7). For each hole group, three hole sizes and four wall thicknesses measurements are done, as shown in Figure 5.7.

The average measured values and the standard deviations of the hole sizes and the wall thicknesses for each hole group are shown in Table 6.7. In the table, also, the deviations between the nominal (designed dimensions before scaling with shrinkage factors) values and the measured dimensions of the hole sizes and wall thicknesses are also shown.

On Test Part 1, for all the wall sections, on which the “EDGES” scan type was applied (1.A, 1.B, 1.C, 2.A, 2.B and 3.B), it is seen that the wall thickness values are very close to each other and range between 0.739 mm and 0.747 mm.

**Table 6.7: Measured Dimensions of Hole Features of Test Part 1**

**All Dimensions in mm**

| Pore Group | Nominal HS* | Nominal WT* | Scaled** HS | Scaled** WT | Measured HS | Measured WT | Deviation (Measured- Nominal) HS | Deviation (Measured- Nominal) WT | Type of Wall Scan |
|---|---|---|---|---|---|---|---|---|---|
| 1.A*** | 2 | 0.2 | 2 | 0.2 | 1.298 ± 0.013 | 0.746 ± 0.037 | -0.702± 0.013 | 0.546±0.037 | EDGES |
| 1.B*** | 2 | 0.2 | 1.937 | 0.1937 | 1.277 ± 0.010 | 0.743 ± 0.012 | -0.723± 0.010 | 0.543±0.012 | EDGES |
| 1.C*** | 2 | 0.2 | 2.064 | 0.2064 | 1.406 ± 0.010 | 0.763 ± 0.031 | -0.594± 0.010 | 0.563±0.031 | EDGES |
| 2.A | 2 | 0.66 | 2 | 0.66 | 1.809 ± 0.037 | 0.743 ± 0.034 | -0.191±0.037 | 0.066±0.034 | EDGES |
| 2.B | 2 | 0.66 | 1.937 | 0.639 | 1.708 ± 0.016 | 0.739 ± 0.028 | -0.292±0.016 | 0.079±0.028 | EDGES |
| 2.C | 2 | 0.66 | 2.064 | 0.6811 | 1.568 ± 0.015 | 1.082 ± 0.023 | -0.432±0.015 | 0.422±0.023 | Contouring Only |
| 3.A | 2 | 0.68 | 2 | 0.68 | 1.508 ± 0.021 | 1.057 ± 0.033 | -0.492±0.021 | 0.377±0.033 | Contouring Only |
| 3.B | 2 | 0.68 | 1.937 | 0.6589 | 1.756 ± 0.012 | 0.747 ± 0.014 | -0.244±0.012 | 0.089±0.014 | EDGES |
| 3.C | 2 | 0.68 | 2.064 | 0.7017 | 1.558 ± 0.033 | 1.103 ± 0.024 | -0.442±0.033 | 0.423±0.024 | Contouring Only |
| 4.A | 2 | 1.2 | 2 | 1.2 | 1.782 ± 0.020 | 1.288 ± 0.013 | -0.218±0.020 | 0.081±0.013 | Contouring + Hatching |
| 4.B | 2 | 1.2 | 1.93798 | 1.1627 | 1.708 ± 0.049 | 1.278 ± 0.023 | -0.292±0.049 | 0.078±0.023 | Contouring Only |
| 4.C | 2 | 1.2 | 2.064 | 1.2384 | 1.907 ± 0.011 | 1.269 ± 0.014 | -0.093±0.011 | 0.069±0.011 | Contouring + Hatching |

***HS stands for the hole size, WT stands for the wall thickness**
**** With shrinkage factor**
***** A for shrinkage factor 1, B for shrinkage factor 0.968, C for shrinkage factor 1.032**

As expected these are the smallest wall thickness values in all measurements, due to the nature of the scan type. Although the values are close to each other (dictated by a single contour pass), the deviations from design values vary. Effective beam diameter being 0.68 mm and the contour beam offset 0.34 mm; the measured wall thicknesses indicate that the actual effective beam diameter is probably greater than 0.68 mm.

Within all major groups (1,2,3,4) it is seen that, in 1.032 shrinkage factor hole groups (1.C, 2.C, 3.C, 4.C), the amount of positive deviation in wall thickness is almost exactly compensated by the negative deviation in hole size ($\Delta HS \cong \Delta WT$). Whereas for the unscaled hole groups, shrinkage factor is 1, (1.A, 2.A, 3.A, 4.A) and 0.968 shrinkage factor scaled hole group (1.B, 2.B, 3.B, 4.B), the amount of positive deviation in wall thickness is smaller than the amount of negative deviation in hole size ($\Delta HS > \Delta WT$). For example, within the 1$^{st}$ major group, for the 1.C hole group, the positive deviation in the wall thickness value (0.563 mm) is very close to the negative deviation in the hole size value (0.591 mm). However for the unscaled hole group (1.A) and 0.968 shrinkage factor hole group (1.B), the amount of positive deviation in wall thickness (0.546 mm and 0.543 mm, respectively) is smaller than the amount of negative deviation in hole size (0.702 mm and 0.703 mm respectively). The effect of shrinkage factor on dimensional accuracy is further investigated in Test Part 2.

For the major groups 2 and 3 , the nominal wall thickness values are close or equal to “ 2 x beam offset for contour”, i.e. 0.68 mm. Within these two major groups, hole groups 2C, 3A and 3C showed the largest deviation in wall thickness values (0.422 mm, 0.377 mm and 0.423 mm, respectively). In these hole groups the type of scan is “Contouring Only”. As shown in Figure 2.10(a), the wall sections of these hole groups were scanned with two overlapping contour exposures. This resulted in double exposure of the wall sections (compared to EDGES type of scan), absorbing more energy per area and resulting in thicker sections with greater deviation. In hole group 4.B where the same scan type was applied on the wall sections, the amount of deviation between the measured and intended wall thickness is very small (0.078 mm) due to the larger wall thickness (1.16 mm).

As the positive deviation in wall thickness increases, it is compensated through a larger negative deviation in hole size. The largest positive deviations in wall thicknesses are seen on the first group (0.546 mm, 0.543 mm and 0.563 mm) as the nominal (designed value) of the wall thickness was 0.2 mm, which is the thinnest of all. Thus, the smallest hole sizes were obtained in hole group 1.

For the “EDGES” type of scan (1.A, 1.B, 1.C, 2.A, 2.B and 3.B), it is seen that the smallest deviation in wall thickness were obtained with the hole group 2.A. When this group is compared with others (1.A, 1.B, 1.C, 2.B and 3.B), it is seen that, the scaled wall thickness of hole group 2.A (0.66 mm) is the largest.

Similarly for the hole groups İN which the wall sections are scanned with the “Contouring Only” type of scan (2.C, 3.A, 3.C, and 4.B), the smallest deviation in wall thickness was obtained with the hole group (4.B), of which the scaled wall thickness (1.16 mm) is the largest again.

For the hole groups on which the wall sections are scanned with the “Contouring and Hatching” type of scan (4.A, 4.C), it is seen that the deviation in wall thickness between these group are about the same (0.089 mm and 0.069 mm). For the “Contouring and Hatching” type of scan, the effect of the increased wall thickness on the dimensional accuracy of the hole features will be further investigated in Test Part 2.

### 6.2.2 Test Part 2

Test Part 2 was manufactured similar to Test Part 1. However in this case, the type of scan is controlled for each group of hole. The results of the CMM measurements of porous features in Test Part 2 are shown in Table 6.8. As in Test Part 1, in 1.032 shrinkage factor holes (1.C and 2C), the amount of positive deviation in wall thickness, 0.218 mm and 0.079 mm, respectively, are almost exactly compensated by the negative deviation in hole size, 0.228 mm and 0.095

mm, respectively ($\Delta HS \cong \Delta WT$). Whereas for the unscaled hole groups (1.A and 2.A) and 0.968 shrinkage factor scaled hole group (1.B and 2B), the amount of positive deviation in wall thickness is smaller than the amount of negative deviation in hole size ($\Delta HS > \Delta WT\uparrow$). These results are similar to those for Test Part1.

When the deviation from the design values of the wall thicknesses on Test Part 2 are compared, it is seen that they do not differ from each other within major hole groups. This was expected as the type of the scan does not change within the major hole groups and the scaled wall thicknesses of the minor hole groups are very close to each other. However when the deviation between the nominal (design value) and measured hole size values are compared, within each major hole group the 1.032 shrinkage factor groups (1.C and 2.C) resulted in the smallest deviations in hole size (0.208 mm and 0.095 mm). As the type of scan does not change within major hole group, it is concluded that shrinkage factor alone, is quite influential in the dimensional accuracy of the hole sizes, for a given scan type.

In Table 6.9, the comparison of the hole groups of Test Part 1 and Test Part 2 for “Contouring and Hatching” type of scan is given. When the hole groups with the same shrinkage factor are compared (4A-2A and 4B-2B) it is seen that the deviations in the hole size and wall thickness do not differ between these holes groups and the accuracy of the dimensions are about the same, although the scaled wall thickness differs. Thus, unlike the other scan types (EDGES and “Contouring Only”), the increase in the scaled wall thickness value with the same shrinkage factor does not provide better but about the same accuracy in “Contouring and Hatching” type of scan.

**Table 6.8: Measured Dimensions of Hole Features of Test Part 2**

| All Dimensions in mm | | | | | | | Deviation (Measured-Nominal) | | |
|---|---|---|---|---|---|---|---|---|---|
| Pore Group | Nominal HS* | Nominal WT* | Scaled** HS | Scaled** WT | Measured HS (Average) | Measured WT (Average) | HS | WT | Type of Wall Scan |
| 1.A*** | 2 | 0.9 | 2 | 0.9 | 1.711 ± 0.021 | 1.112 ± 0.010 | -0.289±0.021 | 0.212 ± 0.010 | Contouring Only |
| 1.B*** | 2 | 0.9 | 1.937 | 0.871 | 1.684 ± 0.012 | 1.109 ± 0.007 | -0.316±0.012 | 0.209 ± 0.012 | Contouring Only |
| 1.C*** | 2 | 0.9 | 2.064 | 0.929 | 1.772 ± 0.015 | 1.118 ± 0.009 | -0.228±0.015 | 0.218 ± 0.015 | Contouring Only |
| 2.A | 2 | 1.4 | 2 | 1.4 | 1.759 ± 0.008 | 1.478 ± 0.012 | -0.241±0.008 | 0.078 ± 0.008 | Contouring +Hatching |
| 2.B | 2 | 1.4 | 1.937 | 1.357 | 1.716 ± 0.033 | 1.47 ± 0.007 | -0.284±0.033 | 0.07 ± 0.033 | Contouring +Hatching |
| 2.C | 2 | 1.4 | 2.064 | 1.445 | 1.905 ± 0.039 | 1.479 ± 0.010 | -0.095±0.039 | 0.079 ± 0.039 | Contouring +Hatching |

***HS stands for the pore size, WT stands for the wall thickness**
**** With shrinkage factor**
***** A for shrinkage factor 1, B for shrinkage factor 0.968, C for shrinkage factor 1.032**

**Table 6.9: The Effect of Change in Wall Thickness for "Contouring and Hatching" Type of Scan**

| All dimensions in mm | | | | | | | | Deviation (Measured-Nominal) | | |
|---|---|---|---|---|---|---|---|---|---|---|
| Test Part | Pore Group | Nominal HS* | Nominal WT* | Scaled** HS | Scaled** WT | Measured HS (Average) | Measured WT (Average) | HS | WT | Type of Wall Scan |
| 1 | 4.A*** | 2 | 1.2 | 2 | 1.205 | 1.782 ± 0.020 | 1.288 ± 0.013 | -0.218 ± 0.020 | 0.088 ± 0.013 | Contouring + Hatching |
| | 4.C*** | 2 | 1.2 | 2.064 | 1.238 | 1.907 ± 0.011 | 1.269 ± 0.014 | -0.093 ± 0.011 | 0.069 ± 0.014 | Contouring + Hatching |
| 2 | 2.A | 2 | 1.4 | 2 | 1.4 | 1.759 ± 0.008 | 1.478 ± 0.012 | -0.24 ± 0.008 | 0.078 ± 0.012 | Contouring +Hatching |
| | 2.C | 2 | 1.4 | 2.064 | 1.445 | 1.905 ± 0.009 | 1.479 ± 0.010 | -0.095 ± 0.039 | 0.079 ± 0.010 | Contouring +Hatching |

***HS stands for the pore size, WT stands for the wall thickness**
**** With shrinkage factor**
***** A for shrinkage factor 1, C for shrinkage factor 1.032**

### 6.2.3 Test Part 3

Unlike Test Parts 1 and 2, Test Part 3 also includes changing hole size. Here, the shrinkage is kept constant, thus the hole size and wall thickness alone are studied. After the fabrication of Test Part 3, similar to Test Parts 1 and 2, again sand-blasting alone was observed to be insufficient in removing the unsintered loose powder inside of the holes. The unsintered powder needed to be poked to loosen and be released from the parts, followed by further sand-blasting. Even so, for the 1 mm holes in Test Part 3, the powder inside the holes could not be removed without damage to the part (Figure 6.7).

Similar to other test parts, rather than the original model square geometry, all holes on Test Part 3 were seen to be rounded at the corners. However when the corners of 3 mm and 2 mm holes are compared (Figure 6.8), it is seen that the amount of curvature on the corners of the 3 mm holes are slightly smaller than it is for the 2 mm holes.

As the powder inside of 1 mm holes could not be removed, no dimension measurements on the 1 mm holes could be done. CMM measurements for the rest of the holes are shown in Table 5.4. For all the hole groups it is seen that measured hole dimensions in X and Y directions do not differ from each other.

The results of Test Part 3 are similar when compared with the results of Test Part 1 and 2. As all the holes of Test Part 3 were scaled with 1.032 shrinkage factor, the amount of positive deviation in wall thickness are almost exactly compensated by the negative deviation in hole size for all hole groups

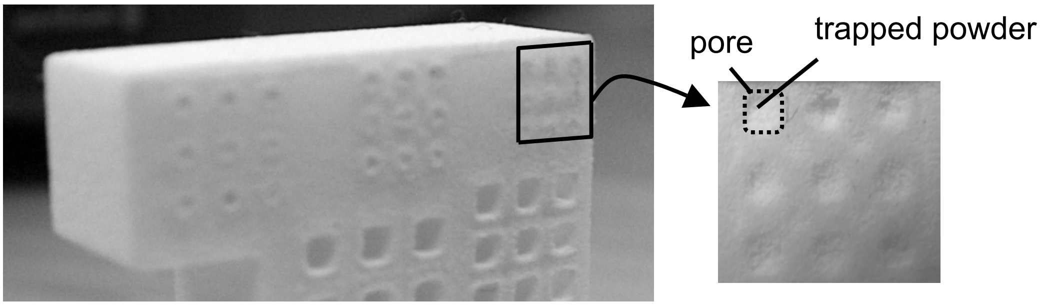


**Figure 6.7: Trapped powder in 1 mm holes of Test Part 3**


2 mm holes with 0.68 mm
wall thickness


2 mm holes with 1.4 mm
wall thickness

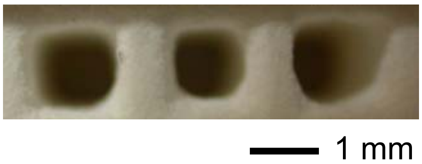


3 mm holes with 0.68 mm
wall thickness

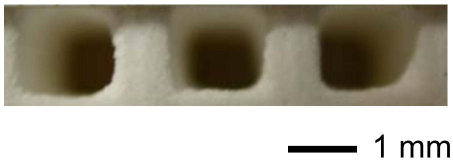


3 mm holes with 1.4 mm
wall thickness

**Figure 6.8: Comparison of the amount of curvature between 2mm and 3mm holes**

($\Delta HS \cong \Delta WT$). This result is the same as those in Test Parts 1 and 2.

For the same nominal hole size, shrinkage factor and wall thickness, the deviation in Test Part 3 are about the same as those in Test Part 1 (groups 3C and 4.C) and Test Part 2 (group 2.1).

For the two different hole sizes (2 mm and 3 mm), it is seen that the amount of the deviation from the design value in the wall thickness are about same and it decreases as the designed wall thickness is increased. This indicates that the deviation from the design value depends on the thickness of the wall (i.e. type of the scan) not on the hole size.

### 6.2.4 Lattice Structures

In addition to the three tubular cubic hole structures, lattice structures are designed and built as explained in Chapter 2. After the lattice structures were produced, it was easily seen that, on all of them, the shape of the holes on the XZ and YZ plane (Figure 2.18 (a)), turned out to rectangular, instead of designed square shape. Although the manufacturer specified shrinkage value in Z direction, 1.013, was applied to lattice structures, in all lattices it is easily observed that the size of all the holes in Z direction is small when compared to their designed value, 2 mm.

**Table 6.10: Measured Dimensions of Hole Features of Test Part 3**

| **All dimensions in mm** | | | | | | Deviation (Measured-Nominal) | | |
|---|---|---|---|---|---|---|---|---|
| Nominal HS* | Nominal WT* | Scaled** HS | Scaled** WT | Measured HS (Avg.) | Measured WT (Avg.) | HS | WT | Type of Wall Scan |
| 3 mm | 0.68 | 3.096 | 0.7 | 2.597 ± 0.020 | 1.07 ± 0.016 | -0.403± 0.020 | 0.390 ± 0.016 | Contouring Only |
| | 1.4 | 3.096 | 1.44 | 2.908 ± 0.016 | 1.473 ± 0.018 | -0.092± 0.016 | 0.074 ± 0.018 | Contouring+ Hatching |
| 2 mm | 0.68 | 2.064 | 0.7 | 1.578 ± 0.013 | 1.068 ± 0.012 | -0.423± 0.013 | 0.388 ± 0.012 | Contouring Only |
| | 1.4 | 2.064 | 1444,8 | 1.911 ± 0.017 | 1.474± 0.008 | -0.089± 0.017 | 0.074 ± 0.008 | Contouring+ Hatching |

***HS stands for the pore size, WT stands for the wall thickness**
*** With shrinkage factor 1.032**

In the first lattice structure it was seen that, the walls inside the lattice structure were observed to be very brittle and break very easily. The reason for that was understood after the analysis of the sliced file of the 1st lattice structure (Figure 5.5). As the wall thickness between the holes in the 1st lattice is 0.66 mm, the exposed areas at the interior intersection sides of the holes are very small, which results in very brittle walls. This brittleness was not observed on other lattices.

For the lattice structures, in addition to the deviations of the hole size wall thickness, the overall part dimensions on the XY plane were also measured. The positions that the probe of the CMM was touched during the measurements on lattice structures are shown in Figure 5.12(b). For each lattice structure, measurements were performed on three different rows of holes, which lie on different planes, on XY, XZ and YZ plane (Figure 5.12(a)). For the XY and XZ

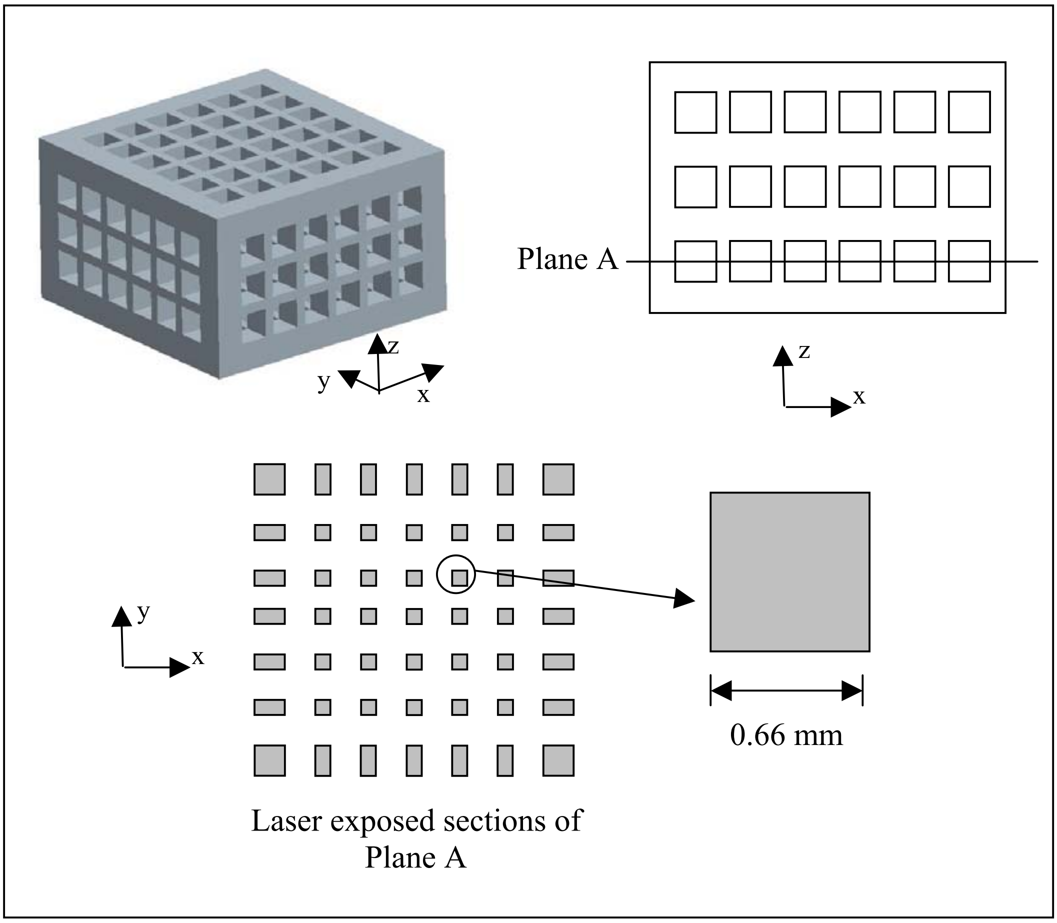


**Figure 6.9: The brittleness problem in the 1st lattice structure**

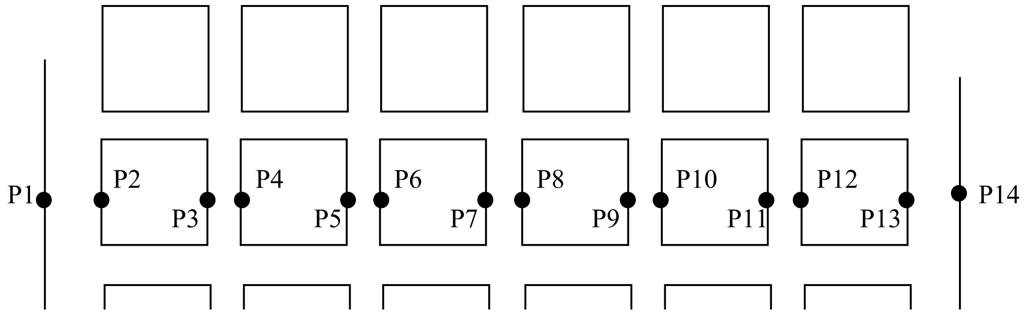


**Figure 5.12 (b): CMM measurement points on lattice structures**

plane, the measurements (hole sizes and wall thicknesses) were performed in X direction and for the YZ plane they were in the Y direction, i.e. no hole size or wall thickness measurements were performed in Z direction.. For each lattice, the actual distance between P1 and P14 points, in Figure 5.12(b), gives the side length of the part. The distance between other points (P2,P3….P13) give the hole sizes or the wall thicknesses between holes, and the distance between P1-P2 and P13-P14 gives the thickness of the surrounding wall. The results of the measurements for the lattice structures are presented in Table 6.11, 6.12 and 6.13.

In the measurements performed in all lattice structures, it is seen that outer (side length, in Table 6.11-6.13) dimensions of the lattice are slightly smaller than the nominal dimensions.

In all previous test parts, the actual wall thicknesses measured turned out to be greater (positive deviation) than their designed values with any type of scan. This situation also exists for the inner walls (between holes) of the lattice structures, however the thickness of the surrounding walls (SWT1 and SWT2) are smaller (negative deviation) than their designed values (2 mm). Compared to other wall thickness deviations, these deviations are small and the resulting thicknesses approximate nominal values well.

To compare the measured hole size and wall thickness values of lattice structures with other test parts, Table 6.14 is constructed. In each lattice structure, the shrinkage factor in X and Y direction was 1.032 and it is again seen that the amount of positive deviation in wall thicknesses are very close to the negative deviation in the hole sizes.

When the results of the 3rd lattice structure is compared with the results of hole group 2.C of Test Part 2 (in Table 6.7), and with the 2 mm hole size, 1.4 mm wall thickness hole group of Test Part 3 it is seen that the deviations from the designed values are almost same. The deviations in the hole size and wall thickness in the 3rd lattice are around 0.087 mm and 0.078 mm respectively. For the hole group 2.C on Test Part 2 and the 2 mm hole size, 1.4 mm wall thickness hole group of Test Part 3, the hole size deviations are 0.095 mm and 0.089 mm and the wall thickness deviations are 0.079 mm and 0.074 mm, respectively.

When the results of 2nd lattice structure (wall thickness is 1.1 mm) is compared with the results of 1.C hole group Test Part 2 (wall thickness is 0.9 mm), in Table 6.8, (on the wall sections of both, "Contouring Only" type of scan is performed), it is again seen that the accuracy of 2nd lattice structure is better than 1.C hole group Test Part 2, as the wall thickness between the holes are larger for the 2nd lattice structure.

When the measured wall thicknesses for the 1st lattice structures are compared with all similar hole groups of test parts, on the wall sections of which EDGES type of scan is employed, it is seen that the deviations from the designed values are again same.

Thus, as the deviations results for the lattice structure are almost same with the same kind of holes of previous test parts, it is concluded that the dimensional accuracy of the hole features do not vary with their structure (tubular or lattice).

**Table 6.11: Measured Dimensions of Hole Features on 1st Lattice Structures**

| All dimensions in mm<br>Shrinkage Factor: 1.032 | | Side length (w) | SWT1 | HS1 | WT1 | HS2 | WT2 | HS3 | WT3 | HS4 | WT4 | HS5 | WT5 | HS6 | SWT2 |
|---|---|---|---|---|---|---|---|---|---|---|---|---|---|---|---|
| | Distance Between Points | P1-P14 | P1-P2 | P2-P3 | P3-P4 | P4-P5 | P5-P6 | P6-P7 | P7-P8 | P8-P9 | P9-P10 | P10-P11 | P11-P12 | P12-P13 | P13-P14 |
| | **Nominal** | **19.250** | **2.000** | **2.000** | **0.650** | **2.000** | **0.650** | **2.000** | **0.650** | **2.000** | **0.650** | **2.000** | **0.650** | **2.000** | **2.000** |
| On XY plane | Measured | 19.166 | 1.980 | 1.939 | 0.754 | 1.902 | 0.736 | 1.901 | 0.748 | 1.906 | 0.731 | 1.909 | 0.745 | 1.932 | 1.983 |
| | **Deviation (Measured Nominal )** | **-0.084** | **-0.020** | **-0.061** | **0.104** | **-0.098** | **0.086** | **-0.099** | **0.098** | **-0.094** | **0.081** | **-0.091** | **0.095** | **-0.068** | **-0.017** |
| On XZ plane | Measured | 19.137 | 1.970 | 1.921 | 0.762 | 1.899 | 0.739 | 1.903 | 0.755 | 1.894 | 0.732 | 1.901 | 0.748 | 1.927 | 1.986 |
| | **Deviation (Measured Nominal )** | **0.113** | **-0.030** | **-0.079** | **0.112** | **-0.101** | **0.089** | **-0.097** | **0.105** | **-0.106** | **0.082** | **-0.099** | **0.098** | **-0.073** | **-0.014** |
| On YZ plane | Measured | 19.142 | 1.974 | 1.931 | 0.759 | 1.901 | 0.753 | 1.903 | 0.732 | 1.894 | 0.754 | 1.894 | 0.744 | 1.931 | 1.972 |
| | **Deviation (Measured Nominal )** | 0.108 | **-0.026** | **-0.069** | **0.109** | **-0.099** | **0.103** | **-0.097** | **0.082** | **-0.106** | **0.104** | **-0.106** | **0.094** | **-0.069** | **-0.028** |

***HS stands for the hole size, WT stands for the wall thickness, SWT stands for the thickness of the wall surrounding the holes**
***On the walls WT1, WT2, WT3 and WT4 "EDGES" type of scan, on the walls SWT1 and SWT2 "Contouring+Hatching" type of scan is performed**

**Table 6.12: Measured Dimensions of Hole Features on 2nd Lattice Structures**

| All dimensions in mm Shrinkage Factor: 1.032 | | Side length (w) | SWT1 | HS1 | WT1 | HS2 | WT2 | HS3 | WT3 | HS4 | WT4 | HS5 | WT5 | HS6 | SWT2 |
|---|---|---|---|---|---|---|---|---|---|---|---|---|---|---|---|
| | Distance Between Points | P1-P14 | P1-P2 | P2-P3 | P3-P4 | P4-P5 | P5-P6 | P6-P7 | P7-P8 | P8-P9 | P9-P10 | P10-P11 | P11-P12 | P12-P13 | P13-P14 |
| | **Nominal** | **21.500** | **2.000** | **2.000** | **1.100** | **2.000** | **1.100** | **2.000** | **1.100** | **2.000** | **1.100** | **2.000** | **1.100** | **2.000** | **2.000** |
| XY plane | Measured | 21.375 | 1.973 | 1.916 | 1.210 | 1.879 | 1.216 | 1.875 | 1.228 | 1.876 | 1.211 | 1.886 | 1.208 | 1.922 | 1.975 |
| | **Deviation (Measured Nominal)** | **-0.125** | **-0.027** | **-0.084** | **0.110** | **-0.121** | **0.116** | **-0.125** | **0.128** | **-0.124** | **0.111** | **-0.114** | **0.108** | **-0.078** | **-0.025** |
| XZ plane | Measured | 21.401 | 1.983 | 1.924 | 1.205 | 1.877 | 1.221 | 1.871 | 1.222 | 1.879 | 1.215 | 1.880 | 1.214 | 1.929 | 1.981 |
| | **Deviation (Measured Nominal )** | **-0.099** | **-0.017** | **-0.076** | **0.105** | **-0.123** | **0.121** | **-0.129** | **0.122** | **-0.121** | **0.115** | **-0.120** | **0.114** | **-0.071** | **-0.019** |
| YZ plane | Measured | 21.382 | 1.976 | 1.921 | 1.213 | 1.881 | 1.211 | 1.875 | 1.225 | 1.878 | 1.210 | 1.887 | 1.208 | 1.918 | 1.979 |
| | **Deviation (Measured Nominal)** | **-0.118** | **-0.024** | **-0.079** | **0.113** | **-0.119** | **0.111** | **-0.125** | **0.125** | **-0.122** | **0.110** | **-0.113** | **0.108** | **-0.082** | **-0.021** |

***HS stands for the hole size, WT stands for the wall thickness, SWT stands for the thickness of the wall surrounding the holes**
***On the walls WT1, WT2, WT3 and WT4 "Contouring only" type of scan, on the walls SWT1 and SWT2 "Contouring+Hatching" type of scan is performed**

**Table 6.13: Measured Dimensions of Hole Features on 3rd Lattice Structures**

| **All dimensions in mm Shrinkage Factor: 1.032** | | **Side length (w)** | **SWT1** | **HS1** | **WT1** | **HS2** | **WT2** | **HS3** | **WT3** | **HS4** | **WT4** | **HS5** | **WT5** | **HS6** | **SWT2** |
|---|---|---|---|---|---|---|---|---|---|---|---|---|---|---|---|
| | Distance Between Points | P1-P14 | P1-P2 | P2-P3 | P3-P4 | P4-P5 | P5-P6 | P6-P7 | P7-P8 | P8-P9 | P9-P10 | P10-P11 | P11-P12 | P12-P13 | P13-P14 |
| | **Nominal** | **23.000** | **2.000** | **2.000** | **1.400** | **2.000** | **1.400** | **2.000** | **1.400** | **2.000** | **1.400** | **2.000** | **1.400** | **2.000** | **2.000** |
| XY plane | Measured | 22.898 | 1.974 | 1.964 | 1.479 | 1.902 | 1.473 | 1.910 | 1.482 | 1.912 | 1.477 | 1.908 | 1.484 | 1.958 | 1.975 |
| | **Deviation (Measured Nominal )** | **-0.102** | **-0.026** | **-0.036** | **0.079** | **-0.098** | **0.073** | **-0.090** | **0.082** | **-0.088** | **0.077** | **-0.092** | **0.084** | **-0.042** | **-0.025** |
| XZ plane | Measured | 22.907 | 1.968 | 1.962 | 1.483 | 1.918 | 1.468 | 1.912 | 1.476 | 1.909 | 1.486 | 1.911 | 1.474 | 1.969 | 1.971 |
| | **Deviation (Measured Nominal )** | **-0.093** | **-0.032** | **-0.038** | **0.083** | **-0.082** | **0.068** | **-0.088** | **0.076** | **-0.091** | **0.086** | **-0.089** | **0.074** | **-0.031** | **-0.029** |
| YZ plane | Measured | 22.927 | 1.981 | 1.961 | 1.472 | 1.920 | 1.479 | 1.905 | 1.489 | 1.914 | 1.476 | 1.919 | 1.481 | 1.962 | 1.968 |
| | **Deviation (Measured Nominal )** | **-0.073** | **-0.019** | **-0.039** | **0.072** | **-0.080** | **0.079** | **-0.095** | **0.089** | **-0.086** | **0.076** | **-0.081** | **0.081** | **-0.038** | **-0.032** |

***HS stands for the hole size, WT stands for the wall thickness, SWT stands for the thickness of the wall surrounding the holes**
***On the walls WT1, WT2, WT3, WT4 ,SWT1 and SWT2 “Contouring+Hatching” type of scan is performed**

**Table 6.14: Measured Dimensions of Hole Features on Lattice Structures**

| All dimensions in mm | | | | | | | | Deviation (Measured-Nominal) | | |
|---|---|---|---|---|---|---|---|---|---|---|
| Lattice | Measured Plane | Nominal HS* | Nominal WT* | Scaled** HS | Scaled** WT | Measured HS (Average) | Measured WT***(Average) | HS | WT | Type of Wall Scan |
| 1 | XY | 2 | 0,650 | 2,064 | 0,671 | 1,905± 0.012 | 0,732± 0.009 | 0,095± 0.012 | -0,082± 0.009 | EDGES |
| | XZ | 2 | 0,650 | 2,064 | 0,671 | 1,899± 0.011 | 0,731± 0.012 | 0,101± 0.011 | -0,081± 0.012 | EDGES |
| | YZ | 2 | 0,650 | 2,064 | 0,671 | 1,898± 0.009 | 0,738± 0.011 | 0,102± 0.009 | -0,088± 0.011 | EDGES |
| 2 | XY | 2 | 1,100 | 2,064 | 1,135 | 1,879± 0.013 | 1,215± 0.008 | 0,121± 0.013 | -0,115± 0.008 | Contouring Only |
| | XZ | 2 | 1,100 | 2,064 | 1,135 | 1,877± 0.015 | 1,215± 0.007 | 0,123± 0.015 | -0,115± 0.007 | Contouring Only |
| | YZ | 2 | 1,100 | 2,064 | 1,135 | 1,880± 0.008 | 1,213± 0.009 | 0,120± 0.008 | -0,113± 0.009 | Contouring Only |
| 3 | XY | 2 | 1,400 | 2,064 | 1,445 | 1,908± 0.004 | 1,479± 0.015 | 0,092± 0.004 | -0,079± 0.015 | Contouring + Hatching |
| | XZ | 2 | 1,400 | 2,064 | 1,445 | 1,913± 0.007 | 1,477± 0.007 | 0,087± 0.007 | -0,077± 0.007 | Contouring + Hatching |
| | YZ | 2 | 1,400 | 2,064 | 1,445 | 1,915± 0.009 | 1,479± 0.006 | 0,086± 0.009 | -0,079± 0.006 | Contouring + Hatching |

***HS stands for the hole size, WT stands for the wall thickness**
**** With shrinkage factor 1.032**
***** Average of the WT1, WT2, WT3, WT4 and WT5**

# CHAPTER 7

# CONCLUSIONS AND FUTURE WORK

## 7.1 Conclusions of the Laser Sintered Part Porosity Study (Irregular Porous Structures

In this study, a mathematical model is established which relates the part porosity to the laser sintering machine parameters: the laser power, the laser scan speed and hatching distance. In order to determine the processing window for the parametric experiments, a series of preliminary experiments have been performed by varying the processing parameters. The three processing parameters can be expressed by a single parameter called laser energy density as

$$ED = \frac{P}{HD \cdot LS} \tag{7.1}$$

where $P$ is the laser power, $HD$ is the hatching distance and $LS$ is the laser scan speed. At the high porosity end (where the laser energy density is low), the process limitation was found to be due to the "curling" of the sintered layers, especially at the beginning of the build where the number of layers is small. This phenomenon is frequently observed in SLS, especially at low laser power settings and/or in thin parts.

The process limitation at the low porosity end (where the laser energy density is high) was found to be the "burning" (degradation) of the powder by oversintering, where an excessive amount of smoke was observed during the laser exposure along with discoloration in the part.

The part porosities of the test parts are characterized indirectly, by measuring their apparent densities. As the density of the part increases, the part porosity decreases, thus, the results based on density reflect the relative state of porosity in the produced parts.

From the analysis of the test parts it is seen that the apparent density increases with increasing laser energy density as expected, indicating a reduction in porosity. However, the increase in apparent density slows down, implying an asymptotic limit or, perhaps, a local maximum that is yet to be reached. Further increase in the laser energy density caused degradation of the material, which resulted in decrease in the density.

The mathematical relation, which was developed to predict the apparent density of the laser sintered parts, is determined by fitting the experimental data, which were obtained through $2^3$ factorial experiments, using the least squares method. The resulting equation is presented below

$$\begin{aligned} \rho = {} & 5.347 + 0.144 \cdot LP - 8.522 \cdot 10^{-4} \cdot LS - 12.479 \cdot HD \\ & - 3.012 \cdot 10^{-5} \cdot (LP \cdot LS) + 0.428 \cdot (LP \cdot HD) \\ & + 2.248 \cdot 10^{-4} \cdot (LS \cdot HD) - 8.8591 \cdot 10^{-5} \cdot (LP \cdot LS \cdot HD) \end{aligned} \tag{7.2}$$

where $\rho$ is density in g/cm$^3$, laser power *LP* is in W, the laser scan speed *LS* is in mm/s, and the hatching distance *HD* in mm. For all the parameter configurations, when the measured density of the laser sintered parts are compare with the predicted densities calculated through Equation (7.2), it was seen that there were very little (maximum error around 2.5%) difference between them, which shows that the mathematical model well predicts the apparent mass density.

The approximate porosity in the parts is calculated by using an approximate value for the true density of the polymer powder, PA, 1.15 g/cm$^3$. Similar to the effect on the mass density, for the low laser energy densities the increase in the laser energy density results in steep decrease in the resultant porosity, but for the high laser energy densities the increase in the laser energy density does not cause so much variance in the resulting porosity and porosity reaches an asymptote.

From the analysis, it was also observed that the laser energy density cannot be used as the sole influential factor for porosity of the laser sintered parts; same laser energy density does not always result in the same apparent mass density. The specific values of the parameters that combine to make up the laser energy density are effective. That is for a given laser energy density value, different combinations of parameters that make it up yield different porosities.

## 7.2 Conclusions of Hole Structures Study (Regular Porous Structure)

In this part of the study, hole and lattice structures were built using SLS, to investigate the size/accuracy limitations in building such structures.

With the EOSINT P380 SLS machine and with PA 2200 polyamide powder, it is seen that, very small regular hole sizes could not be produced, (hole size ≤ 1 mm) as the stacked unsintered powder inside of these holes could not be removed without damage to the part. In fact for all the test parts produced, sand-blasting alone was observed to be insufficient in removing the unsintered loose powder inside of the holes. The unsintered powder needed to be poked to loosen and be released from the parts, followed by further sand-blasting.

The holes on all parts were seen to be rounded at the corners, rather than the original model square geometry design. For wall thicknesses and hole dimensions comparable with the effective beam diameter, this is expected since the laser beam path cannot contour sharp corners properly due to its finite width. In addition, thermal relaxation after sintering would allow the corners to curve during solidification. After comparing different sized holes, it is seen that as the hole size increases the amount of curvature on corners decreases.

In the first lattice structure it was seen that, the interior walls were observed to be very brittle and break very easily. As the wall thickness between the holes in the first lattice is 0.66 mm, the exposed areas at the interior intersection sides of the holes are very small, which results in very brittle walls. This brittleness was not observed on other lattices.

The type of the scan exposed on thin wall sections between the holes differs with the value of the wall thickness. The CMM measurements performed on the test parts show that the actual wall thickness values and deviations from design values directly depend on the type of the scan hole features are exposed to. It is also concluded that wall thickness is much more effective than the hole size values on the dimensional accuracy of the resultant hole size, as for the hole features with the same wall thicknesses but different hole sizes, the dimensional deviations from the design values do not differ significantly (Table 6.10).

When the results of the same kind of hole features (same type of scan on the wall sections) of the lattice hole structures and tubular hole structures are compared, it is seen that the deviations do not differ between these structures. Thus it is concluded that the dimensional accuracy of the hole features do not vary with their structure (tubular or lattice).

From all measurements it is seen that, the deviation from the designed values of the walls between the holes are always positive, that is the built wall thickness is always greater than the design thicknesses. Whereas for the hole sizes, the deviation from the design values are always negative. This indicates that the positive deviations in wall thicknesses are compensated through negative deviations in hole sizes.

The amount of deviation in the wall thicknesses is always smaller than the deviation of the hole size ($\Delta HS > \Delta WT$), if the hole features are unscaled (shrinkage factor is 1) or scaled with shrinkage values smaller than 1. Whereas, for the 1.032 shrinkage factor holes, for all structures the deviation in the wall thicknesses is about the same as the hole size (($\Delta HS \cong \Delta WT$). This shows that shrinkage factor is also effective on the dimensional accuracy of the resultant hole size.

The minimum wall thickness that could be produced is around 0.75 mm, during which the EDGES type of scan was applied. Although before the study, the effective beam diameter of the laser beam was predicted as 0.68 mm, as the thickness of the walls scanned with EDGES, is around 0.75 mm, the actual effective beam diameter is thought to be greater than 0.68 mm.

Among all tried wall thickness values, it is seen that the largest positive deviations in wall thicknesses are seen on very thin wall sections. The thinnest wall sections were designed in the first group of hole on Test Part 1, which is 0.2 mm. The nominal hole size of this group was 2 mm. Due to the “EDGES” type of scan, the actual wall thickness between these holes turned out to be 0.750 mm regardless of shrinkage factor and the deviation in the wall thickness, 0.550 mm. Thus the smallest hole sizes were obtained with this group of hole due to the largest deviation in wall thickness.

For the case, 0.68 mm ≤ wall thickness < 1.2 mm, two contouring laser paths scan the wall sections, i.e. “contouring only” type of scan. In this range, it is seen that when the designed wall thickness value gets closer to 0.68 mm, the positive deviation in the wall thickness from design value increases. The reason is that, when the wall thickness gets closer to 0.68 mm, the wall sections are scanned with two overlapping contour exposures. This resulted in double exposure of the wall sections, absorbing more energy per area and resulting in thicker sections with greater deviation. As the designed wall thickness is increased in the range between 0.68 mm and 1.2, it is seen that the positive deviation of wall thickness from design values decreases, due to the decrease in the amount of overlapping of two contouring exposure. For example when the 2.C hole group of Test Part 1 and 1.C hole group of Test Part 2 is compared (both are exposed with “contouring only”, have 1.032 shrinkage factor and have 2 mm nominal hole size), it is seen that the positive deviation in wall thickness of 1.C hole group of Test Part 2 (0.218 mm, Table 6.8) is smaller than it is for 2.C hole group of Test Part 1 (0.422 mm, Table 6.7) as the scaled wall thickness of 1.C hole group of Test Part 2 ( 0.928 mm) is larger than the scaled wall thickness of 2.C hole group of Test Part 1 (0.681 mm). Thus the negative deviation of hole size in 1.C hole group of Test Part 2 (0.228 mm) is also smaller than 2.C hole group of Test Part 1 (0.432 mm).

For the case 1.2 mm ≤ wall thickness, "contouring and hatching" type of scan is performed on the wall sections. Among all tried hole size-wall thickness combinations, it is seen that the most accurate (smallest deviations) resultant hole size and wall thickness could be achieved with the hole features, the walls of which are scanned with "contouring and hatching" type of scan, around 0.095 mm in the hole size and around 0.078 mm in the wall sections. But although the accuracy in the hole size and wall thickness is better, the minimum wall thickness value that could be achieved with this scan is around 1.27 mm, which is quite high when compared with the resulting wall thicknesses for thin sections where EDGES function in system software takes over (i.e. produce wall thickness about 0.75 mm). The increase in the scaled wall thickness value always resulted in better accuracy for other types of scans ("EDGES" and "contouring only"). Whereas with "contouring and hatching" type of scan, the increase in wall thickness does not provide better but almost the same accuracy in "contouring and hatching" type of scan (Table 6.9).

## 7.3 Future Work

In the hole structures study, the process parameters were kept at their standard values of EOSINT P380 laser sintering machine and the resultant geometrical and shape accuracy of the hole features are studied. To further analyze the effect of the process parameters on the final small hole features, a systematic experimental study can be employed similar to that in Chapter 2 and 3) applied in which the process parameters are modified in a controlled manner. With this study, the smallest available hole sizes can perhaps be decreased and the dimensional accuracy of the hole features, further increased.

Considering the final accuracy of the hole features, the rounding of the holes at corners with respect to the process parameters could further be investigated. In this study, the amount of the rounding at corners can be measured with optical photography and the resulting rounding at corners can be related to the process parameters, quantifying deviation from target hole cross section geometry.

Regarding the laser sintered part porosity study; the experimental approach used in the study can be applied for other materials in SLS. If needed, the mathematical model obtained with this study can be further optimized with the statistical methods, such as Taguchi Method.

As part of the future work, the porous structures via SLS (both regular and irregular) can also be characterized for their strength and/or other mechanical properties. Whatever, the application might be, a structural integrity is sought in most cases, even if the part in question may not be a structural component, but a functional one.

## REFERENCES


[1] K.H. Tan, C.K. Chua, K.F. Leong, C.M. Cheah, P. Cheang, M.S. Abu Bakar, S.W. Cha, "Scaffold development using selective laser sintering of polyetheretherketone–hydroxyapatite biocomposite blends" Biomaterials 24 (2003) 3115–3123

[2] D.T. Pham, R.S. Gault: "A Comparison of Rapid Prototyping Technologies", Int. J. Mach. Tools Manuf, Vol 38, pp. 1257-1287, 1998

[3] M Aytaç, "Prototyping of Large Sized Plastic Parts by Using CNC Milling Machines", M. S. Thesis, Middle East Technical University, Ankara, Turkey, 2002

[4] S.H. Choi, S. Samavedam: "Modeling and Optimization of Rapid Prototyping", Comp. in Industry, Vol. 47, pp. 39-53, 2002

[5] R.N. Chuk, V.J. Thomson: "A Comparison of Rapid Prototyping Techniques Used for Wind Tunnel Model Fabrication", Rapid Prototyping Journal, Vol. 4, No 4, pp. 185-196, 1998

[6] "Electro Optic Systems Company", http://www.eos-gmbh.de, 25/04/2005

[7] A. Rosochowski, A. Matuszak: "Rapid Tooling: the State of the Art", Journal of Materials Processing Technology, Vol. 106, pp. 191-198, 2000

[8] N.P. Karapatis, J.-P.S. van Griethuysen, R. Glardon: "Direct Rapid Tooling: a Review of Current Research", Rapid Prototyping Journal, Vol. 4, No 2, pp. 77-89, 1998

[9] E. Radstok: “Rapid Tooling”, Rapid Prototyping Journal, Vol. 5, No 4, pp. 164-168, 1999

[10] R.I. Campbell, M. Martorelli, H.S. Lee: “Surface Roughness for Rapid Prototyping Models”, Computer-Aided Design, 2001

[11] H.C.H. Ho, I. Gibson, W.L. Cheung, “Effects of energy density on morphology and properties of selective laser sintered polycarbonate” Journal of Material Processing Technology 89-90 (1999) 204-210

[12] H. Durr, R. Pilz, N. S. Eleser, “Rapid tooling of EDM electrodes by means of selective laser sintering”, Computers in Industry 39 1999 35–45

[13] P. Dunne, S.P. Soe , G. Byrne , A. Venus , A.R. Wheatley, “Some demands on rapid prototypes used as master patterns in rapid tooling for injection moulding” Journal of Materials Processing Technology (2004)

[14] H. Tan, C.K. Chua, K.F. Leong, C.M. Cheah, P. Cheang, M.S. Abu Bakar, S.W. Cha, “Scaffold development using selective laser sintering of polyetheretherketone–hydroxyapatite biocomposite blends” Biomaterials 24 (2003) 3115–3123

[15] S. Bose, J. Darsel, H.L. Hosick, L. Yang, D.K. Sarkar, A. Bandyopadhyay, “Processing and Characterization of Porous Alumina Sacaffolds”. Journal of Materials Science: Materials in Medicine 13 (2002) 23-28.

[16] Yang S, Loeng KF, Du Z, Chua CK, **“**The development of a tissue engineering scaffold structure library for rapıd prototyping Part II. Rapid

prototyping techniques” Tissue Eng 2002 Feb 8:1-11

[17] C.L. Liew, K.F. Leong, C.K.Chua and Z. Du, “Dual material Rapid Prototyping Techniques for the development of Biomedical Devices”, The International Journal of Advanced manufacturing Technology,2002

[18] J. Jackson, S.Smith, F. Glück, J. Malcolm, S. Chang, “Rapid Prototyping a Trabecular Scaffold”, Group Training Project: Bone Tissue Engineering, School of Mechanical Engineering University of Edinburgh, 2001.

[19] M. Erdal, L. Ertoz, S. Guceri, “Characterization of permeability for solid freeform fabricated porous structures”

[20] S. J. Kalitaa, S. Bose, Howard L. Hosick, A. Bandyopadhyay, “Development of controlled porosity polymer-ceramic composite scaffolds via fused deposition modeling.” Materials Science and Engineering C 23 (2003) 611– 620

[21] G.T.M. Chu, A.G. Brady, W.Miao, J.W. Halloran, S.J. Hollister and D. Brei, “Ceramic SFF by direct and indirect stherelithography”, Proceedings of the MRS Fall Meeting Symposium V: Solid Freefrom and Additive Fabrication, Boston, USA, 542, pp 119-123, 30 Nov-3Dec, 1998

[22] A.N. Chatterjee, Sanjay Kumar, P. Saha, P.K. Mishra, A. Roy Choudhury, “ An experimental design approach to selective laser sintering of low carbon steel” Journal of Materials Processing Technology 136 (2003) 151–157

[23] D. Miller, C. Deckard, J. Williams, “Variable Beam Size SLS workstation and enhanced SLS model” Rapid Prototyping Journal Volume 3, 1997, pp. 4-11.

[24] Y. Song, Experimental study of the basic process mechanism for direct selective laser sintering of low-melting powder, Ann. CIRP 46 (1) (1997) 127–130.

[25] P.J. Hardro, J. Wang, B.E. Stucker, “A design of experiment approach to determine the optimal process parameters for rapid prototyping machines”, Proceedings of the Joint Conference of the Fifth International Conference on Automation Technology and the 1998 International Conference of Production Research.

[26] P.J. Karapatis, Y. Guidoux, P. E. Gygax, R. Glardon, “Thermal Behavıor of DMLS Parts”, Proceedings of the Solid Freeform Fabrication Symposium, Austin, Texas, 1998

[27] S.M. Hur, K.H. Choi, S.H. Lee, P. K. Chang, “Determination of fabricating orientation and packing in SLS process”, Journal of Materails Processing Technology 112 (2001), pp. 236-243

[28] C.W.Ku, I. Gibson, W.L. Cheung, “Selective Laser Sintered Castform™ Polystyrene with Controlled Porosity and its Infiltration Characteristics by Red Wax”, Proceedings of the Solid Freeform Fabrication Symposium, Austin, Texas, 1998

[29] S. Akın, A.R. Kovscek, “Computed Tomography in petroleum engineering research”, Applications of X-ray Computed Tomography in the

Geosciences, Geological Society, London, Special Publications, 215, pp.23-38.

[30] D.C. Montgomery, 2004, The $2^k$ Factorial Design, Design and Analysis of Experiments Fifth Edition*,* pp-218-276

[31] Engineering Materials Handbook, Desk Edition, 1995, ASM International, Materials Park, Ohio, pp 135

## APPENDIX A

## PROPERTIES OF FINE POLYAMIDE PA 2200

***MATERIAL PROPERTIES:***

| | |
|---|---|
| Average particle size | 60 µm |
| Bulk density (ASTM D4164 ) | 0.44 $g/cm^3$ |
| Density of laser sintered part (ASTM D792) | 0.95 $g/cm^3$ |
| Moisture Absorption 23°C (ASTM D570) | 0.41 % |

***MECHANICAL PROPERTIES*:***

| | |
|---|---|
| Tensile Modulus (ASTM D638) | 1700 MPa |
| Tensile strength (ASTM D638) | 45 MPa |
| Elongation at break (ASTM D638) | 15 % |
| Flexural Modulus (ASTM D790) | 1300 MPa |
| Izod . Impact Strength (ASTM 256) | 440 J/m |
| Izod . Notched Impact (ASTM 256) | 220 J/m |

* The mechanical properties were measured with laser sintered parts from recycled powder mixed with 40% of new powder. Parts were built in 0.15mm layer thickness with a laser power of 21 Watt, a hatching distance of 0.30mm and a laser speed of 5000mm/s.

***THERMAL PROPERTIES:***

| | |
|---|---|
| Melting point | 184 °C |

| | |
|---|---|
| DTUL, 0.45 MPa ASTM D648 | 177 °C |
| DTUL, 1.82 MPa ASTM D648 | 86 °C |

***CHEMICAL RESISTANCE:***

| |
|---|
| Alkalines, hydrocarbonates, fuels and solvents |

***ELECTRICAL PROPERTIES:***

| | |
|---|---|
| Volume Resistively<br>22°C, 50%RH, 500V<br>ASTM D257-93 | $3.1*10^{14}$ Ohm*cm |
| Surface Resistively<br>22°C, 50%RH, 500V<br>ASTM D257-93 | $3.1*10^{14}$ Ohm*cm |
| Dielectric Constant<br><br>22°C, 50%RV, 5V 1000Hz<br>D150-95 | 2.9 |
| Dielectric Strength<br>22°C, 50%RV, in air, 5V<br>V/sec<br>D149-95a | $1.6 *10^{4}$ v/mm |

***SURFACE FINISH:***

| | |
|---|---|
| Upper facing (after process) Ra | 8.5 µm |
| Upper facing (after finish) Ra | 0.13 µm |

## APPENDIX B

## EOSINT P380 STANDARD PROCESSING PARAMETERS FOR PA 2200

*SHRINKAGE SCALING*

| Scaling Factors | |
|---|---|
| X, Y Axis | 3.1% |
| Z Axis | 1.3%-1.18% |

| | |
|---|---|
| Layer thickness: | 0.15 mm |

*LASER EXPOSURE PARAMETERS*

| CONTOURING | |
|---|---|
| Laser Power | 9.40 W |
| Laser Scan Speed | 700 mm/s |
| Beam Offset | 0.34 mm |

| HATCHING | |
|---|---|
| Laser Power | 38.2 W |
| Laser Scan Speed | 4500 mm/s |
| Beam Offset | 0.53 mm |
| Hatching Distance | 0.30 mm |

## APPENDIX C

## ESTIMATION OF THE PARAMETERS IN LINEAR REGRESSION MODELS

The method of least squares is typically used to estimate the regression coefficients in a multiple linear regression model. Suppose that $n > k$ observations on the response variable are available, say $y_1, y_2, \ldots, y_n$. Along with each observed response $y_i$, we will have an observation on each regressor variable and let $x_{ij}$ denote the $i$th observation on variable $x_j$. The data will appear as in Table A.1.

We may write the model equation (Equation 5.16) in terms of the observations in Table 5 as

$$\begin{aligned} y_i &= \beta_0 + \beta_1 x_{i1} + \beta_2 x_{i2} + \ldots\ldots\ldots + \beta_k x_{ik} + \varepsilon_i \\ &= \beta_0 + \sum_{j=1}^{k} \beta_j x_{ij} + \varepsilon_i \end{aligned} \tag{A.1}$$

The method of least squares chooses the $\beta$'s in Equation A.1 so that the sum of the squares of errors, $\varepsilon_i$, is minimized. The least squares function is

**Table A.1: Data for Multiple Linear Regression**

| y | $x_1$ | $x_2$ | ..... | $x_k$ |
|---|---|---|---|---|
| $y_1$ | $x_{11}$ | $x_{12}$ | .... | $x_{1k}$ |
| $y_2$ | $x_{21}$ | $x_{22}$ | .... | $x_{2k}$ |
| . | . | . | | . |
| . | . | . | | . |
| $y_n$ | $x_{n1}$ | $x_{n2}$ | .... | $x_{nk}$ |

$$\begin{aligned} L &= \sum_{i=1}^{n} \varepsilon_i^{\,2} \\ L &= \sum_{j=1}^{n} (y_i - \beta_0 - \sum_{j=1}^{k} \beta_j x_{ij})^2 \end{aligned} \tag{A.2}$$

The function $L$ *is to be minimized with respect to* $\beta_0$, $\beta_1$..., $\beta_k$. The least squares estimators, say $\hat{\beta}_0, \hat{\beta}_1, ........ \hat{\beta}_k$, must satisfy

$$\left.\frac{\partial L}{\partial \beta_0}\right|_{\hat{\beta}_0, \hat{\beta}_1 ...., \hat{\beta}_k} = -2\sum_{j=1}^{n}(y_i - \hat{\beta}_0 - \sum_{j=1}^{k}\hat{\beta}_j x_{ij}) = 0 \qquad \text{(A.3.a)}$$

and

$$\left.\frac{\partial L}{\partial \beta_j}\right|_{\hat{\beta}_0, \hat{\beta}_1 ...., \hat{\beta}_k} = -2\sum_{j=1}^{n}(y_i - \hat{\beta}_0 - \sum_{j=1}^{k}\hat{\beta}_j x_{ij})x_{ij} = 0 \quad j=1,2,...., k \quad \text{(A.3.b)}$$

Simplifying Equation A.3,

$$\begin{array}{l}
n\hat{\beta}_0 + \hat{\beta}_1 \sum_{i=1}^{n} x_{i1} + \hat{\beta}_2 \sum_{i=1}^{n} x_{i2} + ........ + \hat{\beta}_k \sum_{i=1}^{n} x_{ik} = \sum_{i=1}^{n} y_i \\
\hat{\beta}_0 \sum_{i=1}^{n} x_{i1} + \hat{\beta}_1 \sum_{i=1}^{n} x_{i1}{}^2 + \hat{\beta}_2 \sum_{i=1}^{n} x_{i1}x_{i2} + ........ + \hat{\beta}_k \sum_{i=1}^{n} x_{i1}x_{ik} = \sum_{i=1}^{n} x_{i1} y_i \\
\quad . \qquad\qquad . \qquad\qquad . \qquad\qquad . \\
\quad . \qquad\qquad . \qquad\qquad . \qquad\qquad . \\
\quad . \qquad\qquad . \qquad\qquad . \qquad\qquad . \\
\hat{\beta}_0 \sum_{i=1}^{n} x_{ik} + \hat{\beta}_1 \sum_{i=1}^{n} x_{ik}x_{i1} + \hat{\beta}_2 \sum_{i=1}^{n} x_{ik}x_{i2} + ........ + \hat{\beta}_k \sum_{i=1}^{n} x_{ik}{}^2 = \sum_{i=1}^{n} x_{ik} y_i
\end{array} \qquad \text{(A.4)}$$

These equations are called the **least squares normal equations. T**here are $p$=k+1 normal equations, one for each of the unknown regression coefficients. The solutions to the normal equations will be the least square estimators of the regression coefficients $\hat{\beta}_0, \hat{\beta}_1, ........ \hat{\beta}_k$ .

It is simpler to solve the normal equations if they are expressed in matrix notation. Equation A.1 may be written in matrix notation as

$$y = X\beta + \varepsilon \qquad \text{(A.5)}$$

where

$$y = \begin{bmatrix} y_1 \\ y_2 \\ . \\ . \\ y_n \end{bmatrix} \quad , \qquad X = \begin{bmatrix} 1 & x_{11} & x_{12} & \dots & x_{1k} \\ 1 & x_{21} & x_{22} & \dots & x_{2k} \\ . & . & . & \dots & . \\ . & . & . & \dots & . \\ . & . & . & \dots & . \\ 1 & x_{n1} & x_{n2} & \dots & x_{nk} \end{bmatrix}$$

$$\beta = \begin{bmatrix} \beta_0 \\ \beta_1 \\ . \\ . \\ \beta_k \end{bmatrix} \quad \text{and} \qquad \varepsilon = \begin{bmatrix} \varepsilon_1 \\ \varepsilon_2 \\ \varepsilon_3 \\ \varepsilon_4 \\ \varepsilon_5 \end{bmatrix}$$

In general, **y** is an ($n$ x 1) vector of the observations, **X** is an ($n$ x p) matrix of the levels of the independent variables, ***β*** is ($p$ x 1) vector of the regression coefficients, and ***ε*** is an (n x1) vector of the random errors.

It is intended to find the vector of least squares estimators, $\hat{\beta}$ , that minimizes

$$L = \sum_{j=1}^{n} \varepsilon_1{}^2 = \varepsilon'\varepsilon = (y - X\beta)'(y - X\beta) \tag{A.6}$$

$L$ may be expressed as

$$\begin{aligned} L &= y'y - \beta'X'y - y'X\beta + \beta'X'X\beta \\ &= y'y - 2\beta'X'y + \beta'X'X\beta \end{aligned} \tag{A.7}$$

because $\beta'X'y$ is a (1 x 1) matrix, or a scalar, and its transpose $(\beta'X'y)' = y'X\beta$ is the same scalar. The least squares estimators must satisfy

$$\left.\frac{\partial L}{\partial \beta}\right|_{\beta} = -2X'y + 2X'X\hat{\beta} = 0 \tag{A.8}$$

which simplifies to

$$X'X\hat{\beta} = X'y \tag{A.9}$$

Equation (A.9) is the matrix form of the least squares normal equations. It is identical to Equation (A.4). To solve the normal equations, the both sides of the Equation (A.9) is multiplied by the inverse of the $X'X$. Thus, the least squares estimator of $\beta$ is

$$\hat{\beta} = (X'X)^{-1} X'y \qquad \text{(A.10)}$$

The fitted regression model is

$$\hat{y} = X\hat{\beta} \qquad \text{(A.11)}$$

In scalar notation, the fitted model is

$$\hat{y}_i = \hat{\beta}_0 + \sum_{i=1}^{k} \hat{\beta}_j x_{ij} \qquad i = 1,2,\text{..........},\text{n} \qquad \text{(A.12)}$$

The difference between the actual observation $y_i$ and the corresponding fitted value $\hat{y}_i$ is the **error**, say $e_i = y_i - \hat{y}_i$. The (n x 1) vector of error is denoted by

$$e = y - \hat{y} \qquad \text{(A.13)}$$

## THE STEPS OF THE LEAST SQUARE METHOD IN THE DENSITY EXPERIMENT

The experimental data on the density study, is shown in Table A.2 below, with the exact values of each parameter.

During establishing the $\delta$ (response) matrix, for each run the mean of the responses observed in the two replicates are taken. The $X$ matrix and $\delta$ vector are

**Table A.2: The Results of $2^3$ Factorial Design Density Variation Experiment**

| | | Parameter* Levels | | | Measured Apparent Mass Density ($g/cm^3$) | | | |
|---|---|---|---|---|---|---|---|---|
| Process Config. | Test Run | Laser Power (A, W) | Laser Scan Speed (B, mm/s) | Hatching Distance (C, mm) | Replicate 1 | Replicate 2 | Density Sum ($g/cm^3$) | Density Avg. ($g/cm^3$) |
| -1 | 1 | 28.15 | 4000 | 0.3 | 0.955 | 0.950 | 1.905 | 0.953 |
| a | 2 | 38.22 | 4000 | 0.3 | 0.965 | 0.971 | 1.936 | 0.968 |
| b | 3 | 28.15 | 5000 | 0.3 | 0.875 | 0.883 | 1.758 | 0.879 |
| ab | 4 | 38.22 | 5000 | 0.3 | 0.951 | 0.957 | 1.908 | 0.954 |
| c | 5 | 28.15 | 4000 | 0.45 | 0.764 | 0.773 | 1.537 | 0.769 |
| ac | 6 | 38.22 | 4000 | 0.45 | 0.933 | 0.934 | 1.867 | 0.934 |
| bc | 7 | 28.15 | 5000 | 0.45 | 0.696 | 0.704 | 1.400 | 0.700 |
| abc | 8 | 38.22 | 5000 | 0.45 | 0.771 | 0.775 | 1.546 | 0.773 |

$$X := \begin{array}{c} \begin{array}{cccccccc} & x_1 & x_2 & x_3 & x_4 & x_5 & x_6 & x_7 \end{array} \\ \begin{pmatrix} 1 & 28.15 & 4000 & 0.3 & 112600 & 8.445 & 1200 & 33780 \\ 1 & 38.22 & 4000 & 0.3 & 152880 & 11.466 & 1200 & 45864 \\ 1 & 28.15 & 5000 & 0.3 & 140750 & 8.445 & 1500 & 42225 \\ 1 & 38.22 & 5000 & 0.3 & 191100 & 11.466 & 1500 & 57330 \\ 1 & 28.15 & 4000 & 0.45 & 112600 & 12.66 & 1800 & 50670 \\ 1 & 38.22 & 4000 & 0.45 & 152880 & 17.199 & 1800 & 68796 \\ 1 & 28.15 & 5000 & 0.45 & 140750 & 12.66 & 2250 & 63337 \\ 1 & 38.22 & 5000 & 0.45 & 191100 & 17.199 & 2250 & 85995 \end{pmatrix} \end{array} \qquad \delta := \begin{pmatrix} 0.953 \\ 0.968 \\ 0.879 \\ 0.954 \\ 0.769 \\ 0.934 \\ 0.704 \\ 0.773 \end{pmatrix}$$

The $X^T X$ matrix is

$$X^T \cdot X = \begin{pmatrix} 8 & 265.48 & 3.6\times 10^4 & 3 & 1.195\times 10^6 & 99.54 & 1.35\times 10^4 & 4.48\times 10^5 \\ 265.48 & 9.013\times 10^3 & 1.195\times 10^6 & 99.555 & 4.056\times 10^7 & 3.379\times 10^3 & 4.48\times 10^5 & 1.521\times 10^7 \\ 3.6\times 10^4 & 1.195\times 10^6 & 1.64\times 10^8 & 1.35\times 10^4 & 5.442\times 10^9 & 4.479\times 10^5 & 6.15\times 10^7 & 2.041\times 10^9 \\ 3 & 99.555 & 1.35\times 10^4 & 1.17 & 4.48\times 10^5 & 38.82 & 5.265\times 10^3 & 1.747\times 10^5 \\ 1.195\times 10^6 & 4.056\times 10^7 & 5.442\times 10^9 & 4.48\times 10^5 & 1.848\times 10^{11} & 1.521\times 10^7 & 2.041\times 10^9 & 6.929\times 10^{10} \\ 99.54 & 3.379\times 10^3 & 4.479\times 10^5 & 38.82 & 1.521\times 10^7 & 1.318\times 10^3 & 1.747\times 10^5 & 5.931\times 10^6 \\ 1.35\times 10^4 & 4.48\times 10^5 & 6.15\times 10^7 & 5.265\times 10^3 & 2.041\times 10^9 & 1.747\times 10^5 & 2.398\times 10^7 & 7.959\times 10^8 \\ 4.48\times 10^5 & 1.521\times 10^7 & 2.041\times 10^9 & 1.747\times 10^5 & 6.929\times 10^{10} & 5.931\times 10^6 & 7.959\times 10^8 & 2.702\times 10^{10} \end{pmatrix}.$$

The $(X^T X)^{-1}$ is calculated as

$$
\left(X^T \cdot X\right)^{-1} = \begin{pmatrix}
1.174\times 10^{4} & -345.838 & -2.587 & -3.005\times 10^{4} & 0.076 & 885.524 & 6.632 & -0.195 \\
-345.838 & 10.428 & 0.076 & 885.382 & -2.298\times 10^{-3} & -26.701 & -0.195 & 5.89\times 10^{-3} \\
-2.587 & 0.076 & 5.774\times 10^{-4} & 6.625 & -1.701\times 10^{-5} & -0.195 & -1.48\times 10^{-3} & 4.361\times 10^{-5} \\
-3.005\times 10^{4} & 885.382 & 6.625 & 8.003\times 10^{4} & -0.195 & -2.359\times 10^{3} & -17.664 & 0.52 \\
0.076 & -2.298\times 10^{-3} & -1.701\times 10^{-5} & -0.195 & 5.125\times 10^{-7} & 5.884\times 10^{-3} & 4.361\times 10^{-5} & -1.314\times 10^{-6} \\
885.524 & -26.701 & -0.195 & -2.359\times 10^{3} & 5.884\times 10^{-3} & 71.129 & 0.521 & -0.016 \\
6.632 & -0.195 & -1.48\times 10^{-3} & -17.664 & 4.361\times 10^{-5} & 0.521 & 3.947\times 10^{-3} & -1.163\times 10^{-4} \\
-0.195 & 5.89\times 10^{-3} & 4.361\times 10^{-5} & 0.52 & -1.314\times 10^{-6} & -0.016 & -1.163\times 10^{-4} & 3.504\times 10^{-6}
\end{pmatrix}
$$

and the $X^T\delta$ vector is

$$
X^T \cdot \delta = \begin{pmatrix} 7.034 \\ 234.831 \\ 3.15\times 10^{4} \\ 2.593 \\ 1.051\times 10^{6} \\ 86.624 \\ 1.16\times 10^{4} \\ 3.876\times 10^{5} \end{pmatrix}
$$

The least square estimate of $\beta$ is calculated from equation A.10 as:

$$
\beta = (X^T X)^{-1} X^T \delta
$$

$$
\beta = \begin{pmatrix} 5.377 \\ -0.144 \\ -8.522\times 10^{-4} \\ -12.479 \\ 3.012\times 10^{-5} \\ 0.428 \\ 2.248\times 10^{-3} \\ -8.591\times 10^{-5} \end{pmatrix}
$$

so the least squares fit is:

$$
\begin{aligned}
\delta = 5.377 - 0.144x_1 - 8.522\times10^{-4}x_3 - 12.479x_3 + \\
3.012\times10^{-5}x_4 + 0.428x_5 + 2.248\times10^{-3}x_6 - 8.591\times10^{-5}x_7
\end{aligned}
\tag{A.14}
$$

Substituting the $x_4 = x_1 x_2$, $x_5 = x_1 x_3$, $x_6 = x_2 x_3$ and $x_7 = x_1 x_2 x_3$ into Equation 5.33, the exact least square fit is found as:

$$\begin{aligned} \delta = 5.377 - 0.144x_1 - 8.522\times10^{-4} x_3 - 12.479x_3 + 3.012\times10^{-5} x_1 x_2 \\ + 0.428x_1 x_3 + 2.248\times10^{-3} x_2 x_3 - 8.591\times10^{-5} x_1 x_2 x_3 \end{aligned} \tag{A.15}$$

where $x_1$ stands for the laser power, $x_2$ for the laser scan speed, $x_3$ for the hatching distance.